Deciphering the regulatory transcriptional landscape underlying right ventricular remodeling

Inaugural Dissertation

Submitted to the

Faculty of Medicine (FB-11)

In partial fulfillment of the requirements for the degree of

Doctor of Human Biology (Dr. biol. hom.)

of the Justus Liebig University Giessen

by

Fatemeh Khassafi

From Kashan, Iran

Giessen, 2024

MAX PLANCK INSTITUTE
FOR HEART AND LUNG RESEARCH

UKGM
UNIVERSITÄTSKLINIKUM
GIESSEN UND MARBURG

Deciphering the regulatory transcriptional landscape underlying right ventricular remodeling

Inaugural Dissertation

Submitted to the

Faculty of Medicine (FB-11)

In partial fulfillment of the requirements for the degree of

Doctor of Human Biology (Dr. biol. hom.)
of the Justus Liebig University Giessen

by

Fatemeh Khassafi

From Kashan, Iran

Giessen, 2024

From the Max-Planck-Institute for Heart and Lung Research
and the Faculty for Internal Medicine of the Justus Liebig University Giessen

Aus dem Fachbereich Medizin
der Justus-Liebig-Universität Gießen

Center for Infection and Genomics of the Lung (CIGL)

Lung Vascular Epigenetics

Gutachterin: Prof. Dr. Pullamsetti, Soni Savai

Gutachter: Prof. Dr. Samakovlis, Christos

Tag der Disputation: 21.08.2024

Dedicated to

The women of my country and around the world,
who have been denied education due to oppression.

Table of Contents

LIST OF TABLES

LIST OF FIGURES

Figure 27: Summary of common dysregulated genes and associated pathways.

Figure 28: Selected differentially regulated genes associated with ECM in human RV and MCT-rat RV samples

Figure 29: Western blot validations of 4 ECM proteins in MCT-RV

LIST OF ABBREVIATION

PH	Pulmonary hypertension
PAH	Pulmonary arterial hypertension
CTEPH	Chronic thromboembolic pulmonary hypertension
iPAH	Idiopathic pulmonary arterial hypertension
PVR	Pulmonary vascular resistance
mPAP	Mean pulmonary arterial pressure
RHC	Right heart catheterization
PVD	Pulmonary vascular disease
RV	Right ventricle
LV	Left ventricle
RVH	Right ventricle hypertrophy
RVF	Right ventricle failure
EF	Ejection fraction
SV	Stroke volume
CO	Cardiac output
RVEF	Right ventricle ejection fraction
RVEDP	Right ventricle end diastolic pressure
RVSP	Right ventricle systolic pressure
MCT	Monocrotaline
PAB	Pulmonary arterial banding
SuHx	Sugen-hypoxia
Ees	End-systolic elastance
Ea	Effective arterial elastance
RV-PA	Right ventricular–pulmonary artery
ECM	Extracellular matrix
ER-(α/β)	Estrogen receptors (alpha/beta)
BNP	Brain natriuretic peptide
DEG	Differentially expressed gene
FAO	Fatty acid oxidation

1. INTRODUCTION

1.1 Pulmonary Hypertension

Pulmonary hypertension (PH) represents a complex spectrum of cardiovascular disorders characterized by an elevated mean pulmonary artery pressure (mPAP) of more than 20 mmHg[1]. However, to better cover all forms of PH in the definition, it is essential to include a pulmonary artery wedge pressure (PAWP) of 15 mmHg or lower, and a pulmonary vascular resistance (PVR) of 3 Wood units (WU) or more[2]. Pulmonary hypertension is gaining increased recognition followed by growing diagnosis, as it is estimated to affect >1% of the general population in recent years, and subsequent poor survival and quality of life, when accounting for all forms of PH[3]. The gold-standard diagnosis of PH is through right heart catheterization (RHC). However, the diagnosis of PH goes beyond right heart catheterization or echocardiography, and requires a comprehensive investigation of the etiology and an understanding of the underlying pathophysiology[4].

The classic classification of PH distinguishes between postcapillary PH, which is related to increased pulmonary venous pressure in left-sided heart disease (LHD), and precapillary PH, which results from pulmonary vascular remodeling and obstruction. Remodeling results in thickening of the intima and/or medial layers of the muscular vessels, leading to distal muscularization of the precapillary arterioles and increased PVR. On the other hand, PH is categorized into five main groups, each reflecting different etiologies and requiring different therapies. It is noteworthy that even mild forms of PH are associated with an increased risk of mortality regardless of the etiology. The global burden is pronounced, particularly in low- and middle-income countries, where comorbidities such as congenital heart disease, rheumatic heart disease, cardiomyopathies, chronic lung disease, endemic infections and other conditions contribute significantly. Limited access to diagnostic and therapeutic interventions in low- and middle-income countries exacerbates the challenge, and underestimation of the global burden of disease makes effective advocacy for screening, diagnosis and management difficult, particularly in vulnerable populations[1].

1.2 Pulmonary Hypertension classification

In the World Health Organization's 2008 Dana Point clinical classification, PH is divided into five different categories based on common etiologies and similar histopathological conditions.

However, the original classification was changed to Group 1 in particular after the 5th World Symposium in 2013 and the current classification[5] are shortly explained below:

Group 1 encompasses Pulmonary Arterial Hypertension (PAH), the most extensively studied form of PH, with diverse origins such as idiopathic, familial (often due to BMPR2 gene mutations), anorexigen-induced PH, and others. PAH is clinically characterized by a mPAP ≥ 25 mmHg, often companied by left (and right) ventricular end-diastolic pressure (LVEDP) ≤ 15 mmHg, and pulmonary vascular resistance (PVR) > 3, while molecularly identified by vasculopathy affecting distal pulmonary arteries, vascular proliferation, fibrosis, medial hypertrophy, and enhanced vasoconstriction. Group 2 PH is Pulmonary Venous Hypertension (PVH) due to left heart disease, resulting from elevated left atrial pressure due to left heart abnormalities. This group is relatively less studied, while it is known as the most common form of PH. Group 3, associated with lung disease/hypoxemia, is prevalent in conditions like chronic obstructive pulmonary disease (COPD) and interstitial lung disease (ILD). Group 4 is Chronic Thromboembolic Pulmonary Hypertension (CTEPH), stemming from chronic pulmonary thromboembolic events, while Group 5 comprises PH with unclear multifactorial mechanisms, including diverse causes like sarcoid lung disease, glycogen storage disease, and thyroid disorders. Despite their similarities, each form of PH has been defined by their distinct hemodynamics and pathophysiological features, summarized in Table 1[1,2].

CLASSIFICATION	WHO GROUP	POSSIBLE ETIOLOGIES
PAH (vascular remodeling of pulmonary arteries)	1	Idiopathic, heritable, drug and toxin-associated, connective tissue disease, HIV infection, congenital heart disease, schistosomiasis, portal hypertension
PH associated with left-sided heart disease	2	Left ventricular systolic/diastolic dysfunction, valvular heart disease, congenital/acquired inflow/outflow tract obstruction, cardiomyopathy
PH associated with lung disease	3	Chronic obstructive pulmonary disease, Interstitial lung disease, chronic exposure to high altitude, hypoventilation syndromes, pulmonary diseases with restrictive and obstructive pattern
PH associated with pulmonary artery obstructions	4	CTEPH, large or proximal vessel disorders, reduced compliance and luminal narrowing
PH with unclear and/or multifactorial mechanisms	5	Hematological disorders including sickle cell disease, systemic disorders including sarcoidosis, metabolic disorders, fibrosing mediastinitis, renal failure on dialysis

Table 1; Classification of PH into five groups. The main clinical differences and the different etiologies underlying each form of PH have been outlined. *The table has been adopted from Mocumbi et al, Nature Reviews Disease Primers, 2024*[1].

1.3 Pulmonary Arterial Hypertension (PAH)

PAH, formerly known as primary PH, is the subject of the most comprehensive studies of all types of PH. This is mainly due to the high mortality rate, which averages around 15% with conventional therapy. In addition, PAH is associated with various etiologies, which leads to increased mechanistic complexity and requires extensive investigations[4].

PAH is subsequently classified into five subgroups, reflecting its complex and varied nature, based on etiology and pathophysiology. Idiopathic (iPAH) and heritable PAH, denoted as Groups 1.1 and 1.2, are characterized by unknown cause or genetic mutations such as in BMPR2 gene (the most common) and other related genes[6,7]. Group 1.3 addresses drug- and toxin-induced PAH, underscoring the role of substances like fenfluramine and amphetamines as potential triggers[8,9]. Groups 1.4.1 to 1.4.6 encompass PAH associated with various medical conditions such as connective tissue diseases, HIV infection, Porto-pulmonary hypertension (POPH), congenital heart diseases, schistosomiasis, and chronic hemolytic anemia, emphasizing the disease's prevalence and unique characteristics in each context[10–15]. Lastly, Group 1 focuses on pulmonary veno-occlusive disease and pulmonary capillary hemangiomatosis, highlighting their distinct yet related pathological features to iPAH[16]. This sub-classification emphasizes the need for precise diagnosis and understanding of the underlying causes to effectively manage and treat PAH.

While all subcategories of PAH are clinically characterized by mPAP of >20 mmHg, with a normal pulmonary artery wedge pressure (PAWP) of <15 mmHg, measured by right-heart catheterization, PAH is also characterized by the specific (‘precapillary’) pulmonary arterial remodeling[17], as the extensive remodeling happen in precapillary pulmonary arteries, is the main cause of the elevated pulmonary pressure. Here, we present a comprehensive summary of cellular and molecular hallmarks of PAH, highlighting both the driving factors and the primary effects of the disease.

1.3.1 Survival and current therapeutic approaches in PAH

Despite the significant advances in understanding the pathophysiology of PAH in recent years, the mortality rates among these patients are still notably high, depending on diverse clinical backgrounds and etiologies. According to the latest data from the REVEAL (Registry to Evaluate Early and Long-term PAH Disease Management) registry[18], the average survival rates for PAH patients are reported to be 85-91% at 1 year, 68-75% at 3

years, and approximately 57-65% at 5 years. For iPAH patients, the median survival of 2.8 years has been reported underlining the disease's critical prognosis condition. PAH survival is profoundly affected by factors such as the early diagnosis, accuracy of prognosis, efficient management, and the appropriate selection of therapeutic interventions, which also play a critical role in enhancing the patients' quality of life. Several studies show that the disease occurs predominantly in women and have emphasized the association between the disease and age, connective tissue disease, congenital heart disease and other factors, while showing better survival rates, focusing on these important mortality risk factors such as gender[19–21]. The significance of the right ventricular (RV) response to pressure load in PAH is increasingly acknowledged as a vital determinant of survival. Consequently, there is a growing interest on strategies aiming to preserve myocardial function, emphasizing their profound influence on both survival rates and quality of life in PAH patients[22].

PAH is treated with drugs that mainly target vasodilation via different signaling pathways such as prostacyclin, nitric oxide and endothelin[2]. In addition, conventional treatment follows a multi-parameter risk assessment, guiding the choice between dual or triple combination therapies, and adjustment based on treatment response[23]. Nonetheless, managing PAH in older patients, who more frequently have multiple comorbidity conditions, present a unique challenge, as they show a varied response to PAH medications[24]. Given the complex and evolving nature of PAH in older individuals, there is an urgent need for more targeted research to guide therapeutic strategies effectively.

Furthermore, the multi-factorial condition of PAH, significantly impacts the quality of life across all ages. The gap between symptom onset and treatment initiation, is often substantial, and complicates timely detection of the disease. Such delays in diagnosis and therefore, leaving the condition untreated, profoundly impairs the quality of life, and restricts physical activities, while significantly increases the risk of premature death, reflecting the critical need for timely diagnosis and personalized treatment to mitigate the life-limiting effects of PAH[25,26].

The RV plays a crucial role in determining the quality of life of PAH patients, as it mainly carries the increased pulmonary pressure. Its ability to adapt and maintain its function has a direct impact on cardiac output and thus on the patient's ability to perform daily activities. Deterioration of RV function therefore leads to symptoms such as fatigue and dyspnea, which significantly affect quality of life, and maintaining RV function is crucial to mitigate the impact of PAH on patients' well-being[27].

1.4 Driving factors of PAH

PAH as a severe vasculopathy is characterized by vascular stiffening and especially by vasoconstriction, which initially leads to reduced pulmonary circulation and secondarily to RV hypertrophy and failure[1]. At the genetic level, mutations in multiple PAH-related genes, predominantly BMPR2, result in increased vasoconstriction, cell proliferation, inflammation, and reduced apoptosis, influencing both disease's progression and severity. While these mutations are highly prevalent in the familial form of PAH, there is also a significant accumulation of mutations in iPAH, with some emerging since childhood. The risk of developing PAH among BMPR2 mutation carriers necessitates annual screening and genetic counseling not only for early detection, but also targeted therapies[28].

At epigenetic level, PAH is influenced by DNA methylation, microRNAs expression, and histone deacetylation, affecting related gene expression without altering the DNA sequence[29,30]. These mechanisms collectively contribute to disease progression by regulating pathways related to hypoxia, vasoconstriction, inflammation, and excessive cell proliferation in various cell types, which altogether driving PAH. Therefore, understanding the complex interplay of genetic and epigenetic factors is crucial for developing precise diagnostics and effective treatments for PAH.

1.5 Hallmarks of PAH

As mentioned above, PAH is a complex disease marked by excessive vasoconstriction and abnormal vascular remodeling, affecting all layers of pulmonary vessels and leading to a severe reduction in vascular cross-sectional area, which results in elevated pulmonary pressure, increased right ventricular afterload, and decreased large pulmonary artery compliance; putting strain on the right ventricle. The cellular and structural changes of the vessels, characterized by endothelial injury, cell proliferation, and enhanced extracellular matrix deposition, suggest a transition of cells to a proliferative and apoptosis-resistant state. Vascular remodeling on the other hand, is linked to chronic inflammation and the involvement of various progenitor cell types, which either contribute to or potentially counteract the proliferative changes[22].

The pathological processes in PAH can be categorized into several hallmarks (Figure 1). Firstly, there's an imbalance in vasoactive mediators, with a decrease in vasodilatory mediators like prostaglandin I_2 and nitric oxide, and an increase in vasoconstrictors like thromboxane and endothelin-1[31,32]. Secondly, vascular cell proliferation and remodeling are driven by certain vasoconstrictors like endothelin, as well as growth factors, and

activated intracellular signaling cascades that promote not only cellular proliferation, but migration, and resistance to apoptosis[33,34]. Amongst these driving growth factors and signaling pathways, VEGFs, TGF-β, Notch and PPAR-γ signaling roles and effect on the smooth muscle cells, and a lesser extent, endothelial cells and fibroblasts proliferation are have been studied more extensively over the last decade[22]. The deregulated growth of endothelial cells and disordered angiogenesis possibly affecting endothelial repair, along with the role of endothelial progenitor cells emerges as a third hallmark of PAH, and a potential focus for therapeutic interventions[35]. Inflammation, is another key hallmark and triggers of PAH, characterized by the presence of various immune cells in the lung vasculature and contributes to the development of pulmonary plexiform lesions[36,37]. Additionally, the disease is marked by a shift in cellular metabolism towards glycolysis, similar to cancer cells, which is believed to impact the resistance to apoptosis and maintain vascular remodeling[38]. Moreover, thrombosis is another commonly observed phenotype, particularly in iPAH patients, which further complicates the disease by enhancing the hypercoagulable state[39]. Altogether, these phenomena contribute to the vascular remodeling known as the primary hallmark of PAH.

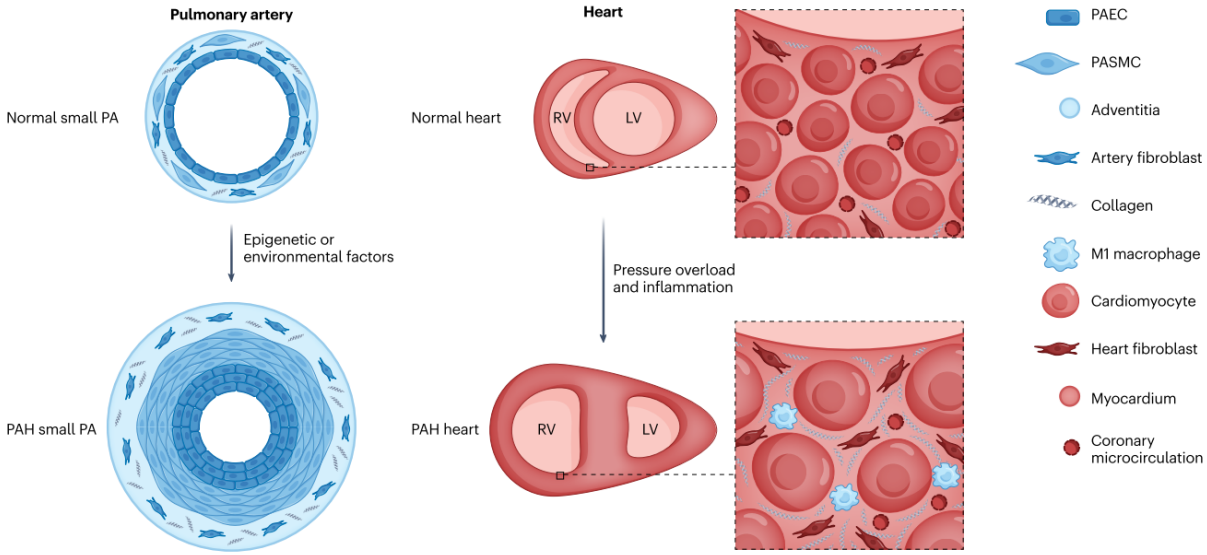

Figure 1: Pathologic phenotype of PAH in lung vasculature and in heart. PAH progression involves various cell types in lung and heart (right ventricle) tissue, each contributing to one or more hallmark features of PAH. Left part displays vascular remodeling in pulmonary arteries and the right panel shows the hypertrophy and remodeling of the right ventricle associated with PAH. Various molecular alterations underlie the phenotype shift in the respective cell types. *This figure has been adopted from Mocumbi et al, Pulmonary hypertension, Nature Reviews disease primers, 2023*[1].

Secondary hallmark of PAH is the right ventricular hypertrophy (RVH). Hypertrophy arises in the RV due to increased resistance in the pulmonary circulation, leading to muscle mass accumulation and wall thickening as an initial compensatory response to increase

RV afterload, in PAH. However, sustained resistance eventually results in RV dysfunction, dilatation, and RV failure (RVF). In addition, the increased pressure in the RV increases RV wall tension and oxygen demand, which impedes myocardial perfusion and triggers right ventricular ischaemia. This mechanical stress activates various cellular signaling pathways as well as a metabolic shift towards increased glucose uptake and glycolysis, which collectively contribute to RVH and RVF. Understanding the complex processes of RVH and subsequent failure, is crucial for the development of targeted therapies and management strategies for PAH[40–42].

1.6 Right ventricle

As illustrated in Figure 1, RV experiences a progressive remodeling in PAH, a process that despite being subsequent to the primary cause, it remains as critical as pulmonary vascular remodeling, because it is the main contributor to the high morbidity and mortality in PAH patients. However, our understanding of RV remodeling and RV dysfunction is very limited, although one of the central goals of PAH treatment is to reverse RV remodeling and maintain its normal function in order to improve survival and quality of life[43]. Besides, the unique anatomy and biology of the RV, distinct from the left ventricle (LV), linked to pulmonary circulation, necessitates a deeper understanding, which is further crucial for development of innovative therapeutic strategies. Here we first introduce the basic concepts such as co-development of RV and pulmonary circulation, anatomical differences between RV and LV, RV function in physiological and pathophysiological of PAH context.

1.6.1 Development of RV and pulmonary circulation

During fetal development, the right ventricle is the dominant chamber, handling about 60% of the cardiac output. In contrasts, at birth, the RV's dominance is reduced as the pulmonary resistance decreases and the LV undergoes hypertrophy to take on the systemic circulation's demands. Over time, the RV adapts to lower resistance and pressures compared to the LV, marking a distinct developmental trajectory from the fetal period to adulthood[44].

In adult pulmonary circulation, the pulmonary artery divides into smaller vessels, conducting blood flow through a low-pressure system critical for gas exchange, while avoiding pulmonary edema due to the highly permeable alveolar membranes. Unlike the systemic circulation, pulmonary arterioles exhibit incomplete smooth muscle layers, especially those < 70 microns

diameter, indicating a unique regulatory mechanism, including oxygen sensing and the influence of vasoactive substances[44]. To investigate the right ventricle function in normal and pathologic conditions of pulmonary circulation, several concepts, like pulmonary input impedance, are commonly used to describe the resistance to flow in the pulmonary circulation and the resulting "afterload" on the RV[45]. The right ventricle encounters the "afterload" mainly determined by PVR, which RV must overcome to pump blood through the pulmonary circuit. PVR, calculated as the average pressure difference between the main pulmonary artery and the left atrium, divided by the mean cardiac output, is a critical determinant of the RV's workload in total, and small changes in vessel resistance having a significant impact. The balance of vessel resistance, blood flow regulation, and RV afterload highlights the complexities of pulmonary circulation and the critical role of the RV in sustaining this balance in pulmonary circulation[44].

1.6.2 Right ventricle anatomy differs from left ventricle

The RV is significantly thinner than the LV, comprises about one-sixth of the heart's total mass with a wall thickness of 1-3 mm compared to the LV's 10 mm. Structurally, it includes an inflow tract, an apical region, and an outflow tract, with its complex shape challenging accurate assessment through two-dimensional imaging. Functionally, the interventricular septum and spiral muscle bundles link the RV and LV, suggesting a shared contractile force between those two chambers[46–48]. RV is predominantly supplied by the right coronary arteries' blood, ensuring a continuous coronary flow throughout the cardiac cycle under normal conditions due to its lower intra-myocardial tissue pressure. However, under excessive pressure overload, the RV's coronary perfusion pattern may start to resemble that of the LV, indicating its adaptability under stress[44].

1.6.3 Contractile function of the RV in the normal state

Furthermore, the contractile function of the RV differs markedly from that of the LV. In the LV, blood ejection involves a concentric contraction of its free wall, while the RV operates through a sequential contraction from the inflow to the outflow tract, relying more on changes in its wall surface and septal distance[49]. Due to its distinct shape and structure, the RV achieves a larger ejection fraction (EF) with smaller wall surface area changes compared to the LV, and uniquely moderates respiratory changes without altering its contractile function[50]. Although RV and LV stroke volumes (SV) are in a similar range due to the nature of circulatory systems,

the RV dynamics leads to a more pronounced reaction to increased pressure afterload, showing a tendency for increased end-diastolic volume and reduced ejection fraction[44].

Moreover, recent insights in RV function, and the complex interactions between the RV free wall, the interventricular septum, and the LV free wall, recognized the importance of the RV's contractile function, especially under increased pulmonary vascular resistance and RV pressure. For instance, right coronary artery occlusion and RV contractile dysfunction, while not significantly impacting systemic hemodynamics under normal circumstances, can lead to systemic hypotension when pulmonary vascular resistance is high. The critical role of the RV was further emphasized during myocardial infarction, where the subsequent findings showed that RV contractile dysfunction, significantly increases morbidity and mortality[44,51].

1.6.4 RV response to acute and chronic pressure increase

RV has a distinct capacity in responding to acute and chronic pressure increase compared to the LV. When exposed to acute pressure overload, the RV's ability is constrained; mirrored in a rapid decline in stroke volume relative to control while mean ejection pressure increase. This limitation is partly due to the thinner RV wall causing higher wall tension compared to LV, when pressure increases. In addition, due to less changes possible in RV shape, it cannot reduce that stress via shape change during rapid contractions. Biochemical differences also exist between RV and LV including myosin isoform, which is associated with the RV being adapted for fast contraction[52].

On the other hand, in chronic pressure overload, the RV's response is notably different. While the adult RV in general, does not tolerate the second exposure to pressure, RVH often occurs in chronic pressure overload, which potentially normalize the RV wall stress[53]. In addition, while the precise advantages or drawbacks are not clear yet, RV dilation may also happen to potentially improve the contractile performance. Biochemical changes, such as reactivation of fetal gene patterns and changes in metabolic and stress-responsive proteins, are observed in animal models of chronic RV pressure overload[54–56], but more human data particularly from RV free wall are needed to fully understand the mechanisms and structural response to the chronic pressure particularly in disease condition.

Furthermore, RV tolerates volume overload to some extent, as it's adapted to handle significant volume changes without impairing its contractile function[57]. However, severe RV dilation can

limit further volume increase, as it also eventually impacts the LV function, like in pulmonary embolism[58]. It again highlights the importance of understanding mechanisms of RV function and hypertrophy in both normal and pathological condition, so that we can develop novel therapeutic approach to reverse and normalize RV function in different disease states.

1.7 Right ventricle remodeling in PAH

Right ventricle (RV) dysfunction can happen in response to variety of pathological conditions, including those causing pressure or volume overload (described above), or due to other abnormalities, such as ischemia or infarction, congenital heart disease or cardiomyopathies[59]. PH stands out as a significant cause of RV dysfunction and failure primarily due to the increased afterload imposed, while in most cases, left heart function remains normal[60]. Given the direct correlation between progressive RV dysfunction and poorer survival outcome, understanding of RV function and its molecular phenotype in PAH patients are essential for effective diagnosis and proper management strategies of this potentially life-threatening condition.

1.7.1 Right ventricular hypertrophy associated with PAH

The healthy RV, characterized by its flexible and thin wall, granting it a natural ability to adjust to gradually increased afterload, due to the rise in pulmonary arterial pressures, commonly seen in PAH[61]. However, despite being highly adaptable, RV function can be compromised when faced with prolonged exposure to elevated pressure. In this condition, the RV has to work harder to pump blood through the constricted vessels, leading to a massive and concentric hypertrophy.

Concentric remodeling is distinguished by an increased mass-to-volume ratio while maintaining systolic and diastolic function close to normal[62], which is identified by hypertrophy mass greater than 35 g/m2 and an inferior wall thickness exceeding 5mm[63]. Consequently, RV is able to maintain the SV, and therefore keeping EF and cardiac output (CO) similar to normal level. Thus, adaptive RVH is also called as compensatory RV hypertrophy, reflecting the maintenance of normal functional outcomes in patients during this phase. Eisenmenger syndrome and congenital pulmonary stenosis are two examples where RV resilience to chronic pressure overload occurs to great extent. In Eisenmenger syndrome, prolonged high pulmonary pressure, and late-onset failure suggests adaptive capabilities, most

likely due to preserved fetal heart structures and compensatory outflow mechanisms, whereas in pulmonary stenosis, the RV generally copes well with the obstruction, and only severe cases lead to RVF[64].

At the cellular and molecular level, the increase in RV mass is primarily due to an increase in cardiomyocyte mass and RV free wall thickness, driven by cardiomyocyte size growth[65], accompanied by minimal RV dilation or fibrosis. This process effectively maintains stroke volume, RVEF, and exercise capacity. The extent to which RVH is maintained is influenced by various factors, including significant metabolic shifts, which is a key hallmark of hypertrophy, as well as conditions like ischemia, fibrosis, and autonomic dysregulation[66]. Many of these influences are under epigenetic control, orchestrated by RV-specific activation of transcription factors such as HIF-1α, cMyc, and FOXO1[67,68]. The distinction between adaptive and maladaptive RVH is further underscored by the molecular characteristics, such as alterations in glucose and fatty acid metabolism, angiogenesis, and adrenergic signaling pathways[69].

Despite all this, little is known about the initial RVH and its benefits in PAH. Besides, the point of RV deterioration and falling into maladaptive hypertrophy is poorly understood, as this adaptation is typically not sustained for long term. The duration of RVH vary significantly among individuals. Indeed, maintaining the compensatory hypertrophy without progressing to RVF depends on multiple factors, such as the severity and progression rate of PAH, underlying causes, individual patient differences in RV structure and function, and the effectiveness of the treatment[70]. In addition, there is a heterogeneity in type of RVH seen in PAH patient, with some perfectly take advantages of the compensated phase, while preserving cardiac output, whereas some other with same hemodynamic stress develop maladaptive RVH, and decompensate[71]. Gender, in particular, appears to play an important role in RV adaptive responses. Studies have shown that female patients with PAH have better RV compensation in the face of a given pulmonary pressure compared with male patients, in which sex hormones might play a role. This results in better RV function, which may explain the better survival of female PAH patients[72,73].

1.7.2 Development of maladaptive hypertrophy and RV failure

As the disease progresses, the increased workload and metabolic demands on the hypertrophied RV can lead to a shift from adaptive to maladaptive remodeling, characterized by dilation, and

reduced contractility, eventually resulting in RVF. In addition, RV fibrosis often occurs in maladaptive RVH, which is accompanied by substantial decreases in RV ejection fraction, increased end-diastolic pressure, decreased cardiac output, and elevated levels of BNP[62]. However, the critical elements and the point at which the compensatory adaptive remodeling ceases to preserve the SV, leading to RV dilatation and subsequent failure are poorly investigated[70].

Similar to RV hypertrophy, RV maladaptation in PAH is also driven by a numerous cellular and molecular changes, including ischemia, fibrosis, adrenergic remodeling, inflammation, dysregulation of T-tubule structure in cardiomyocytes, and mitochondrial metabolic dysfunction, uncoupled glycolysis, and dysregulation of fatty acid oxidation (FAO), which some mirror the alterations observed in the pulmonary vasculature[74–79]. As PAH progresses, increasing RV pressures lead to a decrease in right coronary artery perfusion, and myocardial metabolism shifts from FAO to glycolysis, which is probably a protective response requiring less oxygen[80]. Yet, the challenges arise when coronary perfusion fails to meet the oxygen demands in RVH, leading to ischemia and subsequent RVF. Reduced angiogenesis, possibly driven by elevated reactive oxygen species from mitochondria and a reduction in HIF-1α, adds to this problem[81,82]. The shift to anaerobic metabolism, insufficient capillary network adaptation, myocardial ischemia, and increased myocardial fibrosis collectively contribute to the transition from compensatory RVH to a maladaptive state, compromising RV wall flexibility[83] (Figure 2).

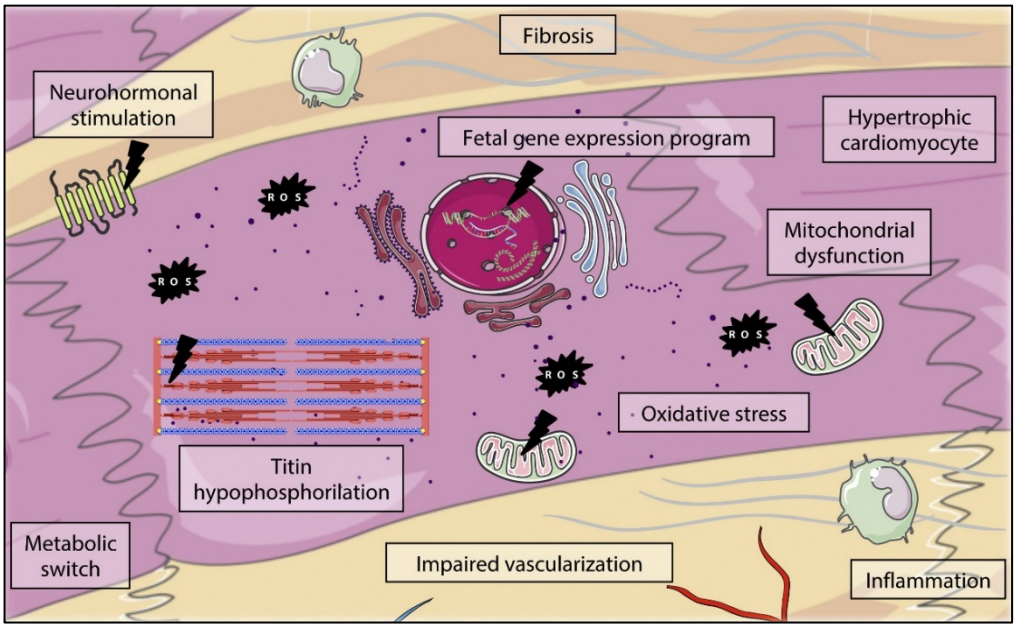

Figure 2: Right ventricle maladaptation process characterized by a myriad of cellular and molecular hallmarks. *The figure is adopted from Aida Llucià-Valldeperas et al; Clinics in Chest Medicine, 2021*[84].

Animal models, especially rodent models of RVH, have been instrumental in delineating the transition between adaptive and maladaptive RVH, as they provide valuable insight in understanding the molecular mechanisms. However, these models demonstrate that the heterogeneity in RVH goes beyond RV mass or the severity of pressure overload. For instance, rodents subjected to pulmonary artery banding (PAB) demonstrated relatively preserved functional capacity compared to those induced by endothelial toxins such as monocrotaline (MCT) or *SU5416*, despite having an identical right ventricular systolic pressure (RVSP)[70].

1.7.3 RV remodeling is heterogeneous in PAH

As with compensated RVH, the development of a maladaptive RV state depends on several factors, and the RV response varies from person to person. In addition to persistent pressure overload, other complex factors such as neurohormonal signalling, increased reactive oxygen and nitrogen species and various inflammatory responses appear to play a role in this transition[41]. Although elevated RV afterload initiates RVH, it is not the only factor leading to RVF, as demonstrated in studies of the MCT-rat model. This model demonstrates a complex interplay between different levels of RVH and RVF, also includes changes in myocardium gene expression and its structural alteration[85,86]. However, the precise mediators affecting this shift, and mechanisms of adaptive RVH progresses to decompensated RVF in PAH remain unclear, underscoring the complexity of RV maladaptation in PAH and highlighting the need for further research. Sex differences and massive extracellular matrix (ECM) remodeling are two major factors contributing to the heterogeneity of RV remodeling associated with PAH, and deeper understanding of these two aspects could help us to unveil the complexity of adaptive to maladaptive RV transition.

1.7.4 Sex differences affect the RV remodeling

It is long known women are more likely to develop PAH than men (~ 3-4:1), but when the disease established, they experience a better prognosis and survival due to more effective RV adaptation[72]. In line with lower RV ejection fraction in males (also in healthy condition), women with PAH often exhibit better hemodynamic characteristics[87]. In addition, female patients showed greater RV end-systolic elastance (Ees) to arterial elastance (Ea) ratio (Ees/Ea) compared to males, indicating enhanced contractility and improved RV-pulmonary artery coupling, even though the afterload was similar[88]. Sex also plays a role in determining the effectiveness of PAH therapies, implying differences between men and women responding to each drug despite having similar reduction in PVR[89,90]. These contrasting findings about the

susceptibility and survival of females with PAH have is widely known as the 'estrogen paradox'[91]. More knowledge coming from animal models of PH, where it has been previously shown that female rats with Su/Hx treatment demonstrated 1.9-fold higher cardiac index, while ovariectomy deteriorated the RV function[92]. More recently, data from MCT-induced model showed that in male rats, treatment with estradiol maintains RV function, through prostacyclin and endothelin-1 pathways, while reducing RV hypertrophy and fibrosis[93–95]. Moreover, in PAB rats, a reduction in ER-α (estrogen receptor) function caused RV-PA uncoupling, worsened diastolic function, and increased RV fibrosis in female, but not male, highlighting ER-α role in RV adaptation[96]. Along with Estrogen, there are a few reports showing the effects of testosterone in PH animal model. Of note, restoring testosterone in castrated mice had negative effects on the RV function[97], while castration itself reduced RV hypertrophy and fibrosis in male MCT-rats[98]. Nevertheless, our understanding of other sex hormones effects on RV remodeling as of pulmonary vasculature in animal models are very limited[73]. Taken together, studies on classical animal models of PH indicate that sex differences significantly influence the development of PH, with protective effects observed in females mainly via estrogen, however some other animal models show opposite effects. The complexity arise from the varying impact of sex hormones on both pulmonary vasculature and cardiac function, but also the complexity of studying the hormonal system with implication of other external factors like age, reproductive cycles, and diet in research[99].

Not only in group 1 PH, but also in other relevant cardio-pulmonary diseases[73] with abnormal RV, it has been increasingly demonstrated that sex differences are mainly mediated by estrogen and its receptors, thereby improving RV function. In female PAH patients that underwent estrogen treatment, elevated Estrogen E2 levels correlated with improved RV contractile performance, indicating potential cardioprotective properties of estrogen[100,101]. However, the mechanisms of how estrogen affects RV function and the underlying molecular changes are not yet fully understood, especially as data from animal models are limited and in some cases contraindicated. Nevertheless, animal models shed light on several important molecular levels at which estrogen could influence the RV. Estrogen enhances RV function by improving mitochondrial density and boosting key regulatory proteins such as PGC-1α, and pro-angiogenic factors, while also reducing oxidative stress, apoptosis, and inflammation by modulating glutathione activation, glycolysis, and cytokines expression such as IL-6 in Sugen 5416+hypoxia (SuHx) rat model[92,102]. E2 is thought to support RV adaptation and delay maladaptive RVH through its action on estrogen receptors (ER-α, and ER-β)[103]. It has been

demonstrated that ER-β expression prevents the conversion of fibroblasts to myofibroblasts, thereby reducing myocardial fibrosis and heart failure progression[104], inhibits stress-induced hypertrophy[105], and promotes cardioprotective protein S-nitrosation, which improves the myocardial function and RV contractility[106]. The protection is also associated with PI3K/Akt signaling pathways, while reducing the effects of calcineurin-related hypertrophy and Ang-II signaling[107,108].

Furthermore, this protective role of estrogen and its derivatives, in particular those related to reducing RV fibrosis, is supported by several studies showing estrogen's effects on collagen regulation, such as decreased collagen I/III ratio[109], in cardiac fibroblasts, while having an opposite effect on the expression levels of collagen genes in male rats fibroblast, suggesting a role for different expression of ERα and ER-β[110]. Estrogen receptors were also shown to be differently regulate the TIMP-MMP balance and therefore mediate the perivascular collagen in female rats[111]. Moreover, E2 treatment counteracted deteriorating RV remodeling in MCT-rats, mitigating fibrosis and enhancing the expression of several ECM enzymes such as ADAM15, ADAM17, and OPN[112]. All these these findings suggest that a potential cardioprotective mechanism may involve the interplay among estrogen, its receptors, and ECM proteins, in which the RV structural remodeling occurs.

However, further clarification is needed regarding the specific mechanisms in which estrogen contributes to cardiac protection in PAH[73], as it is not only the balance of sex hormone balance, but also other mechanisms such as X/Y-chromosome gene expression, epigenetics and inflammation, are also involved with the sexual dimorphism in pathophysiology of PAH and its effect on RV remodeling. Although the alteration of estrogen has been thoroughly investigated in PH animal studies and some clinical studies have focused on estrogen synthesis or signaling, there is very little mechanistic data on the influence of sex in PAH patients and this needs further investigation[91].

1.7.5 ECM remodeling contribution to RV hypertrophy and failure

Extracellular matrix is another important factor playing a pivotal role in the RV remodeling and transition from adaptive to maladaptive state. As illustrated in Figure 2, ECM is directly and indirectly connected with RV hypertrophy and failure in PAH, undergoing a substantial remodeling, influencing disease progression and patient outcomes. ECM plays a crucial role in maintaining cardiac structure and function, and therefore the remodeling of ECM composition

causes a massive myocardium alteration observed RV hypertrophy, which is further accompanied by RV fibrosis in the later stages of maladaptation[113].

It is known that RV remodeling in PAH is associated with disrupted matrix turnover, and increased collagen content, which has been observed in explanted tissues from PAH patients[83,85,114]. The pathological increase in collagen levels leads to a decline in RV compliance and contributes to diastolic dysfunction of the RV[115–117]. Furthermore, ECM is associated with the mechanosensing feature of cardiomyocytes, which detect the elevated pressure overload through integrin changes, activation of ion channels, cellular junctions, and the titin network within the sarcomeres[118]. During adaptive RVH, cardiomyocyte enlargement occurs through the formation of additional sarcomeres, leading to modifications in the muscular trabeculations of the RV free wall. This, in turn, results in the alteration of the orientation of myocardial fibers[65,119,120]. On the other hand, RVF is associated with increased cardiac tissue stiffness and fibrosis, worsening the RV dilation, by pushing against the septum and LV area, thereby further deteriorating cardiac function[84]. The study on animal model showed that sustained pressure overload alone doesn't fully account for the transition from adaptive to maladaptive RV transition. Instead, additional factors including myocardial apoptosis, excessive fibrosis, and increased stiffness are implicated, in which the ECM remodeling is identified as a critical contributing factor[85]. Therefore, PAH-associated RV remodeling involves various changes in the ECM structure, demanding a deeper insight into the cardiac ECM to formulate precise therapeutic approaches aimed at mitigating the disruptive fibrosis observed during the maladaptive stages of RV[121].

The ECM influences RV remodeling in PAH through several primary channels, some of which reflect changes in the pulmonary vasculature, including: 1. Structural support and signaling; 2. ECM remodeling and degradation; 3. Interaction with inflammation; 4. Impaired angiogenesis; and 5. Fibrosis and stiffness[113,122]. However, the multiple roles of ECM in the pathophysiology of RV hypertrophy and failure can be categorized at two levels: First, ECM and mechanical support for cardiac cells to maintain structural integrity. During RV hypertrophy caused by mechanical stress, the geometry of the chamber changes, ultimately leading to diastolic stiffness. Diastolic stiffness, characterized by the ventricles becoming less compliant or more rigid, results in inefficient filling of the ventricles, which in turn leads to significant backflow during right atrial contraction and impedes RV filling in PAH patients, as well as reduced RV SV[123,124].

In the late stages of PAH, this leads to diastolic dysfunction of the RV. The diastolic stiffness is primarily due to stiffening of the RV cardiomyocytes, hypertrophy and sacromeric disorganization[125]. The stiffening of cardiomyocytes is associated with three protein modifications in particular: 1. reduced titin phosphorylation[83], 2. reduced cardiac troponin I phosphorylation, and 3. altered expression and phosphorylation of calcium-handling proteins, impairing diastolic calcium clearance, with the first two more likely to be associated with ECM remodeling[126]. During the second level RV fibrosis occurs, which is primarily characterized by altered synthesis and degradation of ECM components such as collagens, subsequently resulting in increased RV stiffness[127]. Fibrosis is extensively studied in the context of RV dysfunction, and its role in the transition from adaptive to maladaptive RV is profound.

1.7.6 RV Fibrosis and collagen turnover

RV fibrosis affects cardiac function in two ways: First, it acts as a protective mechanism to preserve the structure of the ventricle and prevent excessive stretching of the cardiomyocytes and ventricular dilatation. However, it later becomes maladaptive, leading to increased myocardial stiffness, impairs contraction coupling, and disrupts cardiac contraction due to excessive collagen accumulation and structural alterations within ECM[128,129]. This fibrotic process, is driven by mechanical stress on both fibroblasts and cardiomyocytes, and is marked by an increased collagen I/III ratio, observed as in late-stage RVF[83]. Moreover, fibrosis interferes with cardiac electromechanical coupling during systole by disrupting the collagen network, diminishing gap junctions, and consequently deteriorating myocardial contraction observed in the PAB rat model[130]. This compromised systolic function is complemented by diastolic dysfunction, characterized by a stiffer myocardium due to fibrosis and cardiomyocyte stiffness, hindering early diastolic filling, as described above[131,132].

Currently, histological analysis of human RV fibrosis is limited to postmortem studies, necessitating not only advanced techniques to detect the ECM proteins, but also biomarkers development for early detection. Furthermore, since of the available imaging methods have limitations[133], the potential reversibility of RV fibrosis after interventions remains unclear. It has been reported that following lung transplantation in PAH patients, or after pulmonary arterial endarterectomy or balloon angioplasty in CTEPH patients, RV demonstrates a capacity to reduce its wall thickness[134–136], however, the functional recovery is influenced by previous disease severity and duration[137].

In summary, an accurate assessment of cardiac fibrosis and its relationship with the interplay and remodeling of ECM components in different forms of RV hypertrophy is crucial for understanding the progression from adaptive to maladaptive RV changes. These findings may pave the way for strategies aimed at reversing RV dysfunction by modulating fibrosis. In particular, this is possible through detailed profiling of stage-specific changes in myocardial tissue. In addition, re-expression of the fetal phenotype combined with inefficient metabolism and inadequate contractility and tissue vascularization contributes to RV deterioration along with myocardial fibrosis. Consequently, the cumulative and interrelated cellular and molecular changes in the RV that initially have a beneficial effect but eventually lead to impaired cardiac function in PAH are more difficult to investigate[84].

1.7.7 Necessity of understanding adaptive vs. maladaptive RV in PAH

As briefly mentioned above, whether the RV maladaptation is reversible or not is a debate. In experimental models of PAH, the implementation of a supra-aortic band to elevate aortic pressure has been shown to enhance coronary blood flow and increase right ventricular function. Additionally, reducing RV pressure might also benefit ventricular perfusion. Nevertheless, reducing mPAP in significant levels, is challenging with the available therapies[138]. Therefore, understanding the stage-specific alterations, encompassing both functional and molecular levels, as well as the complex mechanisms driving this transition, is crucial in identifying different types and stages of RVH in PAH, paving the way for innovative strategies to reverse RV remodeling. Moreover, the transition from adaptive hypertrophy to maladaptive remodeling and failure occurs over months to years, emphasizing the importance of early diagnosis and management of PAH to delay the progression of RV dysfunction. The pivotal role of RV dysfunction in PAH is recently being more recognized by the emergence of novel therapeutic strategies focused on reducing RV stress, enhancing, and potentially normalizing its function. Additionally, ongoing efforts to address the intricate clinical challenges associated with this condition further highlight its significance[139].

1.8 Omics-based approaches to investigate RV remodeling in PAH

1.8.1 Using Omics to understand various RV phenotypes in PAH

Recent advances of high-throughput technologies, comprehensive application of genomics, transcriptomics, proteomics, and metabolomics, collectively known as 'omics', allowed for detailed characterization of pulmonary vascular diseases (PVD), including PAH[140]. Indeed, in

the era of precision medicine, deep phenotyping of patients with PVD, beyond their clinical characterization necessitates the incorporation of omics research, and therefore the application of omics provides insight not only into the pathobiology of diseases, but also supports precise clinical phenotyping. Until now, most omics research focusing on PVDs has involved patients with PAH, which have significantly improved our understanding of disease, however, the majority of them performed a single type of omics[140]. However, the integration of data from various omics modalities lately gained importance to achieve a more detailed and comprehensive understanding of molecular phenotypes and cellular functions in PVDs. Further progress in understanding the origins and pathogenesis of PAH, is similarly reliant on comprehensive approaches that utilize data from various modalities, such as innovative molecular -omics profiling[141]. Despite the progress made in understanding PAH pathophysiology, the heterogeneity of disease resemblance in different patients complicates the application of this knowledge to successful treatments.

On the other hand, the progressive RVF being the primary cause of high morbidity and mortality in PAH, necessitate leveraging the omics technologies not only for (re)classifying and diagnosing PAH, but also for identifying new molecular markers specific to RV condition. This helps in effectively aligning patients with current and forthcoming treatments[142]. In addition, the progression from initial stages into the uncoupled failing stage is a continuous process in which various remodeling events happens[84], suggesting the possibility existing distinct phases in adaptive and maladaptive RV remodeling, which in turn require different treatment support required. Consequently, it is crucial to create diagnostic tools capable of evaluating the severity of RV hypertrophy conditions and detecting early maladaptive alterations in RV structure[143,144].

Omics data, deliver a detailed measurement of the genes, transcripts, proteins, and metabolites alterations that govern the structural and functional changes in cardiac cells at different timepoints of disease progression, and therefore they can be utilized to identify molecular profile of PAH associated RV remodeling[140]. Furthermore, subphenotyping approaches in RV omics studies, combined with clinical data, does not only help in decoding the molecular phenotype associated with adaptive to maladaptive RV transition, but also enable identifying RV-specific biomarkers, and enhance prognosis and treatment predictions[140,141]. Therefore, there is urgent need for new omics-based studies emphasizing molecular and translational

medicine to address the current challenges of specificity and effectiveness in managing the disease, in particular RV conditions associated with PAH progression[145].

1.8.2 RV omics data are limited

As reviewed in October 2021[145], relatively lower number of tissue-level omics were generated from patients with PAH, and those available were either from lung or the plasma samples, while no high-throughput data was available from patient's RV tissue. However, omics data from cardiac tissue were available from both mice (9%) and rat (29%) animal models. Even a significant portion of the human omics datasets from lung and blood lacked the information concerning gender and ethnicity. Figure 3 shows the distribution of omics studies on human PAH[145].

Even though since October 2021, more omics including transcriptome, proteome and a few metabolome profiling of RV hypertrophy and failure has been published, most of them used experimental models of PAH[146–151]. In August 2022, Bonnet and his group published the first curated human RV omics study[152], in which they initially performed transcriptome and proteome analysis of hypertrophic RV tissues obtained from PAH patients, and then combined the results with an additional plasma proteome cohort of PAH patients, resulting in identification the specific targets as potential biomarkers of RVF. This human RV dataset later has been reanalyzed in a few other studies to serve other particular questions, and to compare with existing transcriptome from animal models[149,153]. Furthermore, later in 2023, another semi-omics approach centered on hemodynamics was published, aiming to cluster patients with PAH based on their RV hemodynamic profiles[154].

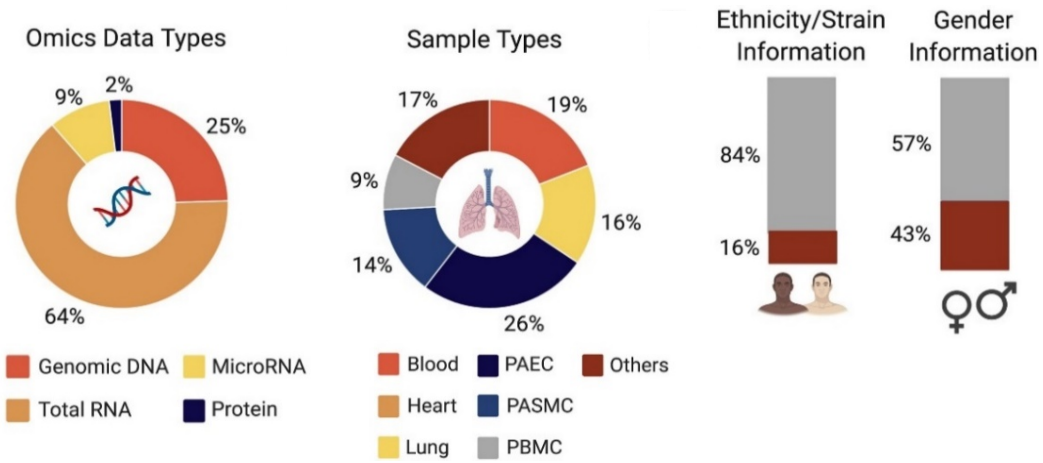

Figure 3: Overview of available public omics data from human PH. *This figure is adopted from Lopez-Crisosto et al, Biochim Biophys Acta Mol Basis Dis. 2021*[145].

Although all current omics datasets of the PAH-associated RV combined with omics analyses of plasma from PAH patients provided a comprehensive understanding of RV dysfunction, revealed several molecular mechanisms associated with unfavorable RV remodeling and identified some novel biomarkers, the scope of human RV research using omics analyses remains very limited due to the difficulty in accessing the RV and therefore the limited number of public datasets available from patients.

1.8.3 Screening RV specific targets and biomarkers using omics studies

Over the years, the discovery of biomarkers has played a crucial role in the treatment of PAH. Among the various omics datasets, proteomic and metabolomic assays, especially on plasma samples, are proving to be the most promising methods for identifying new potential markers and validating known targets. However, many of these studies face the problem of tissue specificity, especially in relation to the RV, and often lack data covering the different stages of PAH progression due to limited[140]. For instance, NT-proBNP serves as a powerful prognostic biomarker in PH, lacks the ability to distinguish between right and left ventricular dysfunction, as it is generated by stressed cardiomyocytes in both locations[141]. Recently a few plasma omics (transcriptome and proteome) studies from different cohorts of PAH patients have focused on the roles of identified markers and their respective RV specificity[60,152,155,156].

While these studies confirmed the expression of specific targets in the RV, performing direct omics analyses (including transcriptomics, epigenomics, proteomics and metabolomics) on human RV tissue and experimental models of RV dysfunction may reveal additional biomarkers directly linked to disease pathology and RV function. To effectively study RV remodeling in PAH using omics, two critical steps are required. First, the integration of multi-omics datasets to distinguish adaptive and maladaptive RV phenotypes by different molecular profiles. By further matching these profiles with clinical data, such as imaging, we can accurately map the dynamics of RV remodeling and identify the critical transition to maladaptive RVH. This requires a comprehensive analysis of patient samples with different RV states, in particular the comparison of compensated and decompensated states. Secondly, the use of integrative omics is essential for the discovery of biomarkers focusing on RV function. Exploring RV-specific biomarkers is critical not only for refining prognosis but also for deepening our understanding of RV therapeutic mechanisms. In addition, this approach helps to categorize PAH patients into different subgroups based on their RV condition, thereby improving the prediction of treatment response and promoting the development of novel interventions[157].

2. AIMS OF THE STUDY

Pulmonary arterial hypertension (PAH) is a progressive disease characterized by abnormal remodeling of the distal pulmonary arteries, leading to increased pulmonary resistance and pressure. This often leads to an adaptive hypertrophic response of the RV, which eventually results in end-stage right heart failure, the major cause of morbidity and mortality in patients with PAH. Therefore, understanding the underlying molecular mechanisms that lead to RV functional deterioration is crucial for the diagnosis, prognosis and development of new therapies in PAH. While many studies have focused on human LV tissue, they cannot be applied to the RV due to differences in embryological origin, shape and ventricular-vascular coupling. On the other hand, limited access to human RV tissue has hindered the investigation of the underlying mechanisms. Moreover, the molecular features of RV remodeling in PAH go beyond conventional clinical knowledge. Therefore, this study aims to investigate the molecular signature of PAH-associated RV remodeling - from adaptive to maladaptive stages - using multi-omics approaches in human RV samples and animal models. By integrating whole transcriptome and plasma proteome datasets across different species, we will be able to identify distinct genes, signaling pathways and upstream regulatory elements associated with different RV hypertrophy phenotypes with the following aims:

- Determination of detailed molecular phenotypes and changes associated with RV adaptation to maladaptation in PAH.
- Performing precise molecular phenotyping of RV remodeling to identify subgroups within compensated and decompensated states of the RV in PAH patients.
- Compare adaptive and maladaptive RV in humans and two animal models and characterize the common phenotype of the maladaptive RV transition.
- Transcriptome analysis in males and females to decipher the sex differences underlying maladaptive RV development.
- To provide a selection of candidate genes associated with different subgroups of RV in PAH together with their validation in the MCT animal model.
- Insights into the pathobiology of progressive RV dysfunction with emphasis on key pathways driving the early to late decompensation phase, with particular reference to remodeling of extracellular matrix (ECM) components.
- Identifying the common pattern of protein expression in patients' plasma that correlates with changes in their RV phenotype
- Identifying potential RV-specific biomarkers that could differentiate between compensated and early or late decompensated RV in PAH patients and correlate with prognosis and clinical outcome

3. MATERIAL AND METHODS:

3.1 Materials

3.1.1 List of kits and equipment

NAME	COMPANY
DC Protein assay kit	BioRad, USA
Supersignal West Femto maximum sensitivity	Thermo Scientific, USA
Western blot chambers	BioRad, USA
Gel blotting paper	Whatman, USA
Polyvinylidene fluoride (PVDF) membrane	Carl Roth, Germany
RNeasy Mini Kit	Qiagen, Germany
miRNeasy Micro Kit	Qiagen, Germany
RNase-free DNase Set	Qiagen, Germany
LabChip GX Touch 24	PerkinElmer
SMARTer Stranded Total RNA-seq kit	Takara Bio
VAHTS Stranded mRNA-seq Library Prep Kit	Vazyme
NextSeq 500 platform	Illumina, USA
Nextseq 2000 platform	Illumina, USA
Olink® Explore 384 Cardiometabolic panel	Olink®, Sweden
Olink Target 96 Cardiometabolic panel	Olink®, Sweden
Olink® Signature Q100	Olink®, Sweden
RNeasy Plus Micro kit	Qiagen, Germany
High Capacity cDNA synthesis kit	Applied Biosystems, USA
Centrifuge	Thermo Scientific, USA
StepOnePlus™ Real-Time PCR System	Thermo Scientific, USA
NanoDrop2000 Spectrophotometer	Thermo Scientific, USA
PCR thermocycler T3000	Biometra, Germany
Precellys Homogenizer	PeQLab, Germany
Microplate reader Infinite 200	TECAN, Germany
Leica microscope DM 2500	Leica, Germany
ImageJ 1.53s	NIH, USA
Leica RM2255 Rotary Microtome	Leica, Germany
Leica EG1160 Tissue Embedding Station	Leica, Germany
ASP200S Advanced Smart VacuumTissue	Leica, Germany
Vevo 3100	Visualsonics, Toronto, Canada
A polyethylene catheter (+pressure transducer)	SciSence catheters, UK
PowerLab	AD Instruments, Australia
PowerLab	
Homeothermic plate	AD Instruments, Spechbach, Germany
19-gauge needle	
silk suture	

3.1.2 List of chemicals and reagents

NAME	COMPANY
iTaq™ Universal SYBR® Green Supermix	BioRad, USA
Mayer's Hematoxylin Solution	Sigma Aldrich, USA
Trichrome Stain Solution	Sigma Aldrich, USA
Methanol	Carl Roth, Germany
Methyl-green	Vector, USA
Milk powder	Carl Roth, Germany
N,N,N′,N′-Tetramethyl-1,2-diaminomethane	Sigma Aldrich, USA
Page Ruler Prestained Protein Ladder	Thermo Scientific, USA
Paraformaldehyde	Carl Roth, Germany
Pertex Mounting Medium	Medite, Germany
Picric acid	AppliChem, Germany
Ponceau S Solution	Sigma Aldrich, USA
Potassium chloride	Carl Roth, Germany
Potassium dihydrogen phosphate	Carl Roth, Germany
Rainbow protein molecular weight marker	AmershamBiosciences, USA
RNase Away	Invitrogen, USA
Scott′s Tap Water Substitute Concentrate 10X	Sigma Aldrich, USA
Sodium bicarbonate	Carl Roth, Germany
Sodium chloride	Carl Roth, Germany
Sodium dodecylsulfate (20% w/v)	Carl Roth, Germany
Sodium hydroxide	Carl Roth, Germany
Stripping Buffer	Thermo Scientific, USA
Tetramethylrhodamine methyl ester (TMRM)	Invitrogen, USA
Tris 0.5 M (pH 6.8)	Amresco, Germany
Tris 1.5M (pH 8.9)	Amresco, Germany
Tris base	Sigma Aldrich, USA
Triton X-100	Carl Roth, Germany
TRIzolTM	Thermo Fisher Scientific, USA
Trypsin Concentrate and Diluent	Life technologies, USA
Tween 20	Sigma, USA
Xylol	Carl Roth, Germany
β mercaptoethanol	Sigma Aldrich, USA
4′,6-Diamidin-2-phenylindol (DAPI)	Invitrogen, USA
Acetic acid, glacial	Sigma, USA
Acetone	Carl Roth, Germany
Acrylamide solution (30%)	Sigma Aldrich, USA
Agarose, low gelling temperature, Type VII	Sigma Aldrich, USA
Ammonium Persulfate (APS)	Sigma Aldrich, USA
Bovine serum albumin (BSA)	Carl Roth, Germany
Bromophenol blue	Roche, Germany
BSA solution (2mg/ml)	BioRad, USA
Chloroform	Carl Roth, Germany
Citrate buffer	Life technologies, USA

Dimethyl sulfoxide	Sigma Aldrich, USA
Diphenylacetohydroxamic acid	Sigma Aldrich, USA
DirectPCR® lysis reagent	Peqlab, Germany
Di-sodium hydrogen phosphate	Carl Roth, Germany
DNA ladder	Fermentas, USA
Ethanol absolute	Carl Roth, Germany
Ethidium Bromide	Carl Roth, Germany
Ethylenediamine-Tetraceticacid (EDTA)	Carl Roth, Germany
Halt™ protease and phosphatase inhibitor	Thermo Fisher Scientific, USA
Hanks' Balanced Salt solution	Thermo Fisher Scientific, USA
Hydrochloric acid	Carl Roth, Germany
Hydrogen peroxide	Merck, Germany
Isopropanol	Carl Roth, Germany
Monocrotaline	Sigma, St. Louis, USA
Isoflurane	Merck, Germany

3.1.3 List of oligonucleotide primers

Transcript	***Forward sequence***	***Reverse sequence***
Human primers		
CCL2	CAGCCAGATGCAATCAATGCC	TGGAATCCTGAACCCACTTCT
IL1B	AGCTACGAATCTCCGACCAC	CGTTATCCCATGTGTCGAAGAA
TGFB1	CGACTCGCCAGAGTGGTTAT	CGGTAGTGAACCCGTTGATGT
FOXM1	ATTGCCCGAGCACTTGGAATCA	CTCAGCTAGCAGCACCTTG
FN1	AGCAGACCCAGCTTAGAGTT	GCAGAAGTGTTTGGGTGACT
NPPA	TGTCCAACGCAGACCTGATG	AGGGCAGATCGATCAGAGGA
TNC	CCAATCATTTGAACAAAGCGGG	TGTAAGCTTTTCCCAAGTGTGT
COL1A1	ACATGTCTAGGGTCTAGACATGTT	ACCTTGCCGTTGTCGCAGAC
ENO3	CCCTGACCTCATACTCCCA	AGGCAGAATCATGAACTCCTG
TIMP1	CCTTCTGCAATTCCGACCT	GCTTGGAACCCTTTATACATCTTG
ANGPT1	AACCAGCCTCCTCTCTCA	GCAGCTGTATCTCAAGTCGAG
CYBB	CTGATTCTCTTGCCAGTCTGT	ATTCCTGTCCAGTTGTCTTCG
HMOX1	TCATGAGGAACTTTCAGAAGGG	TGCGCTCAATCTCCTCCT
ITGB6	GACTCCGGAAACATTCTCCAG	CAAGTTGAGTCCTTCAGTGTCT
IL18	CAGACCTTCCAGATCGCTTC	AATTTCATTGCCACAAAGTTGATG
FGF9	CAGGGAACCAGGAAAGACC	GGGTTAGTTTTTCTGATCCATACA
MMP9	CTTTGAGTCCGGTGGACGAT	TCGCCAGTACTTCCCATCCT
WNT5A	CATGAACCTGCACAACAACG	AGCCAGCATGTCTTCAGG
Rat primers		
Nppa	CCTGGACTGGGGAAGTCAAC	ATCTATCGGAGGGGTCCCAG
Col1A1	CCAGCCGCAAAGAGTCTACAT	AGGGACCCTTAGGCCATTGT
Tgfb1	GCTAATGGTGGACCGCAACA	ACTGCTTCCCGAATGTCTGA
Fn1	CCCCTCCCAGAGAAGTGGT	ATTGGGGTGTGGAAGGGTAAC
Tnc	GCAACCAGGGACAATGTGTG	GGTACTCAGTGACCCGCATC
Ccl2	GCCTGTTGTTCACAGTTGCT	TGTAGTTCTCCAGCCGACTC
Il1B	GCACAGTTCCCCAACTGGTA	TGTCCCGACCATTGCTGTTT
Foxm1	ACCAATATCCAGTGGCTTGG	GCTGTTGATCGCGAACTGTA

ENO3	CTCTACCGACACATTGCAGAC	CCAACTTGTTTCCAGCATGAG
TIMP1	CAGCTTTCTGCAACTCGGA	ACAGCGTCGAATCCTTTGAG
ANGPT1	AGGAAACGAGAAGCAGAACTAC	GTTGTCGTTATCAGCGTCCTT
CYBB	CTCAACCAGAATTCGAAGACAAC	CCACTCCACGTTGAACAGAT
HMOX1	GCCTTCCTGCTCAACATTG	GCGAAGAAACTCTGTCTGTGA
ITGB6	TCACCCAAGAACAAGTCCATC	ACTTCTAGTTCCACCTCAGACC
IL18	CGGAGCATAAATGACCAAGTTC	GCCAGTCCTCTTACTTCACTATC
FGF9	TGGACAGTGGACTCTACCTC	TTCTCTGAACACGCACTCC
MMP9	GAACTCACACAACGTCTTTCAC	GGAGGTCATAGGTCACGTAGG
WNT5A	GCACGCATCCTCATGAACT	ATGGCACTTACAGGCTACATC
Nid1	GTGGAGCAGGATGGGTTCAA	TCCGTGTTGATGGTCAGGTG
C1qtnf1	CTTCCCCTCTGACCTAGCCT	TGTGCCAATCGAATCCTCCC
Sparcl1	CATGGAGCACTGCATAACGC	GTGGTTAAAGCAAGCAGGGC
Megf9	TTGCCAATGCAAACTGGGTG	ATCAGACCGGTTGTTGCACT
Crtac1	GGCTGAGAGAGCCAGAGGA	CCACTCCGTAGTTGAGCTGG

3.1.4 List of primary and secondary antibodies

Antibodies	WB Dilution	Catalog #	Company	Clone number
NID1	(1:500)	PA5-30103	ThermoFisher	Rabbit Polyclonal
MEGF9	(1:1000)	abx027366	Abbexa	Rabbit Polyclonal
CRTAC1	(1:1000)	ab254691	Abcam	Rabbit polyclonal
SPARCL1	(1:200)	sc-514275	Santa Cruz	(G-5): lot# A2615
C1QTNF1/CTRP1	(1:200)	sc-81943	Santa Cruz	(2E7): lot# K0222
NPPA/ANP	(1:200)	sc-515701	Santa Cruz	(F-2): lot# H0822
SPP1/OPN	(1:200)	sc-21742	Santa Cruz	(AKm2A1): lot# F1722
ITGA5	(1:500)	PA5-79529	ThermoFisher	Rabbit Polyclonal
ITGA10	(1:500)	PA5-67829	ThermoFisher	Rabbit Polyclonal
Vinculin	(1:2000)	#4650	Cell Signaling	Rabbit Polyclonal

3.2 Methods

3.2.1 Human samples

3.2.1.1 Ethics

The experimental procedures for using human tissues or cells was in accordance to the principles outlined in the Declaration of Helsinki. Human samples were obtained with the approval of Laval University and the Biosafety and Ethics committees of the University Institute of Cardiology and Respirology of Quebec (CER#20773, CER#20735, CER#21747), and the sample collection as well as experimental procedure were performed according to the preclinical PAH research guidelines[158]. All the patients had previously given the written informed consent, prior to RV tissues collection.

3.2.1.2 Human RV sample collection

Human RV samples collection and the respective clinical measurements including RHC and echocardiography from PAH patients has been performed in collaboration with Sebastien Bonnet, from Laval University.

RV tissues are obtained from initial 45 number of patients (male and female) who were classified as with normal, compensated, or decompensated RV condition, based on clinical background, symptoms and cardiac index. Normal RV samples are obtained from donors with functional RV who had aortic surgery or from autopsy following a sudden death, both from those with no previous record of cardiac deficiency or clinical respiratory disease, and were hospitalized due to other coronary dysfunction such as aortic stenosis. Compensated and decompensated RV samples were collected from biopsy or autopsy of PAH or cardiomyopathy patients with RV hypertrophy records. Echocardiography, RHC measurements (when possible), and criteria for the classification into compensated and decompensated RV samples has been applied as previously described[155]. Briefly, patients with preserved cardiac index (CI, >2.2 L/min/m2), or normal (>=17mm) tricuspid annular plane systolic excursion (TAPSE) were considered as compensated hypertrophy, whereas end-stage PAH patients transplanted or died early with RVF, were considered as with decompensated RV. All the samples were collected either at autopsy from sudden death or at the time of heart/lung transplantation. A summary of main clinical characteristics of patients used for RV transcriptome study is provided in Table 2.

RV condition	sex/age code	CI_RHC (L/min/m2)	TAPSE_3D_echo (mm)
Normal	F43	NA	NA
Normal	M56	NA	NA
Normal	M29	NA	NA
Normal	M31	NA	NA
Normal	F48	NA	NA
Normal	F49	NA	NA
Normal	M64	2.5	22
Normal	M52	2.3	19
Normal	M55	2.57	25
Normal	M55	2.72	20
Normal	F56	2.72	20
Normal	F50	3	20
Normal	M31	2.64	27
Compensated hypertrophy	M 6 months	NA	16
Compensated hypertrophy	F54	NA	20
Compensated hypertrophy	F14	NA	21
Compensated hypertrophy	F 6 months	NA	NA
Compensated hypertrophy	F 8 days	NA	NA
Compensated hypertrophy	F 4 months	NA	NA
Compensated hypertrophy	F33	NA	23
Compensated hypertrophy	F30	NA	16.4
Compensated hypertrophy	M27	NA	10
Compensated hypertrophy	M29	2.54	18
Compensated hypertrophy	F32	3	16
Compensated hypertrophy	F28	2.57	17
Compensated hypertrophy	F23	2.32	19
Compensated hypertrophy	F21	4.36	18
Decompensated_PAH	F54	1.9	17
Decompensated_PAH	M77	3.2	13
Decompensated_PAH	F74	2.5	27
Decompensated_DCM	F25	1.3	10
Decompensated_DCM	F60	2	13
Decompensated_DCM	M42	2.1	6
Decompensated_DCM	M48	2.6	9
Decompensated_DCM	F34	2.14	9
Decompensated_PAH	F57	1.74	15
Decompensated_PAH	F53	1.96	NA
Decompensated_PAH	F76	2.25	16
Decompensated_PAH	M65	2.4	7
Decompensated_PAH	F72	3.36	13

Table 2; Clinical characterization of human RV samples

3.2.1.3 Human plasma sample collection

The clinical measurement of 35 PAH patients in Germany cohort, including MRI and echocardiography, and the subsequent plasma collection has been performed in collaboration with Natascha Sommer, and Khodr Tello from University Clinique in Gießen und Marburg.

Plasma sample collection for the proteome discovery cohort was conducted at the University Hospital Giessen and Marburg, Department of Pneumology and Critical Care Medicine in Germany from 2016 to 2018. This cohort comprised 35 IPAH patients, consisting of 20 individuals with compensated and 15 with decompensated right ventricular states, encompassing both male and female participants. All the patients were enrolled in the "Right Heart 1 trial" (NCT03403868), Germany and has given a written informed consent prior to participation. All the experimental procedures and data collection steps adhered to ethical standards received by the formal approval of the local ethics committee, under the reference AZ 58/15. Detailed patients' clinical information, including age and sex, have been thoroughly documented and can be found in the respective publications[159,160]. The classification of RV states into compensated and decompensated groups was determined based on the ratio of RV end-systolic elastance (Ees) to arterial elastance (Ea), as assessed through cardiac magnetic resonance imaging (MRI), following RHC and echocardiography as previously described[161]. A cutoff value of Ees/Ea = 0.8 was established, in which patients with Ees/Ea >= 0.8 were classified as having a compensated RV state, whereas those with Ees/Ea < 0.8 were identified as with deteriorating RV condition, indicating a decompensated RV state. Fasting blood samples were collected following the MRI and echocardiography and promptly subjected to snap freezing at -80°C, for the subsequent proteomic assay analysis.

The clinical measurement from 61 PAH patients in addition to 56 donors included in UK cohort, and the subsequent plasma collection has been performed in collaboration with Sebastien Bonnet from Laval University, and Allan Lawrie, from university of Sheffield.

The second plasma proteome cohort served as validation cohort was obtained at Sheffield Pulmonary Vascular Unit (UK) from March 2013 to February 2018. This cohort contains blood samples 61 PAH patients (33 IPAH, and 28 CTD-PAH) from both male and female patients, who underwent right heart catheterization (RHC), and were initially characterized as with compensated RV if cardiac index (CO: L/min/m^2) >= 2.2 and as with decompensated RV when cardiac index was below 2.2 L/min/m^2. All experimental procedures were conducted in accordance with the approval of Sheffield Teaching Hospitals Observational Study of Pulmonary Hypertension, Cardiovascular and other Respiratory Disease (UK REC Ref

18/YH/0441) at university of Sheffield, with support from the NIHR Sheffield Clinical Research Facility. Prior to participation, every patient provided informed consent, ensuring their full understanding to take part in the research. Clinically relevant information was extracted from the clinical databases, and the estimated glomerular filtration rate (eGFR) was calculated using the Modification of Diet in Renal Disease formula, as previously described[162]. Detailed patients' clinical information, including age and sex, have been thoroughly documented and can be found in the respective publications[159,163]. To ensure a precise analysis, individuals with a left ventricular ejection fraction below 40%, those with obstructive lung disease, restrictive lung conditions, or perfusion defects on lung scintigraphy, in addition to patients with active or recent (<5 years) cancer were excluded from this cohort. Healthy volunteers and patients without cardiorespiratory disease, including those who underwent right heart catheterization, were enrolled as control group of the cohort (n=56). Fasting blood samples were collected following right heart catheterization measurements, and promptly kept at a temperature of -80°C until they underwent proteomics assay and analysis.

3.2.2 Animal models of RV dysfunction

3.2.2.1 Ethics

Experiments were performed according to the guidelines of the Canadian Council on Animal Care and approved by the Animal Care and Use committees of Laval University (2014-176 and 2018-015). For the animal studies, male and female Sprague Dawley rats (Rattus norvegicus) at age 8-12 weeks, (Charles River Laboratories, Wilmington, MA, USA) were subjected to the treatment protocol as previously described[155].

3.2.2.2 MCT model

The main cohort of monocrotaline (MCT) experiment was performed using male rats exclusively due to their propensity to exhibit more severe pulmonary arterial hypertension (PAH) following MCT treatment[164]. Male Sprague-Dawley rats (250-300g body weight, purchased from Charles River) received a single subcutaneous injection of MCT (60 mg/kg; Sigma, St. Louis, USA, dissolved in 0.5M HCl, and pH was adjusted to 7.4 with 0.5M NaOH), while control rats received equal amount of isotonic saline. After MCT treatment the RV function was monitored weekly using echocardiography, and the final echocardiography measurement was performed the day before the right-heart catheterization. Terminal RHC was performed on anesthetized and closed-chest rats (rats were anesthetized with 2-3% isoflurane)

between week 1 to 5 at the time of sacrifice, or at the end of protocol, following the previously described methodology[165], to measure RV systolic pressure (RVSP), RV end-diastolic pressure (RVEDP), and RV cardiac output. The animals were categorized based on their RV function to the compensated or decompensated RV phase according to CO initially measured by echocardiography, and clinical RV failure signs[155]. Further classification to the early or late decompensated, was done based on additional measurements of RVSP and RVEDP. The maximum experiment procedure was 5 weeks after MCT treatment. After performing the final measurements, the heart, lungs, and other major organs were harvested. The RV was separated from the LV and septum (S) after harvest, to calculate Fulton index (weight ratio of RV/(LV+S))[166], and both were snap-frozen immediately.

Furthermore, in this study, a second batch of rats induced with MCT was utilized, including both male and female subjects, allowed for a comprehensive examination of potential sex-related differences among. Therefore, to consider a common baseline, all the animals in this batch, were treated for only four weeks, in contrast to the first batch, and the right ventricle along with other required organs were harvested and immediately snap-frozen to ensure uniformity in data collection. However, the weekly monitoring process, including assessments via echocardiography and terminal RHC, as well as the classification into compensated and decompensated RV followed the similar methodology as in the first group of MCT-induced rats. All measurements were performed blinded to the samples condition.

3.2.2.3 PAB model

For pulmonary artery banding (PAB)-induced RV failure model, male Sprague-Dawley rats (weighing around 200g) were randomly allocated into two groups: sham (Sham) or PAB. To perform the operation, the rats were anesthetized using isoflurane and subsequently intubated. Following this, a median sternotomy was performed, in order to isolate of the pulmonary artery (PA) from both the aorta and left atrium. The main PA was then banded using silk suture, securely tight against a 19-gauge needle, which was promptly removed. In parallel, sham-operated rats underwent an analogous surgical procedure, but without the constriction of the pulmonary trunk. PAB-operated rats with a peak velocity more than 3.5 m/s at the site of constriction, measured by echocardiography, were considered for inclusion in the current study. During the period of 3 to 8 week post-PAB operation, rats from both the sham and PAB groups were sacrificed or euthanized upon indication of clinical symptoms of RV failure. Echocardiographic assessments, similar to those carried out in the MCT model, were conducted

both weekly, and prior to the sacrifice or euthanasia. Terminal RHC was exclusively performed prior to sacrifice or at the end of the experimental protocol. Since RHC assessments have technical complexity due to the altered shape of the heart and the substantial hypertrophy observed following the banding operation, PAB rats were classified into two groups based on clinical RV failure signs. Those with RV function within an acceptable range, and no sign of failure were considered as "compensated", while "decompensated" was assigned to those PAB rats demonstrating end-stage signs of RV failure. Sham-operated rats with normal RV function were utilized as the control group. Following the assessments, the heart, lungs, and other required organs were harvested. The RV was separated from the LV and septum (S) after harvest, to calculate Fulton index (weight ratio of RV/(LV+S)), and both were snap-frozen immediately. All measurements were performed blinded to the samples condition.

Number of initial animal groups were 30, 30, and 15 for MCT first and second batches, and PAB rats, respectively. Number of samples used for downstream analysis after removing the outliers were 26, 27, and 14 respectively.

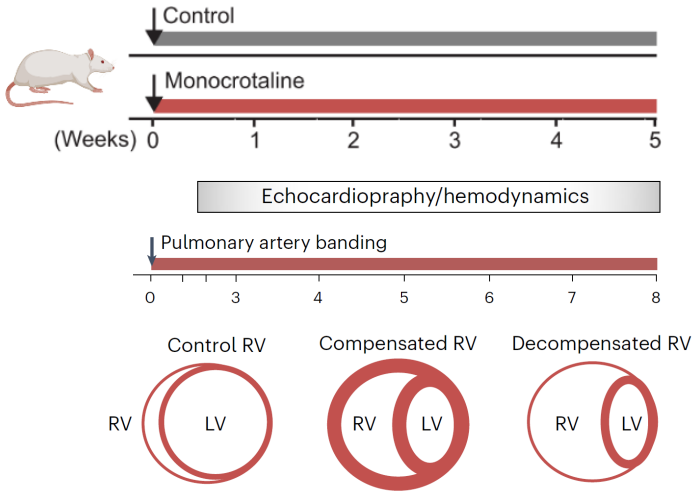

Figure 4: Schematic overview of the RV function screening after Monocrotaline injection or Pulmonary arterial banding model. *This figure is adopted from Khassafi et al, Nature Cardiovascular Research, 2023.*

3.2.2.4 Echocardiography and invasive hemodynamic of rodent models

Echocardiography was conducted utilizing a Vevo 3100 system equipped with a specialized micro-visualization linear probe on SD rats under inhalation anesthesia of isoflurane. (Approximately 200g). Anesthesia induction commenced with 2-3% isoflurane coupled with 100% oxygen (flow rate of 1 L/min.) in an anesthesia induction chamber (Tabletop Laboratory Animal Anesthesia System, Vet Equip Inc. Pleasanton, USA). The rats were then positioned in a supine orientation upon the imaging platform, while their snouts gently kept by a nasal cone linked to the anesthetic apparatus to ensure a steady-state sedation level. Body temperature was

monitored and held at a 37°C, while both eyes received a protective application of ointment to protect against scleral dryness. ECG electrodes were attached to the paws, and chest hair was delicately removed. To optimize ultrasound transmission and reception, a pre-warmed acoustic coupling gel was applied. The echocardiographic evaluations were orchestrated by altering 1.5 to 2.5 percent isoflurane when required, with the aim of maintaining a physiological heart rate (HR) ideally within 400 to 550 beats per minute (bpm). Any deviations from this range prompted a strategic modulation of isoflurane concentration. Following the preparation, Left Ventricular Eccentricity Index (EI) was assessed from B-mode tracings at the level of the papillary muscles. RV parameters such as End-diastolic Right Ventricular Diameter (RVEDD), S wave, Tricuspid Annular Plane Systolic Excursion (TAPSE), Fractional Area Change (FAC), and Cardiac Output (CO) were quantified and analyzed according to current PAH guidelines[167]. All echocardiographic images were captured within a window of 10 to 25 minutes post-anesthesia, with data were obtained in triplicate. Subsequently, the chest wall was gently cleansed using tissue paper, and the tapes securing the paws were removed upon completion of imaging. Anesthesia administration was ceased, allowing rats to recover in an unrestrained manner on a heated ECG pad. Once consciousness was regained, the rats were carefully returned to their respective cages. This comprehensive study adhered strictly to well-established procedures for data acquisition and subsequent measurements, ensuring a robust and standardized approach to the investigative process.

For invasive hemodynamic measurements, rats were anesthetized with 2-3% isoflurane and securely positioned on a homeothermic plate, in a supine posture. Core body temperature was continuously monitored and maintained at 37 ºC via a rectal probe. Between weeks 1 and 5 following MCT injection, and at the end of protocol (for PAB rat only right before sacrifice), rats underwent closed-chest right heart catheterization following the previously published protocol[165]. In brief, a polyethylene catheter linked to a pressure transducer (SciSence catheters, Dover) was used. The catheter was inserted through the right external jugular vein, advanced into the right ventricle to measure the RV systolic pressure and other required pressure parameters. Systemic arterial pressure (SAP) was assessed by catheterizing the left ventricle through the left carotid artery. Data were analyzed using the PowerLab data acquisition system (MPVS-Ultra Single Segment Foundation System, AD Instruments) and LabChart-7 software.

3.2.2.5 Histological characterization of RV hypertrophy

Morphometric assessments were conducted RVs sample that were fixed with a 4% formaldehyde solution. Following fixation, RV samples were embedded in paraffin, then sectioned at 5µm thickness and subsequently stained with hematoxylin-eosin to evaluate RV hypertrophy and Masson trichrome to assess fibrosis. The cross-sectional area of cardiomyocytes was calculated by outlining those cells with discernible nuclei in the hematoxylin-eosin stained sections, employing a method previously detailed[168]. The quantification of both RV fibrosis and the cross-sectional area (CSA) of cardiomyocytes was performed in no less than 10 randomly selected regions using the ImageJ software, to ensure a comprehensive and accurate analysis of the morphological characteristics being investigated.

3.2.3 Bulk RNA sequencing

3.2.3.1 RNA isolation, library preparation and sequencing

Human right ventricular tissues were manually dissected from cardiac biopsies or from autopsies, and immediately snap-frozen for further RNA isolation, adhering to a previously described protocol[155]. Details of human RV sample collection are described in section 3.2.1.2. In the case of RV tissues from rats subjected to MCT treatment or pulmonary artery banding (PAB), collection took place subsequent to hemodynamic measurements, and followed by immediate snap-freezing, according to section 3.2.2.2, and 3.2.2.3, and as previously established method[155].

Subsequently, total RNA was individually isolated from each batch of RV samples using the RNeasy Mini Kit (the miRNeasy Micro Kit was used when available tissue was less than 25mg) from Qiagen. To remove the DNA contamination, the purification process for total RNA in both human and animal tissues was performed in accordance with the guidelines outlined in the RNeasy handbook, involving DNase I digestion using the RNase-Free DNase Set from Qiagen. RNA samples integrity and quantity were assessed by NanoDrop™ 2000 (Thermo Fisher) prior to library preparation. In addition, to ensure RNA integrity, verification was performed using a LabChip© GX Touch™ 24 system (PerkinElmer, based in Waltham, MA, USA), and RNAs with RNA integrity number less than 7.0 were excluded from the subsequent experiments.

For library preparation, approximately 10 ng of human RNA, and 2 µg of total animal RV RNA were utilized as starting material respectively for the SMARTer® Stranded Total RNA-seq Kit - Pico Input Mammalian (Takara Bio, San Jose, CA, USA), for the human RV, and VAHTS

Stranded mRNA-seq Library Prep Kit (Vazyme, Nanjing, China) for animal RV. The procedures strictly followed the manufacturers' provided protocols.

Finally, sequencing was carried out on the Nextseq500 and Nextseq2000 platform from Illumina (San Diego, CA, USA) for human and animal RV samples, respectively. The first batch of human RV tissues underwent paired-end setup, while the remaining datasets utilized a 75-bp single-end setup.

3.2.3.2 Quality control and normalization

The initial step in the data processing pipeline involved the assessment of raw reads for various quality metrics, including adapter content, duplication rates, and overall sequencing quality, which was carried out using FastQC (http://www.bioinformatics.babraham.ac.uk/projects/fastqc/ (2010). Subsequently, Trimmomatic tool (version 0.39) was used to trim reads that showed a drop in quality, defined as falling below a mean quality score of Q15 within a window of five-nucleotides[169]. Following the initial trimming process, reads ranging from 15 to 150 nucleotides in length were selected for further analysis.

The selected reads were then aligned against the Ensembl Human Genome (*hg38*; GRCh38.27), and the Rat Genome (*Rn06*) using STAR mapping tool version 2.6.1. Our alignment process considered for multi-mapping reads and was done with the following parameters: multi-mapping reads, with the parameters: outFilterMismatchNoverLmax: 0.1; outFilterScoreMinOverLread: 0.9; outFilterMatchNminOverLread: 0.9; alignIntronMax: 200000; and outFilterMultimapNmax: 999[170]. Subsequently, total number of reads aligning to annotated genomic regions (genes) were counted using featureCounts tool version 1.6.5 from the *Subread* package[171]. Only those reads that mapped at least partially to one exon were aggregated and counted on a per-gene basis, while reads mapped to multiple genomic regions or genes were excluded from the counting process.

After quality control step for each organism, raw count values underwent separate normalization pipeline using DESeq2 version 1.30.0 in R environment (developed by the Foundation for Statistical Computing in Vienna, Austria)[172], including an additional transformation into regularized logarithm values to facilitate subsequent analyses. For human RV samples, as there were two distinct batches of datasets generated, a batch effect correction was implemented into the normalization step, using the *sva* package[173]. The resulting dataset, which was both normalized and corrected for batch effects, served as the foundational basis for all the further downstream analyses.

3.2.3.3 Downstream gene expression analysis and visualization

After initial steps for quality control and normalization, each datasets were tests for differential expressed genes (DEG) between the possible pairs of compensated and decompensated RV. Differentially expression analysis was performed using the statistical method implemented in DESeq2 package[172]. Genes demonstrating a Benjamini–Hochberg corrected P-value of ≤ 0.05, with a Log2FC (logarithm of fold change) ≥ 0.58 or ≤ -0.58, and a base mean expression ≥ 5, were identified as up or downregulated. Functional annotations of genes were enriched using UniProt data from the (release date: 25.06.2019), leveraging Ensembl gene identifiers from the Universal Protein Resource.

Dimension reduction analyses was conducted on the normalized and regularized-log-transformed counts obtained from DESeq2 assay. This analysis was carried out utilizing the Principal Component Analysis (PCA) implemented *FactoMineR* package within the R environment. Additionally, to verify the quality of samples, both Pearson and Spearman correlation analysis were used to test the correlation within groups, and check for outliers for further analysis. In order to visualize the top differentially regulated genes, as well as correlation scores between the samples, heatmaps were generated using the complexheatmap R package. In assembling the heatmaps of gene expressions, a z-score transformation was applied per row for the normalized count values of all differentially expressed genes. Combinatorial heatmaps were used to visualize the distinct and common deregulated genes, in regards with different pairs of comparison, and significantly altered pathways, between human and rat datasets. In all the heatmap visualizations, samples are distributed unsupervised through the x-axis, which in some cases have been highlighted additionally for their identified subgroups or clusters. In addition, volcano plots were used to illustrate the regulation of DEGs in each specific contrast, using DESeq2 generated Log2 fold changes and adjusted P-values. Violin/Box plots were used to demonstrate the alteration of specific protein coding gene, when necessary, throughout all the samples. R-log-normalized count values were presented in the y-axis, while samples divided into subgroups were indicated along the x-axis.

Unsupervised clustering was applied to a dataset comprising 40 RV samples from humans and 26 samples from the first batch of rats induced with MCT after removing outliers following the quality assessment. K-means method was used for clustering, which is a widely known as unsupervised machine learning algorithm used to identify the distinct subgroups within a dataset only based on the selected features similarities (in this case: gene expression) and

without any other prior knowledge. The process initiates by randomly assigning n number of cluster centroids to the data points, and then associating the rest of data points with the nearest centroids. These centroids are subsequently updated by iteratively recalculating their means based on the assigned data points, and this process continues until meeting a certain balance point. The aim of the algorithm is to minimize the within-cluster sum of squared distances, ultimately resulting in a final clustering solution. While k-means clustering is an efficient method, it can be sensitive to initial parameters, and therefore multiple runs can ensure robustness of the clustering results. To this aim, in this study, different values of initial K were tested on normalized counts to optimize the clustering for each dataset. After careful evaluation, K = 4 was determined as optimal K for rat dataset, while K = 5 was selected for human dataset and the following clustering assignments has been added to the dataset for further analysis.

In the next step, we performed the secondary differential expression analysis using *DESeq2* with the same criteria as in the initial step. However, this DEG analysis involved three different new sets of comparisons. First, a comprehensive DEG analysis between all the new identified clusters (clusters B–E for human and B-D for MCT-induced rat RVs) against control groups of each datasets (cluster A) was performed. Next, distinct comparisons were carried out between subgroups based on their RV state (compensated versus decompensated) but only within their respective clusters. Finally, different one to one DEG analysis was added for the all pairs of comparisons between the clusters.

All sets of lists containing differentially expressed genes were subjected to gene set enrichment analyses using KOBAS version 3[174]. Significantly altered pathways indicated by a corrected False Discovery Rate (FDR) < 0.05 were identified for each pair of comparisons in both directions. The results were visually represent by bar plots summarized mainly for gene ontology terms and KEGG pathways. The bar plots also demonstrate the number of genes that are under- or over-represented within one pathway. After identifying and summarizing the differentially regulated pathways in both datasets, we employed a generalized additive model to demonstrate the relative expression patterns of each set of corresponding genes within one selected pathway, for different RV conditions from normal to late decompensated state. This modeling approach allowed us to capture the elaborate gene expression alteration across different states of RV function.

3.2.3.4 Metadata analysis

Utilizing comprehensive patient background metadata alongside the entire gene expression profile, we conducted a simple generalized linear regression analysis using *glmnet* package[175]. Our initial aim was to identify binominal genes, resulted in a set of 184 candidate genes. Subsequently, we wanted to ascertain whether the expression of any of these genes could be predicted or correlated with any of the provided clinical metadata, including batch, sex, age, and sample type. In addition, to evaluate the model's performance, we implemented a leave-one-out cross-validation approach.

As a result, among the 184 identified binominal genes, only 49 gene had an Area Under the Curve (AUC) greater than 0.6. This observation strongly suggested that batch emerged as the most influential predictor among the chosen variables, masking any discernible effects made by other patients' background features such as age and sex. To further assess the accuracy of prediction for these selected genes, we used standard error estimation which is also implemented in the *glmnet* package. The results indicated an error rate higher than 0.5 for the majority of these genes, implying a notable level of misclassification error. This is largely due to the limited sample size within each group or type, an inevitable challenge in our study given the cohort consists of only 40 patient samples.

3.2.4 Plasma proteome assay (Olink®)

The proteome assessments were performed using a cutting-edge high-throughput multiplex Proximity Extension Assay (PEA) technology developed by Olink® Bioscience, as extensively described in prior studies[176]. In the discovery cohort (German cohort), an Olink Target 96 Cardiometabolic protein panel, version 3601, was used including a comprehensive selection of 92 distinct proteins involved in key biological processes such as cardiac metabolism, cell adhesion, immune response and complement activation. For the validation cohort, an expansive 384-plex panel was utilized (Olink® Explore 384 Cardiometabolic), providing an array of 372 cardio-metabolic proteins in addition to 12 internal control probe detection. This innovative assay uses the epitope-specific binding and hybridization reaction from a manually designed set of paired oligonucleotide antibody probes, which then amplified through quantitative PCR, resulting in the generation of log base-2 normalized protein expression (NPX) values. Notably, higher NPX values indicate a correspondingly elevated expression of the targeted protein,

thereby providing a robust assessment of the proteomic landscape[176], which ensures a precise and reliable quantification of protein levels.

3.2.5 Plasma proteome analysis

3.2.5.1 Differentially protein analysis

After completing the proteome assays and having the Log2 NPX values, we employed the differentially expression analysis to identify the proteins exhibiting altered regulation. In the case of the discovery cohort, unpaired simple t-test was used to compare protein expression levels between two compensated and decompensated RV groups. As the normal distribution per group was hypothesized, to ensure an accurate assessment of the differentially regulation by t-test.

Moving forward, in the validation cohort, which included three distinct RV groups (normal, compensated and decompensated), one-way analysis of variance (ANOVA) was utilized for statistical comparison. Subsequently, the Turkey post-hoc correction method was applied to correct for multiple comparison error. This approach helped to obtain reliable differentially regulated proteins since this cohort contained more than two groups of comparison, which contribute to higher potential variations. However, in the discovery cohort, a deliberate decision was made not to apply correction test to P-values as it contained only two groups of comparison with normal distribution. This strategy was used in order to broaden the scope of protein selection, subjecting to a larger pool of candidates, while the validation cohort has subsequently confirmed the significant differentially regulated protein targets.

3.2.5.2 Integration of candidate proteins with transcriptome

Top 25% proteins from the list of differentially expressed proteins between two groups of patients (decompensated vs compensated RV) was then integrated with two distinct lists of differentially expressed genes from transcriptome analysis (genes with LFC>0.58 and *P.value* <0.05). Then, all the common candidates between these three groups were selected for further assessment, considering their respective differentially expression analysis *P.value* of the proteome assay (=<0.05), in addition to their association with extracellular matrix composition.

3.2.5.3 Functional correlation analysis

To assess the potential correlation between the expression levels of selected proteins with various functional parameters of the right ventricle (RV), a two-step approach was used. First, a simple linear regression model was utilized for cases involving each single RV variable. Subsequently, to avoid the sex/and age impact on the correlation test, a multiple regression model was implemented adjusting for age and sex separately when necessary. The outcomes of regression analyses were reported as the corresponding *P.values* for each individual comparison. This correlation analysis evaluates the potential relationships between RV function and protein expressions, while considering proBNP expression levels as the known indicator of decompensated RV state, as well as the taking the confounding factors such as age and sex into account, ensures the predicted interplay between the expression levels of a single protein and RV function is unbiased and reliable.

3.2.5.4 Random forest model and importance score measurement

A Random Forest (RF) Regression model is utilized to evaluate the performance of subgroup classification by panel of five protein expressions. Initially, we ran the model independently on each PAH cohort, considering all five proteins collectively. Subsequently, we examined various combinations of these proteins. To prevent overfitting, we implemented a 10-fold cross-validation method in combination with our RF model, using the R package 'ranger'[177]. Then, to assess the efficacy of the RF model with respect to each classification combination, we used Receiver Operating Characteristics (ROC) and calculated the Area Under the Curve (AUC). The corresponding *P-values* for each ROCs were determined using the Mann-Whitney (Wilcoxon) test, with the null hypothesis (H0) = "the AUC is equal to 0.5". The following ROC and statistical analysis were performed using the 'verification' package in R[178].

Furthermore, we employed a permutation approach to calculate the importance of variables (in this case, the features represented as single proteins) using the 'ranger' package. This method, which is based on accuracy assessment, allows us to determine the significance of each specific variable by out-of-bag estimation. The results, represented as feature importance score, is defined from the difference between the calculated prediction accuracy, and the accuracy obtained when the measured variable is randomly shuffled and all other variables remain constant. This approach provides valuable insights into the relative importance of individual features (proteins) in the prediction model of RV states.

3.2.5.5 Survival curve analysis

Transplant-free survival was assessed from the time of sampling until either the occurrence of death or lung transplantation surgery, and the data cutoff is set at September 30, 2021. To evaluate the predictive performance of individual proteins or combinations of proteins in determining transplant-free survival, Receiver Operating Characteristics (ROC) curves were used. The ROCs were then used to calculate the optimal threshold values for predicting event-free survival. Logistic regression models were also applied to combine multiple models from different proteins for ROC analysis.

Subsequently, the Kaplan-Meier analysis was used to estimate the transplant-free survival rate, and groups' comparison was performed using the log-rank test, based on the optimal threshold identified through ROC analysis. For the survival curve analyses involving multiple proteins, each patient's proteome profile was assessed, for each protein being counted if its value was equal or exceeded the defined threshold level. Then, the total number of selected proteins surpassing the threshold was reported as sum for each patient, and individuals were subsequently grouped based on this cumulative value. Statistical significance was considered as a level below 5% (=$p<0.05$).

3.2.6 Gene expression quantification by qRT-PCR

Real-time quantitative PCR analyses were conducted following established protocols[179]. In brief, Qiazol in combination with miRNeasy Micro Kit (Qiagen) was used to extract total RNA from both tissues and plasma samples, adhering to the manufacturer's protocol. Subsequently, the obtained total RNA was reverse-transcribed into complementary DNA, and quantitative PCR (qPCR) was performed subsequently, using the appropriate primers. Detailed information and sequences of the utilized oligonucleotide primers can be found in 3.1.3.

For normalization and analysis, either glyceraldehyde 3-phosphate dehydrogenase or 18S ribosomal RNA were used as housekeeping genes. The relative expression levels of each candidate gene were determined using the ΔCt method. The data is presented as average ± standard error of the mean (SEM). To evaluate the normal distribution of the CT values, the Shapiro–Wilk normality test was applied. For comparisons between two groups, the unpaired t-test was utilized when dealing with normally distributed samples, while the Mann–Whitney U-test was employed for non-normally distributed data. In cases where three or more groups

were compared, one-way analysis of variance (ANOVA) was used for normally distributed samples, followed by post-hoc Tukey's multiple comparisons test to correct final *P-values*.

3.2.7 Protein quantification by Western Blotting

RV tissues were initially homogenized in RIPA lysis buffer from Thermo Scientific. The resulting lysate including the extracted proteins from each sample were subsequently quantified, and then segregated using polyacrylamide gels with both 7% and 10% concentrations. The isolated proteins were then transferred onto PVDF membranes. Following a blocking step, the membranes were incubated overnight at a temperature of 4°C with the corresponding primary antibodies. Subsequently, a 2-hour incubation with secondary antibody conjugated with horseradish peroxidase (HRP) was performed. The immune-reactivity was then measured and visualized through chemiluminescence, using the Super signal West Femto substrate solution (Thermo Scientific).

The resulting images were then captured, and developed using the iBright Image reader (Thermo Scientific). Densitometric analysis of the blots was performed using the Fiji Image-J software. Expression levels were quantified by assessing band intensity values, denoted in arbitrary units, and were subsequently normalized to Vinculin, served as a loading control for each blotting. The protein expression values then were compared in decompenated vs compensated RV groups using one-way ANOVA followed by Dunnett's and Turkey's multiple comparisons test to ensure the correction of reported P-values. A detailed list of the antibodies used for the immunoblotting experiment in this study are provided in 3.1.4.

4. RESULTS:

4.1 Hemodynamic assessment and classification of RV function in experimental model of pulmonary arterial hypertension

To identify the molecular profile underlying RV remodeling in the context of PH, we first classified the pathophysiology of RV function into normal, compensated hypertrophy and decompensated failure based on functional and hemodynamic parameters of the RV. To this end, we used two well-known rodent models of PH: monocrotaline (MCT)-induced and pulmonary artery banding (PAB) rat models, both of which represent RV hypertrophy and dilatation associated with PH.

Our hemodynamic results as well as histological morphometric analysis of RV tissue confirmed that considering TPR, RVSP, RVEDP and CO together allowed us to distinguish between two states of RV hypertrophy, compensatory and the majority of decompensated RV specimens (Figure 5a-f). Furthermore, quantification of RV fibrosis and cardiomyocyte cross-sectional area showed a significant increase in decompensated RV (dRV) compared to compensated RV (dRV) of MCT-treated rats (Figure 5g-h).

Figure 5 to Figure 38 are adopted from Khassafi et al, Nature Cardiovascular Research, 2023[159].

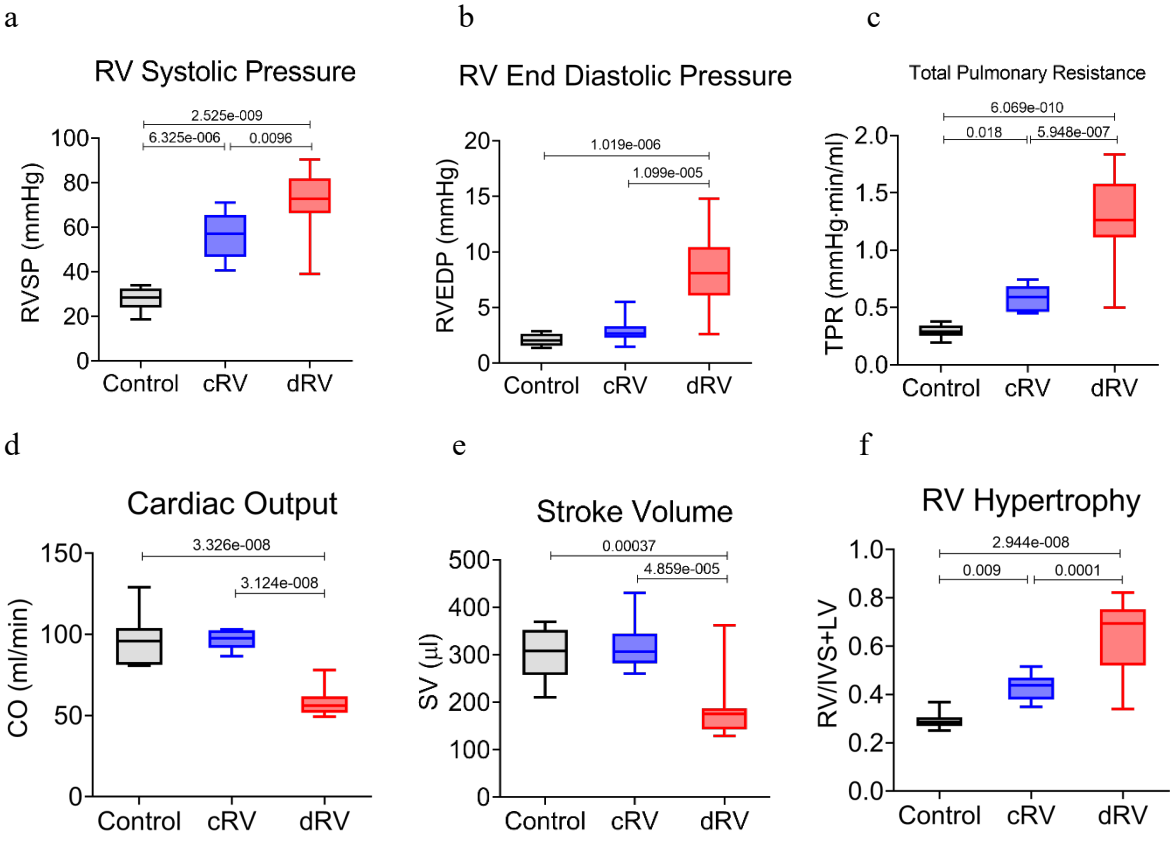

g

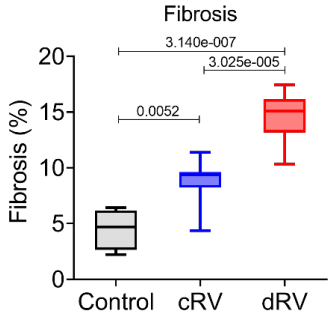

h

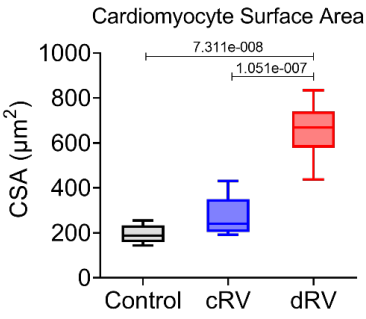

Figure 5: Hemodynamic assessment and RV function in MCT-induced PH rats. (a) RV systolic pressure (RVSP), (b) RV end-diastolic pressure (RVEDP), (c) total pulmonary resistance (TPR), (d) cardiac output (CO), (e) Stroke volume (SV), and (f) RV hypertrophy (calculated as Fulton index = weight ratio of RV and (LV + septum)), measured by closed-chest right heart catheterization. (g) Quantification of cardiac fibrosis from Masson's trichrome staining and (h) cardiomyocyte cross-sectional area (CSA) representing cardiomyocyte hypertrophy from H&E staining. Data are presented as mean ± SEM. (P value has been calculated by one-way ANOVA followed by Tukey's multiple comparisons test). Number of samples (n) in each group of comparison= 10. Number of samples n (control) = 4, n (compensated) = 9, n (decompensated) = 9. In all the box plots: Central bands represents 50% quantile (median), box interquartile ranges: 25–75%, and whiskers set to max/min, 1.5 IQR above/below the box.

4.2 Whole transcriptome profiling of two animal models with PH-associated right ventricle dysfunction

4.2.1 MCT-induced rat models

From hemodynamic classification of RV samples to compensated and decompensated states, we performed RNA sequencing on RV tissues from 30 rats, grouped into control, compensated and decompensated RVs from MCT-induced PH rats. An initial correlation analysis of the total gene expression data identified four samples as outliers based on the total gene expression profiles (Figure 6a,b). After removing four outlier samples from the RNA-seq data, we re-examined the correlation between the remaining 26 samples (Figure 6c) and performed a principal component (PC) analysis for the entire gene expression profile, finding a clear separation between three main groups PC1 contains the highest expression variability of ~25% (Figure 6d).

a

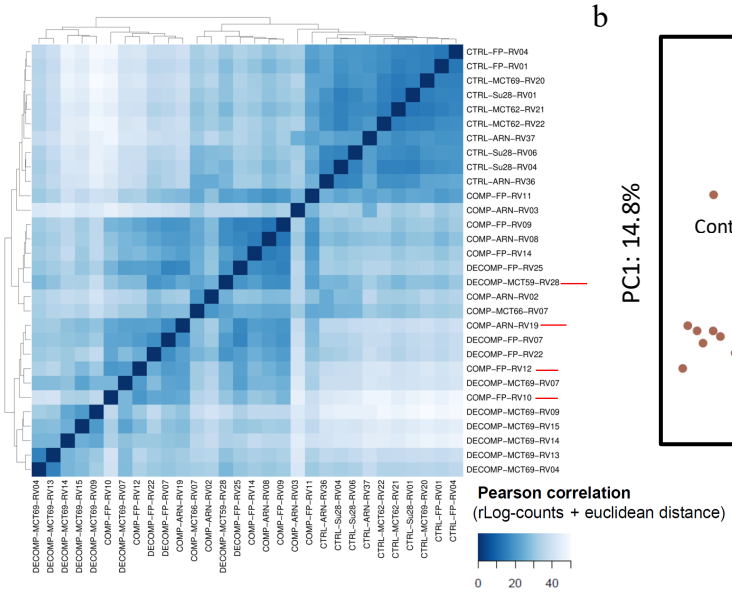

b

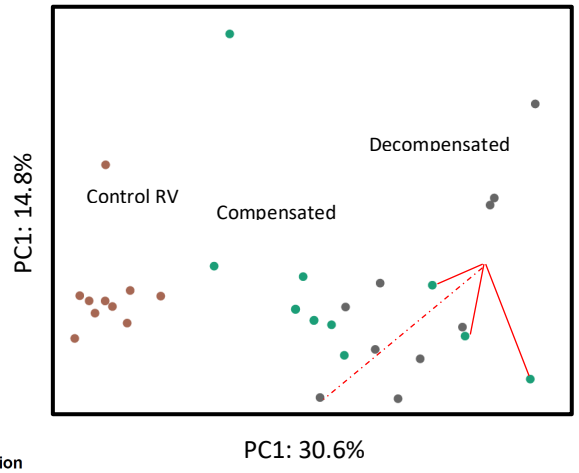

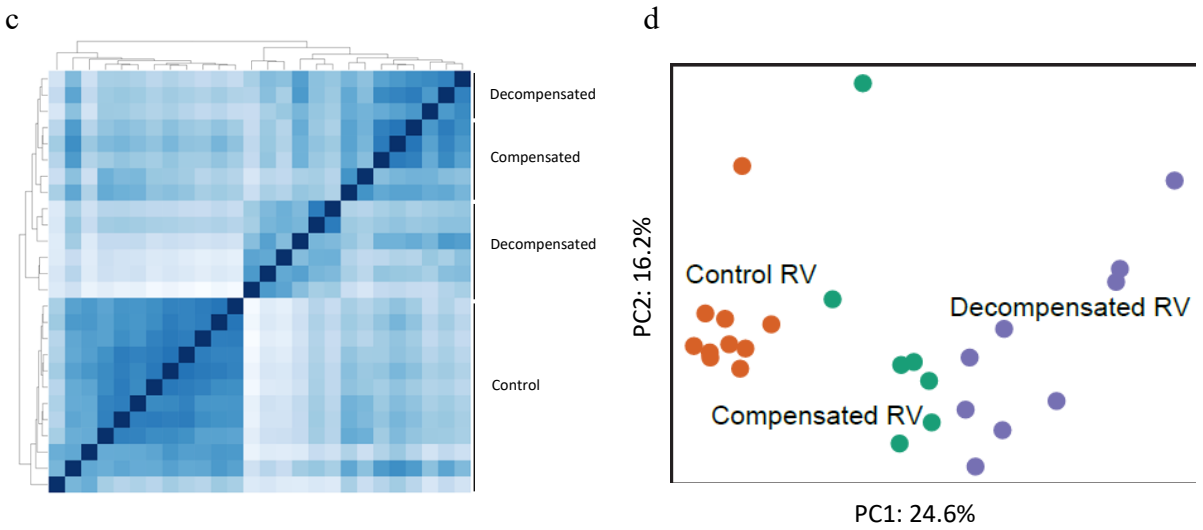

Figure 6: Correlation matrix and Principal Component Analysis (PCA) of whole gene expression profile of MCT-rats with compensated and decompensated RV samples. (a,c) Euclidean distance representing the correlation of regularized log transformation (DESeq2 R-log) of normalized counts for all genes for 30 samples (a), and for 26 samples (c), when four outliers were removed. Genes with sum (counts) <5 are ignored. (b, d) same values of expression used for principal component (PC) analyses using FactoMineR to identify the two groups of genes (=dimensions) incorporating the largest amount of divergence for 30 samples (b), out of which 26 samples weretaken for analysis and (d) four outliers were removed.

Following the initial quality control of samples, we further evaluated the differentially expressed genes (DEG) for 26 samples, which primarily classified into control, compensated and decompensated RV. The analysis of DEGs, performed using the DESeq2 assay as outlined in the Methods section, unveiled significant alterations in transcriptional profiles within compensated (1,383 genes) and decompensated RV (2,991 genes) compared to control RVs. Additionally, 1,159 genes were differentially expressed between decompensated and compensated RV in direct comparisons (Figure 7a-c). Criteria defining significant DEGs were: Basemean expression ≥5, a Log2 Fold Change (LFC) between −0.585 and 0.585, and a false discovery rate (FDR) ≤ 0.05.

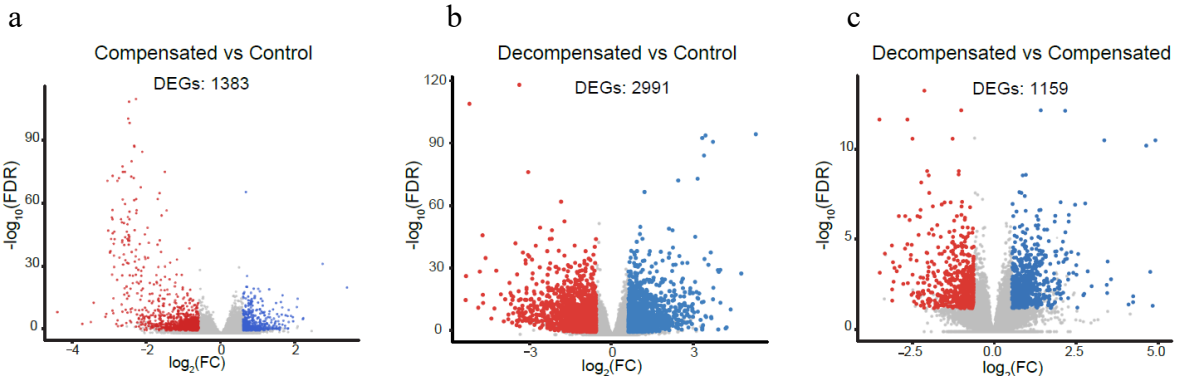

Figure 7: Volcano plots highlighting the DEGs of each pairwise comparison in MCT-rats. (a-c) Volcano plots show the significance of all expressed genes (−log10 false discovery rate (FDR) values on the y axis), plotted against the logarithmic fold change (log2FC values on the x axis), in each pair of comparisons. DESeq normalized counts were used to calculate the log2FC and FDR values. Genes with sum(counts)<5 are ignored. DEGs were

highlighted when base-mean expression ≥ 5; and −0.585 ≤ log2FC ≥ 0.585; and FDR ≤ 0.05 were met. (a) compensated (red) versus control RV (blue), (b) decompensated (red) versus control RV (blue) and (c) decompensated (red) versus compensated RV (blue).

We then performed pathway enrichment analysis to identify the primary molecular and signaling pathways associated with these DEGs. Using Gene Ontology and KEGG pathway analyzes, we demonstrated that in compensated RVs, compared to controls, cell cycle regulation, DNA replication initiation, response to interleukin-1 and cytokine-mediated signaling pathways were upregulated, while transmembrane transport of ions such as Na+, K+ and subsequent cardiomyocyte adrenergic signaling were downregulated. In contrast, in decompensated RVs, many immunological signaling pathways and responses such as T cell aggregation and tumor necrosis factor alpha (TNF-α) regulation were upregulated, whereas in contrast, cardiac conduction and contraction as well as various metabolic processes were markedly downregulated (Figure 8a-b). Furthermore, during the transition from adaptive RV function to maladaptive failure, dysregulations in hypoxia response, ECM-receptor interactions and cell adhesion were detected in addition to the specific signaling pathways dysregulated in each RV state (Figure 8c).

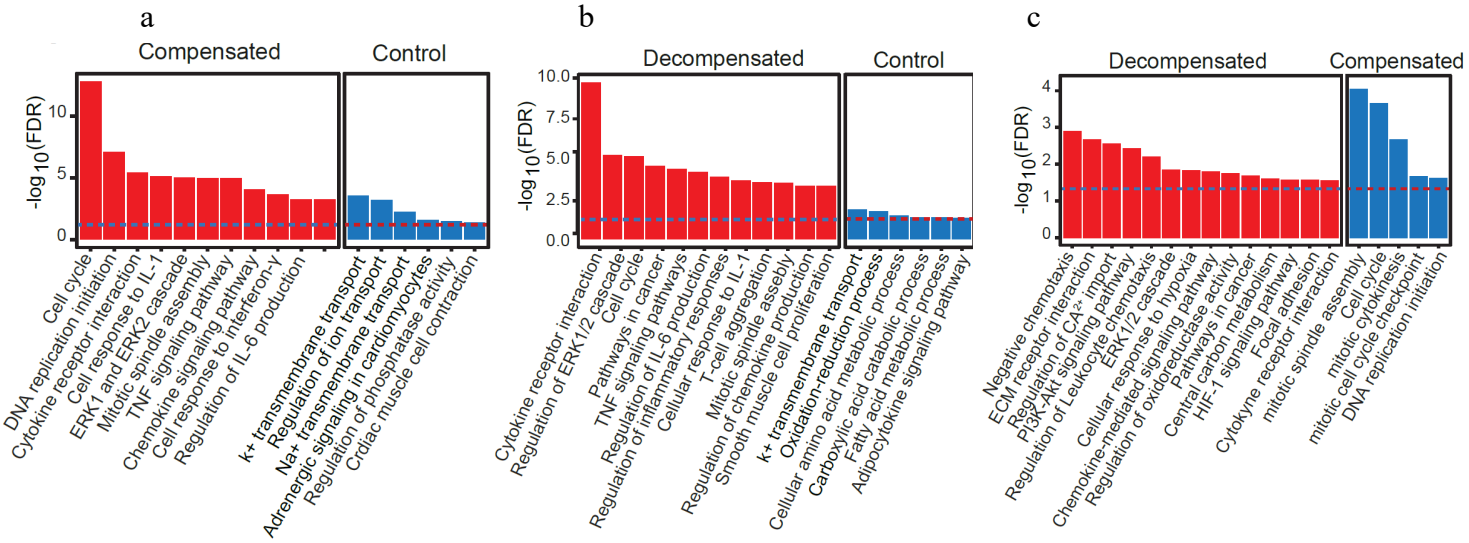

Figure 8: Top selected differentially enriched pathways for each pair of comparisons. (a) Compensated versus control RV, (b) decompensated versus control RV (c) decompensated versus compensated RV. The dashed line represents FDR = 0.05 for the calculated enrichment score.

4.2.2 Pulmonary artery banding (PAB) rat model

Similar to MCT model, male Sprague-Dawley rats underwent for PAB surgery. The obtained RV samples were susequently classified into normal, compensated, and decompensated states, based on exhibiting clinical signs of RV failure, in addition to the echocardiography and closed-

chest right heart catheterization assessments monitored weekly and before sacrifice between week 3 to 8 of experiment[155] (Methods, Figure 4).

PAB-induced RV dysfunction has been evaluated by significant elevations of RVSP, and RV hypertrophy in compensated RV state, while RVEDP was distinctly increased in decompensated RV, which along with clinical RV failure signs enabled us to clearly distinguish the decompensated from compensated RV conditions (Figure 9a-c). However, CO, as well as SV were continuously reduced in PAB rats unlike the MCT model (Figure. 9d-e). Additionally, fibrosis measurement by Masson's trichrome staining, as well as H&E staining for cardiomyocyte cross-sectional area could significantly distinguish compensated and decompensated RV state both from control and one another (Figure 9f-g).

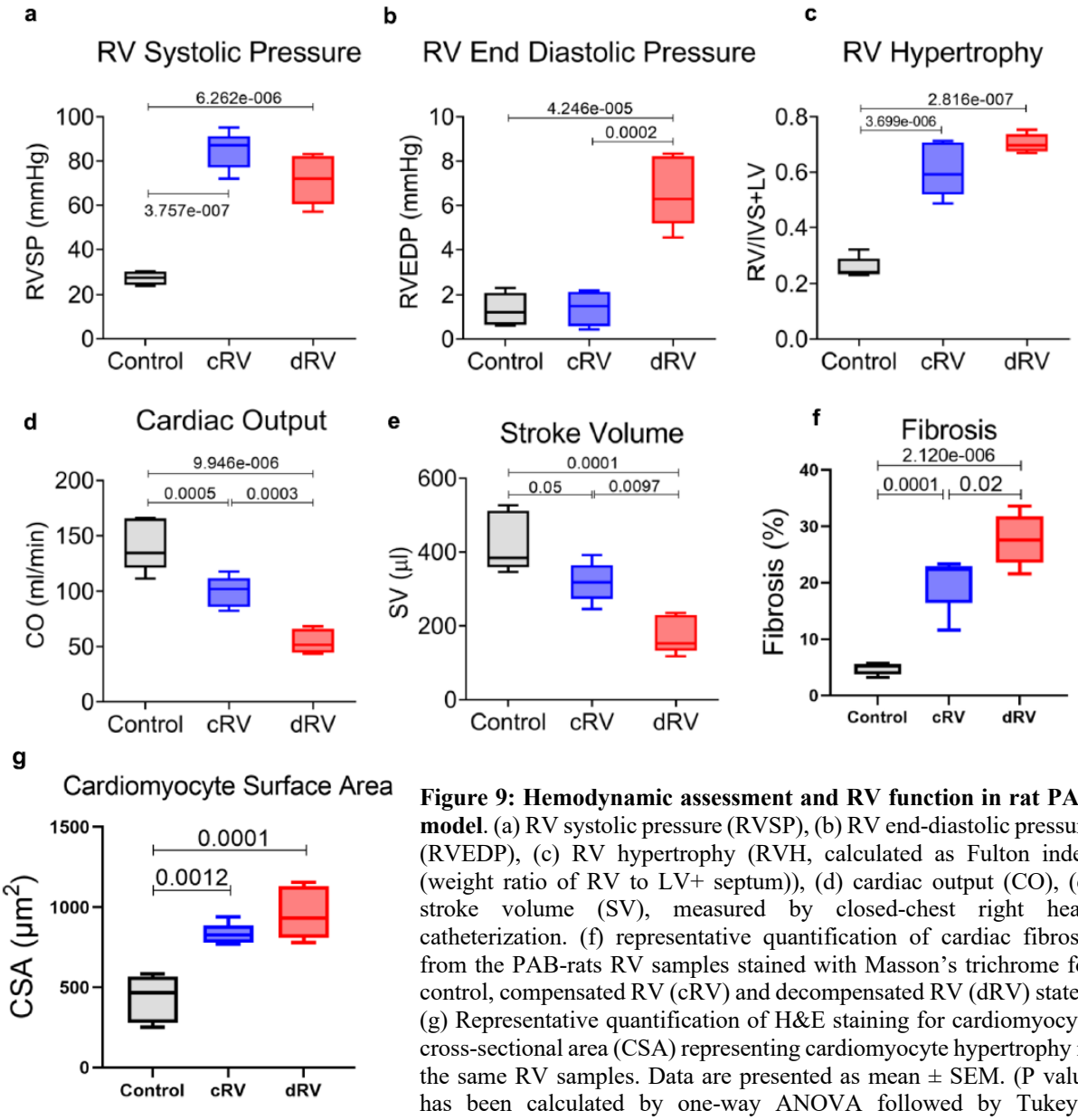

Figure 9: Hemodynamic assessment and RV function in rat PAB model. (a) RV systolic pressure (RVSP), (b) RV end-diastolic pressure (RVEDP), (c) RV hypertrophy (RVH, calculated as Fulton index (weight ratio of RV to LV+ septum)), (d) cardiac output (CO), (e) stroke volume (SV), measured by closed-chest right heart catheterization. (f) representative quantification of cardiac fibrosis from the PAB-rats RV samples stained with Masson's trichrome for control, compensated RV (cRV) and decompensated RV (dRV) states. (g) Representative quantification of H&E staining for cardiomyocyte cross-sectional area (CSA) representing cardiomyocyte hypertrophy in the same RV samples. Data are presented as mean ± SEM. (P value has been calculated by one-way ANOVA followed by Tukey's multiple comparisons test). Number of samples (n) in each group of comparison=5.

Next, we performed total RNA sequencing for 15 RV tissue samples obtained from these selected PAB rats, including 5 samples from each control, compensated and decompensated group. Initial quality control revealed a high correlation between samples from each RV condition, as shown in Figure 10a. However, one of the decompensated RV samples was closer to the compensated RV group and was therefore considered an outlier and removed from the downstream analysis (Figure 10a-b).

Subsequently, we plotted the gene expression profile and the heterogeneity between different groups of RV with PC analysis, which indicated clear distinction between control and compensated RV through both PC1 (30% variation) and PC2 (15.7% variation), and decompensated RV samples were separated majorly by PC2, as more of the PC1 captured the higher heterogeneity within the decompensated RV samples (Figure 10c-d).

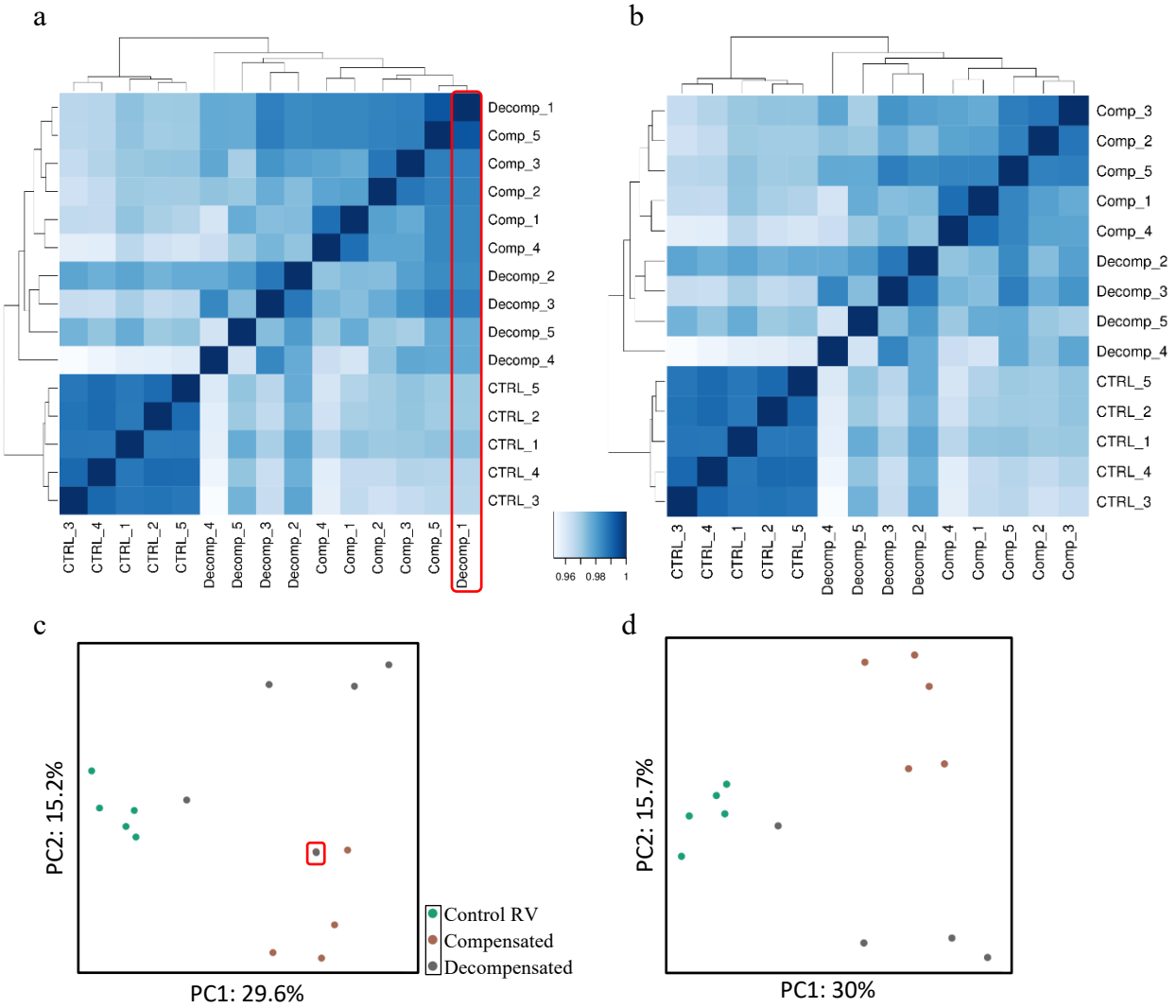

Figure 10: Correlation matrix and Principal Component Analysis (PCA) of whole gene expression profile of PAB-rats with compensated and decompensated RV samples. (a) Spearman correlation heatmap for all the RV samples, depicting decompensated RV-1 as outlier and (b) the same heatmap for 14 RV samples after removing one decompensated RV, which demonstrates high in-group similarity (homogeneity) between the sample. (c-d) PCA plots representing all 15 RV samples (c), and for 14 samples in (d).

DEG analysis revealed 2511 and 1875 genes that are dysregulated in compensated and decompensated RV groups when compared with control RVs, respectively. Lower number of DEGs (445) was detected between decompensated and compensated RVs, which suggest less distinct profiles of decompensation in PAB rats compared with MCT-induced rats RVs (Figure 11a-c). Basemean expression ≥5; −0.585 ≤ log2 fold change (FC) ≥ 0.585; and FDR ≤ 0.05 were the criteria to consider a gene as significant differentially regulated.

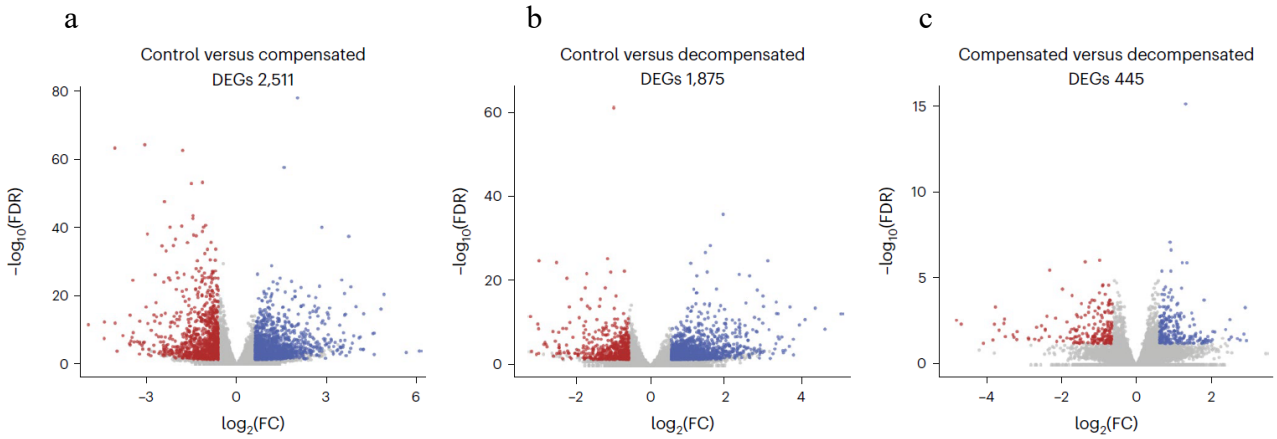

Figure 11: Volcano plots highlighting the DEGs of each pairwise comparison in PAB-rats. (a-c) Volcano plots show the significance of all expressed genes (−log10 false discovery rate (FDR) values on the y axis), plotted against the logarithmic fold change (log2FC values on the x axis), in each pair of comparisons. DESeq normalized counts were used to calculate the log2FC and FDR values and genes with sum (counts)<5 are ignored. DEGs were highlighted when base mean expression ≥ 5; and −0.585 ≤ log2FC ≥ 0.585; and FDR ≤ 0.05 were met. (a) Compensated versus control RV, (b) decompensated versus control RV, and (c) decompensated versus compensated RV.

Enrichment analysis for compensated DEGs compared to control RV samples showed that they are associated with signaling pathways such as cell cycle, DNA replication, and interleukin-1 and interferon-γ responses. Moreover, we found that some signaling pathways such as amino acids, pyruvate and propanoate metabolism were additionally downregulated in the compensated RV samples of PAB (Figure 12a). On the other hand, the decompensated phase of PAB rats was characterized by an enrichment of ECM reorganization, the NF-κB pathway, various immune-related cytokines such as TNF-α, as well as hypoxia and leukocyte aggregation. This pattern is similar to what we observed in MCT rats with decompensated RV (Figure 12b). As mentioned above, fewer genes were differentially regulated in the decompensated RV of PAB rats, which were associated with some distinct signaling pathways such as AMPK signaling, PI3K–Akt signaling, and cAMP metabolism that were upregulated in the decompensated RV, whereas mitotic cell proliferation was downregulated (Figure 12c). This suggests that, in contrast to the distinct molecular phenotypes observed in MCT-associated decompensated RV, there is less transcriptional dysregulation between these primarily characterized compensated and decompensated RVs in PAB rats.

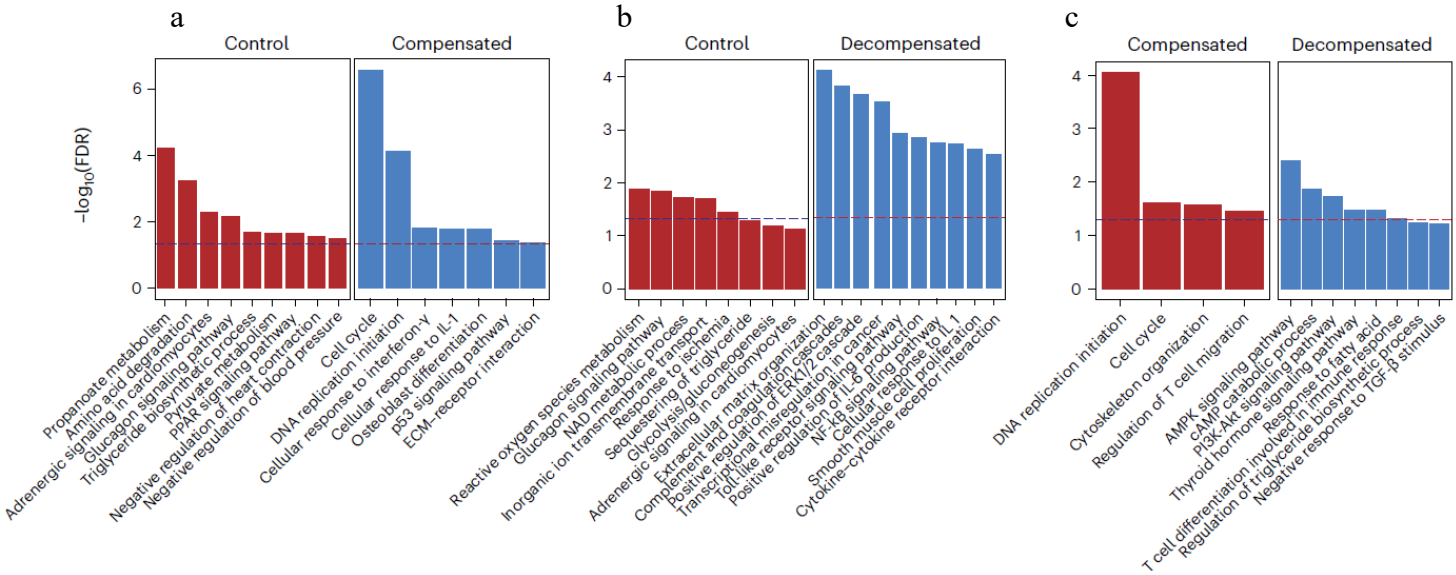

Figure 12: Top selected differentially enriched pathways for each pair of comparisons for PAB-rats RV. (a) Compensated versus control RV, (b) decompensated versus control RV (c) decompensated versus compensated RV. The dashed line represents FDR = 0.05 for the calculated enrichment score.

4.3 Transcriptomic analysis of human adaptive and maladaptive right ventricle

To investigate the specific human RV remodeling and dysfunction associated with PAH, and its relevance to those two described animal models, whole transcriptome profiling was performed on more than 40 human RV tissues that were classified into: control, compensated RV, and decompensated RV states, based on hemodynamic assessment, and clinical symptoms[155] (Table 2, Methods).

Based on this classification, the compensated RV samples resembled the hypertrophic RV stage of patients, while the decompensated RV samples were mostly from failing end-stage hearts, which facilitated the comparison between conditions, including with animal models. The human RV samples were collected at two different time points, resulting in a batch effect in the gene expression profiles of these two groups of samples, regardless of their hemodynamic classification. PC analysis of gene expression before correction shows that samples from two different batches were mainly segregated in PC1 (42%) (Figure 13a), whereas after batch correction of the dataset, RV samples in PC1 and to a lesser extent in PC2 were segregated based on their RV state (decompensated vs. compensated and normal) and not only on the basis of two different batches of sampling (Figure 13b). However, there is still considerable heterogeneity in the dataset in terms of gene expression, particularly within the decompensated RV samples (orange).

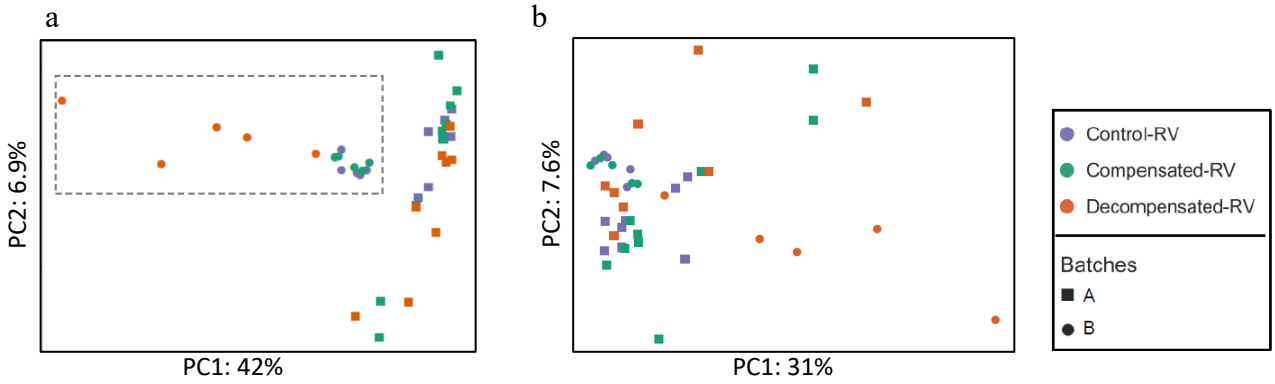

Figure 13: PC analysis show the human RV gene expression dataset (a) before and (b) after batch effect normalization, using *sva* package.

Despite these differences within samples, we found 2027 significantly differentially expressed genes in decompensated RVs compared to control RVs and only 260 DEGs when comparing decompensated and compensated RVs directly (Figure 14a,c). No significant DEGs were found associated with compensated RVs compared to controls. This could possibly be due to heterogeneity within the normal and compensated RV samples.

Enrichment analysis showed that DEGs in decompensated RVs were particularly associated with increased interaction of ECM receptors, cell adhesion molecules and activation of immune cytokines such as TNF-α, while signaling pathways related to the tricarboxylic acid cycle (TCA) and cardiac muscle contraction were markedly downregulated in decompensated RVs, whereas they were upregulated in the compensated RV state (Figure 14b,d).

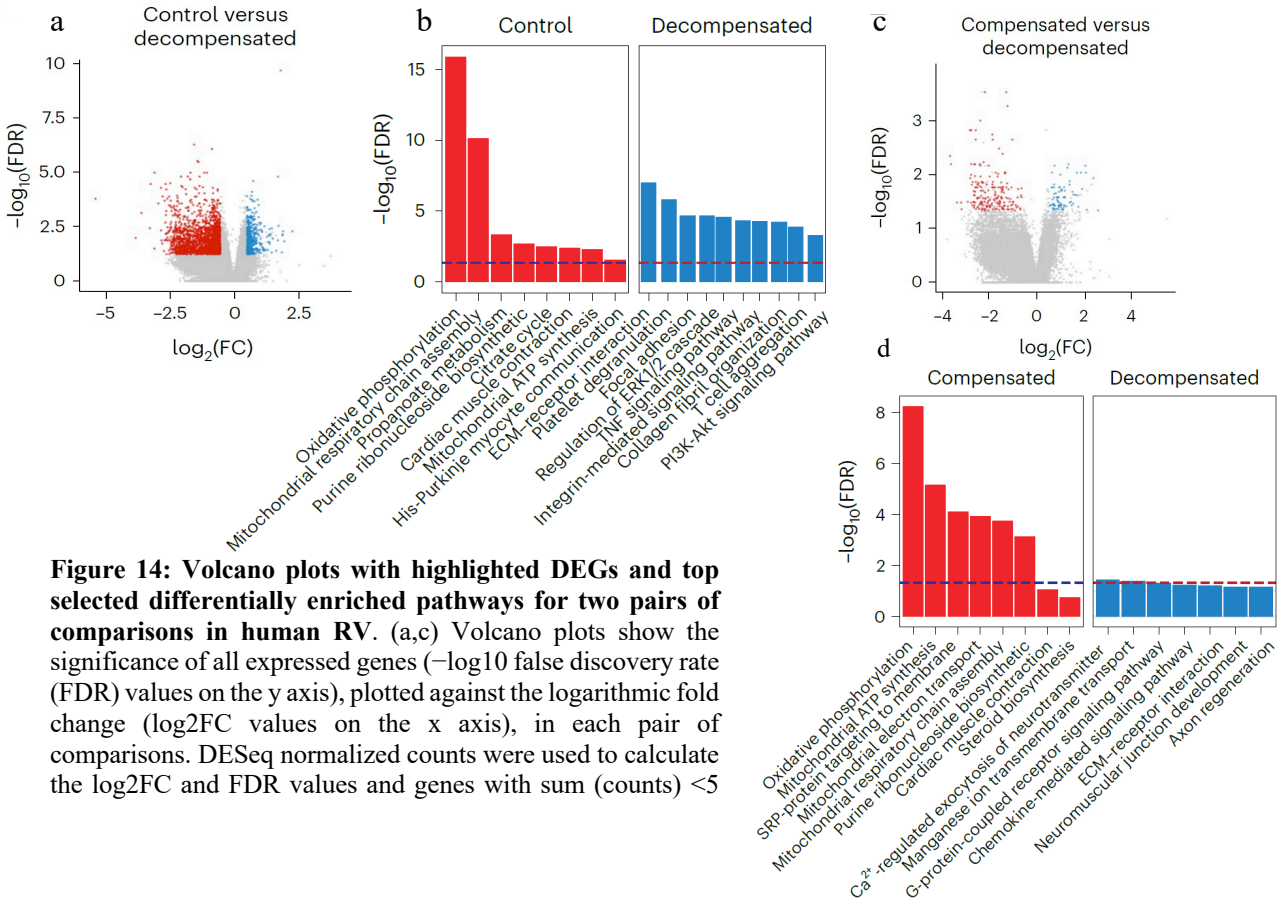

Figure 14: Volcano plots with highlighted DEGs and top selected differentially enriched pathways for two pairs of comparisons in human RV. (a,c) Volcano plots show the significance of all expressed genes (−log10 false discovery rate (FDR) values on the y axis), plotted against the logarithmic fold change (log2FC values on the x axis), in each pair of comparisons. DESeq normalized counts were used to calculate the log2FC and FDR values and genes with sum (counts) <5

are ignored. DEGs were highlighted if base mean expression ≥ 5; and −0.585 ≤ log2FC ≥ 0.585; and FDR ≤ 0.05 were met. (a) Decompensated (blue) versus control RV (red), (c) decompensated (blue) versus compensated RV (red). (b,d) Enriched pathways in decompensated versus control RV (b), and in decompensated versus compensated RV (d). The dashed line represents FDR = 0.05 for the calculated enrichment score.

4.4 Integrative analysis of transcriptome between human RV, and animal models of RV dysfunction

Next, we compared all three transcriptome profiles to determine the similarities and differences between the DEG results of each dataset. As hypothesized, there was a greater similarity in gene expression between the decompensated and control RVs of the two rat models, totaling 1286 genes. Interestingly, when comparing these rat models to humans, there was a higher number of commonly dysregulated genes in the decompensated RV samples from the MCT-induced rats and the samples from the human decompensated RVs compared to the PAB model (522 genes versus 317 genes) (Figure 15a). While both gene sets were significantly enriched for extracellular matrix and integral cell membrane proteins, apoptosis regulation by TNF-α was only upregulated in MCT-induced RV similar to human decompensated RV samples, and not significantly altered in the PAB model. This indicates that the changes in the molecular pathways of MCT-induced decompensated RV closely resemble the pathological condition of the human PAH-associated RV, more than the PAB model. In addition, as mentioned above there were less molecular changes between compensated and decompensated groups in PAB model, which, along with the previous findings[85], shows that PAB model is less reflective of pathological condition of RV failure due to vascular remodeling.

Interestingly, when we performed the enrichment analysis for the co-regulated gene set (259) in decompensated RV between the three datasets, we found that extracellular matrix reorganization was the most upregulated pathway, which was similarly upregulated in all three decompensated profiles. In addition, several cytokine and substrate responses, as well as the mechanisms of vasoconstriction and vasodilation, were commonly regulated in human PAH-associated RVs and in both rat models regardless of the differences in treatment (Figure 15b). Overall, the comparative analysis between the two animal models led us to choose MCT as the preferred model for validating further downstream analyzes of RV remodeling in humans.

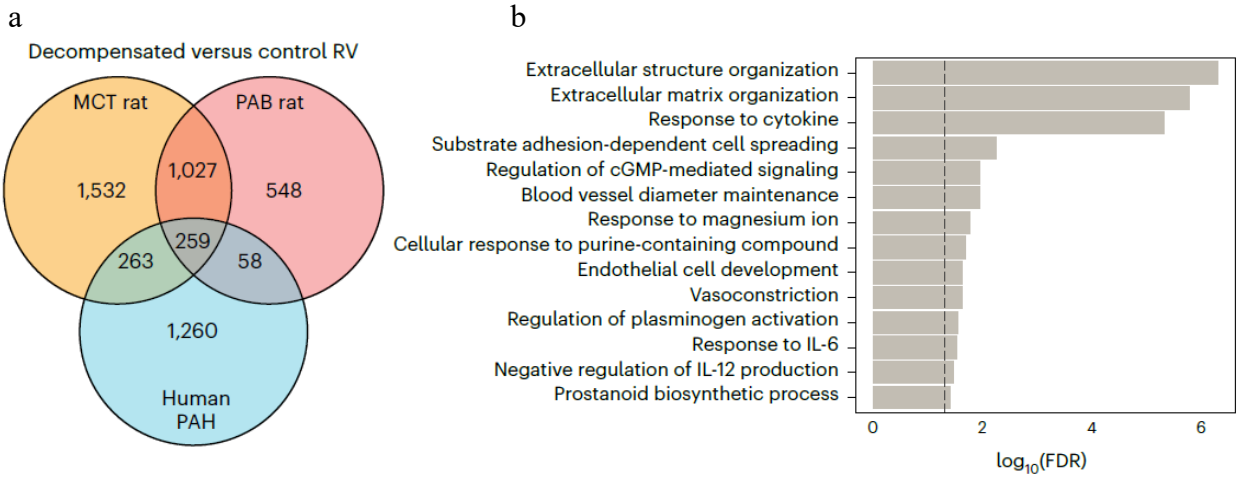

Figure 15: Integrative comparison of transcriptional deregulation in human RVs and two animal models of PH-associated RV dysfunction. (a) Common and distinct DEGs for decompensated RV versus normal RV samples in three transcriptome datasets displayed in the Venn diagram. Orange, MCT rat; red, PAB rat; blue, human decompensated RV versus normal. (b) Top significantly enriched pathways for 259 common DEGs of decompensated versus normal RV samples between all three datasets. The dashed line represents FDR = 0.05.

4.5 How does sex and other clinical factors influence the molecular signature RV remodeling in human PAH?

While we were able to identify the main molecular pathways governing the adaptive to maladaptive remodeling of RV, the considerable diversity and heterogeneity among the human samples hindered us from extracting more information through the transcriptome analysis. Therefore, we decided to employ multiple approaches to initially uncover the extent of this heterogeneity, and investigate how an individual's clinical data might impact their gene expression profile.

4.5.1 Blind assessment of sex, age, sample type and batch by linear regression model

First, using a supervised learning approach (Methods), we investigated whether any of the confounding metadata factors such as sex, age, disease type and sample batches correlated with the specific gene expression pattern observed in compensated and decompensated RV. Using generalized linear regression, we identified 49 genes among the 184 identified bimodal genes with a mean Receiver Operating Characteristic Area-under-the-Curve (ROC AUC) value of ≥ 0.6, indicating that the primary influence comes from the sampling batches, while the gender and age of the participants did not show a significant correlation with the identified genes. This suggests that the analysis of differentially expressed genes and the subsequent assessment of the different subgroups is primarily based on the molecular differences within the RV samples and is not influenced by larger background variations among the patients (Figure 16).

Furthermore, we identified two additional subsets of genes (highlighted in Figure 16), one of which was highly expressed in PAH-decompensated RV and the other had a distinct expression

pattern in compensated RV. However, the small number of samples (40) limits the predictive power of this approach and leads to a high misclassification error in the ROC measurements. Therefore, the 49 identified genes and especially the two PAH-specific gene sets in this analysis were not reliable enough for further downstream speculation unless high-level experimental validation was performed.

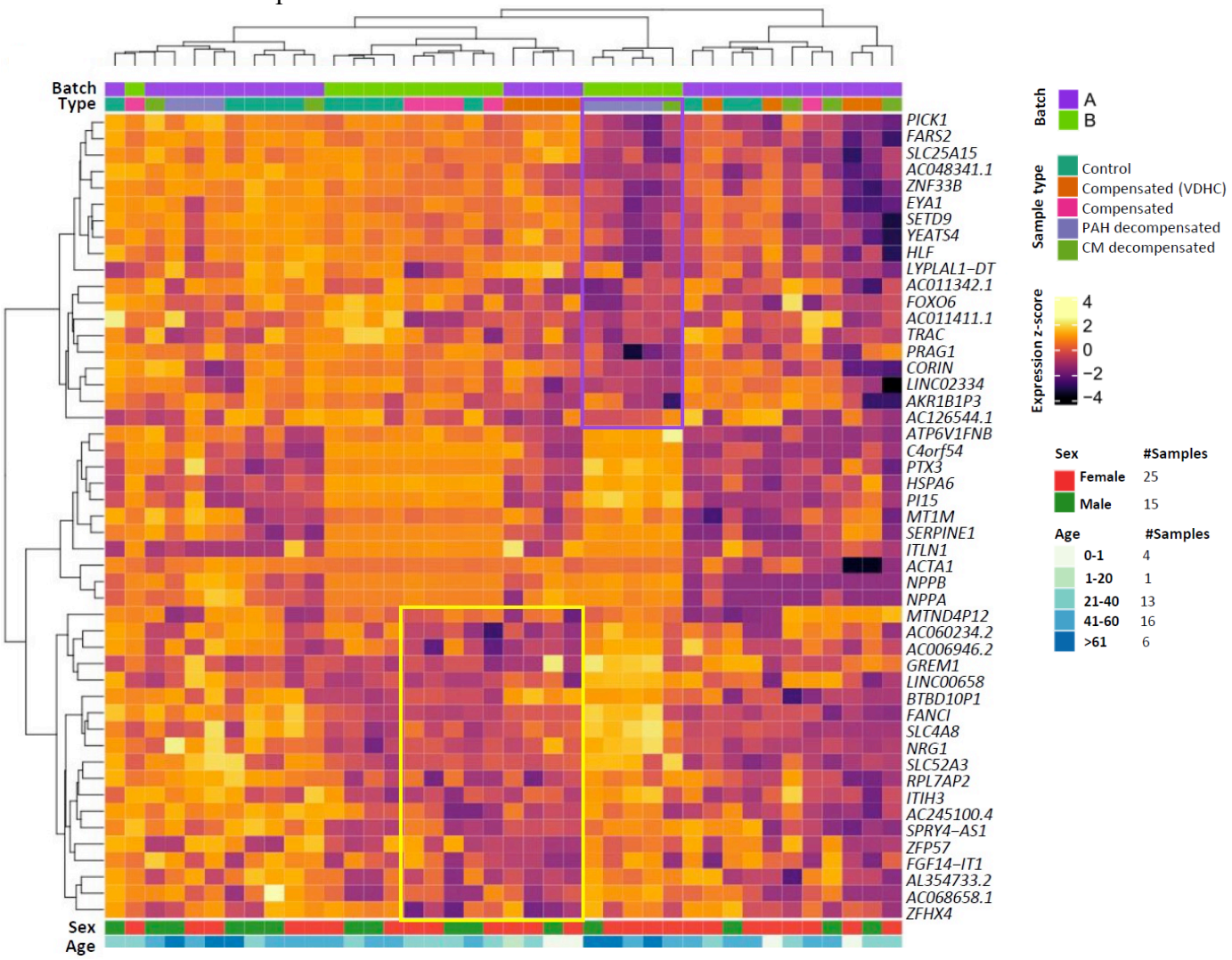

Figure 16: Heatmap illustrating the expression of 49 bimodal genes with AUC > 0.6 from the linear regression model analysis. Two additional subsets of genes has been highlighted which have high correlation with compensated (yellow) and decompensated subgroups (purple), respectively. The assigned k-means clusters of samples shown in this heatmap coming from later clustering analysis. No significant correlations were found with any of the k-means clusters showing that the clusters, are not biased by the sampling batch or patinets' background factors.

4.5.2 Association of sex differences with molecular signature of RV in human patients

As sex differences are suggested to have an impact on RV adaptation and function[72,73], we then focused to the potential differences between the female and male patients in our transcriptome cohort. To this aim, we first used a Fisher's exact test on the male/female inclusion, for both PAH/non-PAH, and compensated/decompensated groups of comparison. We observed that

although there are more females in PAH patients compared to control group (p-value=0.04), there was no significant difference in the number of male/female when comparing the compensated to decompensated RV groups (Figure 17a), and therefore the inclusion of male/female patients does not significantly affect the downstream DEG analysis.

Next, we performed a similar DEG analysis for both compensated and decompensated RV compared to the control group, looking at female and male patients separately. In the female patients, we found no significant changes between compensated and normal RV samples (similar to the comparison with the mixed group). In contrast, we found several profound changes in decompensated RVs compared to control and compensated RVs, such as decreased oxidative phosphorylation and an increase in early estrogen responses, endothelial cell dysfunction, epithelial-to-mesenchymal transition (EMT), and ECM remodeling. The observed changes were very similar to the previous DEG results for the mixed groups, although slightly stronger (Figure 17b). When we performed a similar comparison for the male RV samples only, we initially found no significant number of differentially expressed genes due to the small number of male RVs and the large heterogeneity between these samples. However, considering the p-value < 0.05 to determine the significant DEGs, we identified 739 and 38 differentially regulated genes in the male compensated and decompensated RV groups, respectively. Enrichment analysis of these two groups of genes showed that there was an increase in ECM remodeling, EMT, leukocyte migration and activation, and regulation of apoptosis in the male compensated RV group. In the male decompensated group, these signaling pathways were similarly active, with only a slight increase in apoptosis activation. This finding suggests that male PAH patients may develop maladaptive RV hypertrophy via an alternative pathway that relies primarily on earlier apoptosis activation (Figure 17b).

Finally, we took a closer look at the significant estrogen/progesterone-mediated signaling pathways and found that they were exclusively increased in decompensated RVs from female patients compared to compensated and control RVs, but not in males (Figure 17c). This suggests that sex hormones may have a significant impact on unfavorable RV remodeling in female PAH patients. Not only do female PAH patients take a different pathway to reach a decompensated RV state, but they also maintain the compensated phase of the RV for a longer time due to greater activation of estrogen-mediated signaling pathways. Figure 17d shows a schematic representation of the different pathways by which male and female patients can develop RV hypertrophy and subsequent failure.

a

Condition	Female	Male
Compensated	11	3
Decompensated	9	4
Fisher's exact test *P* value	0.67	
PAH	20	7
Normal	5	8
Fisher's exact test *P* value	0.04	

b

Differentially regulated terms		
Male compensated	Male decompensated	Female decompensated
TNF activation	Regulation of immune response	Hypoxic metabolism
Neutrophil activation	Apoptosis	HIF-1a signaling pathway
Leukocyte migration	Interleukin-4 regulation of apoptosis	KDM2B activity (ChIP–seq)
Apoptosis	NADE-dependent death signaling	Early estrogen response
ECM reorganization	Ficolins activity	EMT activation
Late estrogen respose	Estrogen metabolic pathway*	TGF-beta signaling
EMT activation	Steroid hormone biosynthesis*	TNF activation
	(*downregulation)	Myogenesis
		ECM reorganization

c

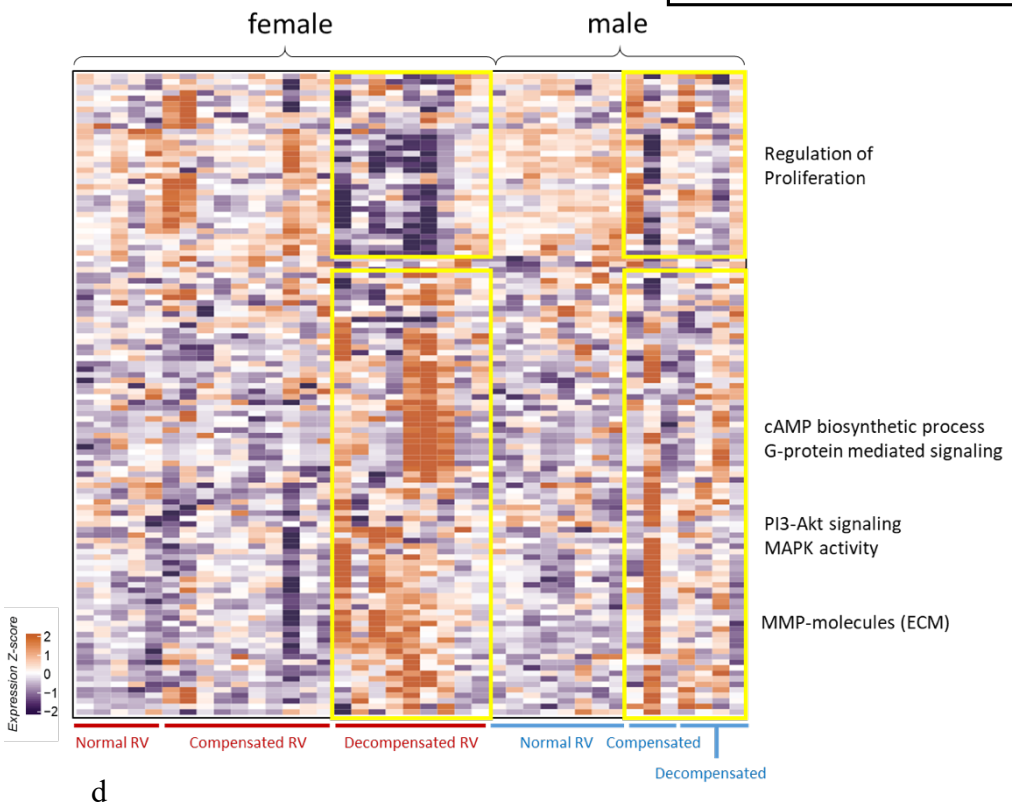

d

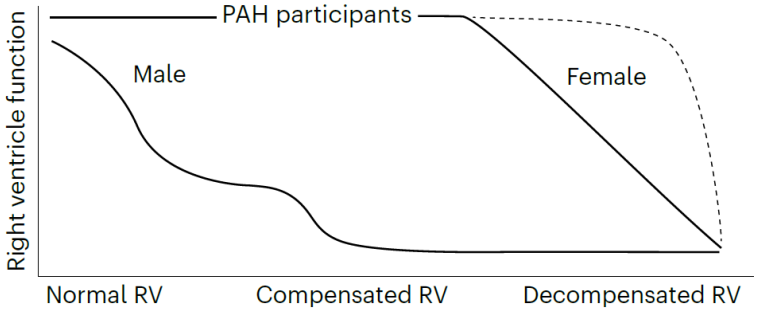

Figure 17: Effects of sex difference on human right ventricular remodeling. (a) Number of patients in each group, separated by sex, and the Fisher's exact test P value for compensated versus decompensated RV and normal-versus-PAH RV pairs. (b) Summary if differentially regulated pathways in RV samples from male and female PAH patients separately. (c) Regulation of 116 differentially regulated genes associated with estrogen and progesterone metabolism (FDR < = 0.05) in all human RV samples. n (normal RV) = F:5, M:8, n (compensated RV) = F:10, M:3, n (decompensated RV) = F:9, M:4. Colors represent the scaled gene expression (rows, z-score). (d) Schematic overview of RV remodeling (and dysfunction) in male and female participants, which shows a different route (longer) for female decompensated RV failure compared with males.

4.5.3 Sex differences influence the molecular mechanism and functional outcome of RV remodeling in MCT-rats

Since re-analysis of the human data suggests that female animals may take a different pathway to develop a decompensated RV state or maintain the compensated RV state longer, we decided to perform RNA sequencing for a second batch of MCT-induced RVs derived from both male and female rats to see if this observation also manifests in animal models. First, we reviewed the primary hemodynamic data and found that RVSP and RVEDP continuously increase from the compensated to the decompensated RV phase in both female and male rats, while CO and also SV do not worsen from the compensated to the decompensated phase in female rats compared to their male counterparts. In addition, the comparison also showed that CO is significantly higher in female rats in the compensated phase than in male compensated RVs, suggesting that compensated hypertrophy is much more pronounced in female rats (Figure 18a-d).

Next, we performed a DEG analysis for all possible contrasts in each female and male group. When comparing the compensated RV with the control group separately in female and male rats, we found similar upregulation of the same signaling pathways, such as the mitotic cell cycle. However, there were differences between female and male decompensated RV groups, although both exhibited similar upregulation of ECM remodeling, which showed that upregulation of calcium signaling, amino acid metabolism, and histone demethylation was observed in male dRV samples (Figure 18e), whereas exclusive enrichment of fatty acid β-oxidation and various inflammatory responses was observed in female decompensated RVs (Figure 18f). In addition, this result revealed some transcription factors differentially enriched in male and female decompensated RVs, such as co-expression of IRF5/EGR2 in males and HIF1A/NFKB1 and activation of ESR1 in female rats (Figure 18e-f). An overview of the altered signaling pathways in male and female MCT-induced rats in relation to their RV dysfunction suggests a delayed maladaptive RV response in female rats that is similar to our observations in human RV hypertrophy and dilation (Figure 18g).

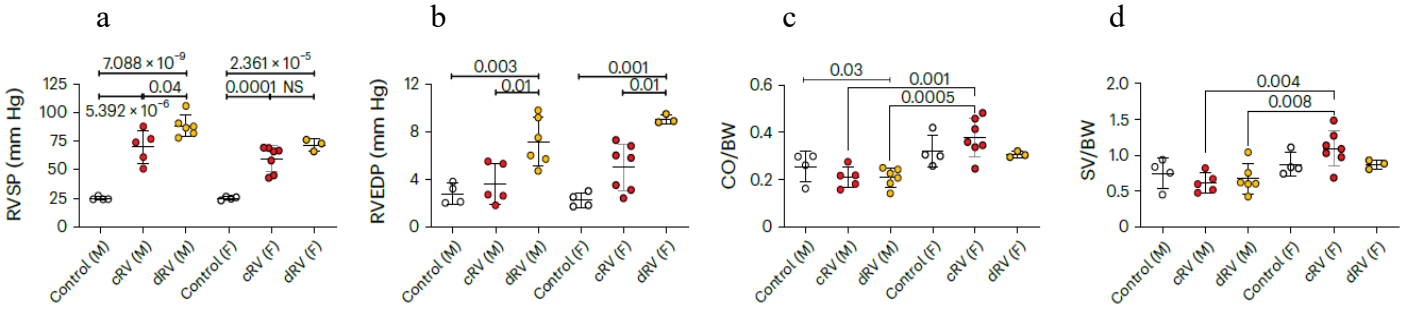

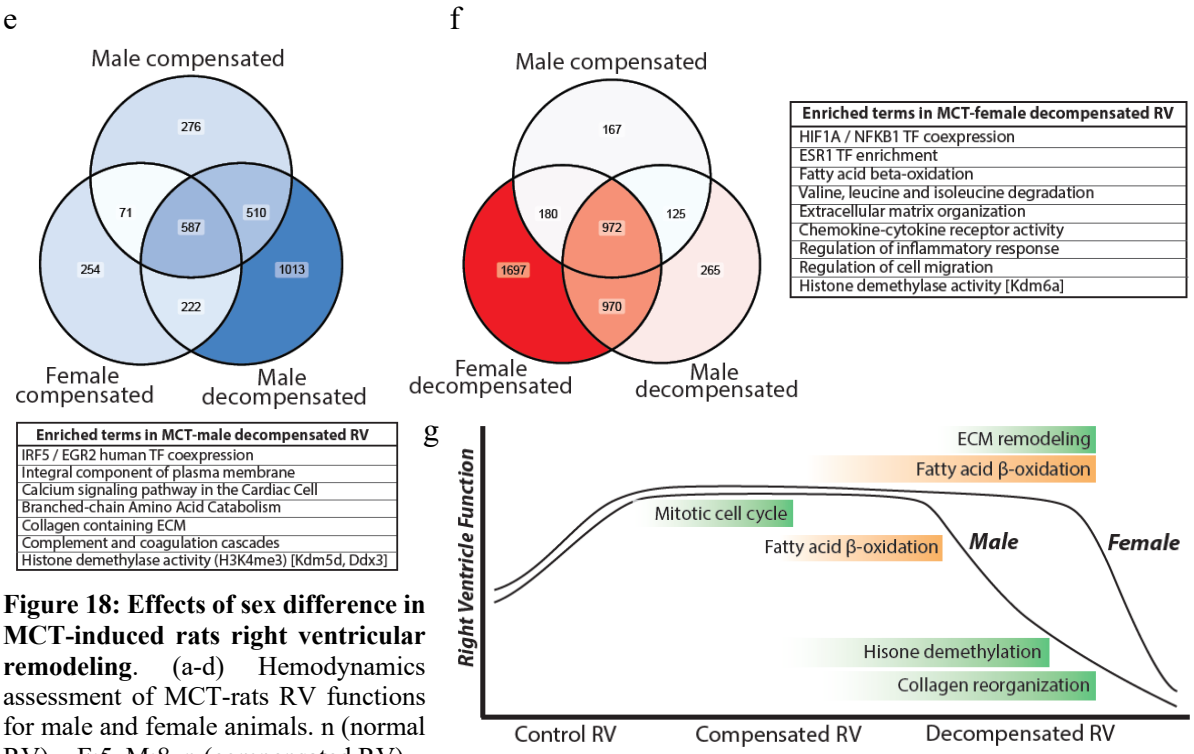

Figure 18: Effects of sex difference in MCT-induced rats right ventricular remodeling. (a-d) Hemodynamics assessment of MCT-rats RV functions for male and female animals. n (normal RV) = F:5, M:8, n (compensated RV) = F:10, M:3, n (decompensated RV) = F:9, M:4. Colors represent the scaled gene expression (rows, z-score). Data are presented as the mean±SEM. *P-value* is calculated by one-way analysis of variance (ANOVA) followed by Tukey's multiple-comparisons test. (e-f) Number of differentially expressed genes and top regulated pathways in male (e) and female (f) rats decompensated RVs. (g) Schematic of RV remodeling in MCT-induced rat model, highlighting the main differentially regulated pathways in male and female animals (green, upregulated; orange, downregulated). cRV, compensated right ventricle; dRV, decompensated right ventricle; M, male; F, female; RVSP, right ventricle systolic pressure; CO, cardiac output; BW, body weight; NS, not significant.

Overall, we concluded that the diversity of factors such as batch, PAH type, sex and age does not seem to influence subsequent changes in gene expression. Nevertheless, sex differences seem to play an important role in the prolonged phase of compensated hypertrophy and delayed onset of maladaptive RV development in female PAH patients, which is also the case in female rats compared to males. However, there are other heterogeneities within the human transcriptome that remain to be explored. This complexity seems to be more related to the different molecular phenotypes of the RV under different conditions. By uncovering these aspects, we aim to understand how the transition from compensated to decompensated RV states occurs, independent of individual differences and their background characteristics.

4.6 Unsupervised clustering unveils the molecular heterogeneity of RV remodeling

4.6.1 Sub-classification of decompensated RV in MCT-induced PH based on transcriptome and hemodynamics

As previously described, the first series of MCT-induced PH was categorized into three groups based on hemodynamic indices and signs of heart failure: normal, compensated, and

decompensated states. However, using unsupervised k-means clustering (Methods), we detected four distinct molecular clusters within the transcriptome of the right ventricle of our MCT-induced rats, the variation of which was detected in two dimensions in PCA (Figure 19a). K-means clustering identified a unique subset among the decompensated RV samples that exhibited a similar molecular phenotype to the compensated group and a distinct transcriptional signature compared to the other decompensated RV samples. Consequently, we classified these three samples as 'early decompensated' RVs, while we labeled the remaining six samples as "late decompensated" RVs (Figure 19b). Using these early and late decompensated subgroups identified by unsupervised clustering, we identified 234 DEGs in early decompensated RVs and 1804 genes in late decompensated RVs, compared with compensated RVs (Figure 19c). We also identified 804 significant DEGs describing the signatures indicating the transition from early to late decompensated RV function in the rat model of MCT-induced pulmonary hypertension. (Figure 19c). Basemean expression ≥5; −0.585 ≤ LFC ≥ 0.585; and FDR ≤ 0.05 were used to determine the significant DEGs as before.

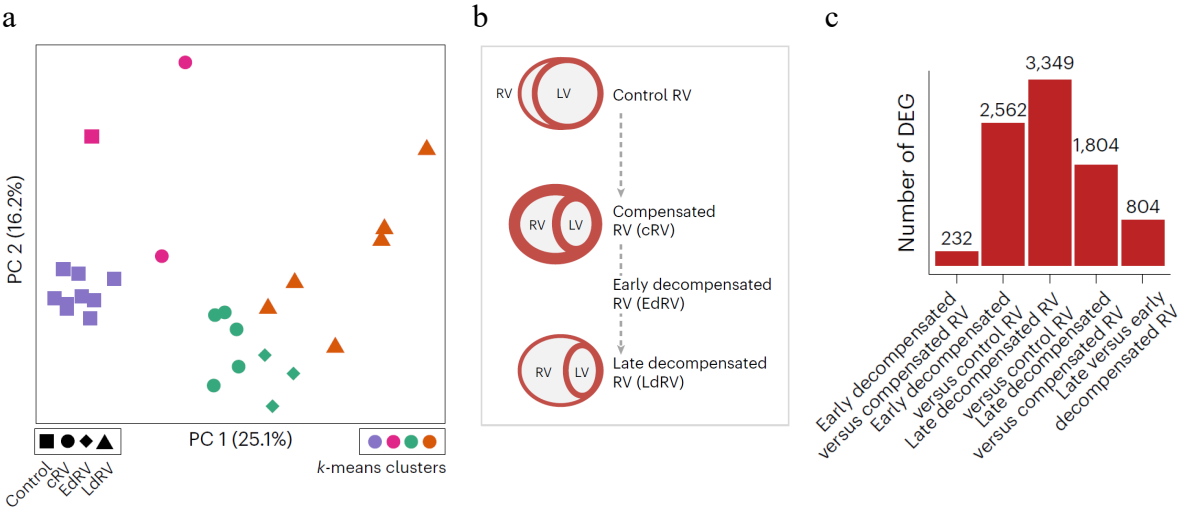

Figure 19: Identification of early decompensated RV based on the transcriptome in MCT-induced pulmonary hypertension. (a) PC analysis was performed on the normalized RNA-seq data, in which the k-means clusters are demonstrated by different colors. Three early-decompensated RV samples clustered with the compensated group, while separated from other decompensated samples on both PCs. Different shapes represent different RV states. (b) Schematic of the classification of RV function into normal, compensated and decompensated, along with a further sub-classification of the decompensated RV into early and late states, based on both transcriptome and hemodynamic features. (c) The number of DEGs that are significantly regulated in each pairwise comparison (base mean expression ≥ 5, −0.585 ≤ log2FC ≥ 0.585, FDR ≤ 0.05).

Similar to previously described, DEGs in compensated RVs were prominently associated with cell cycle regulation, interaction with cytokine receptors, ERK1/2 cascade, cell activation in immune responses (such as T cells), TNF signaling pathway, and regulation of interleukin and interferon responses compared to controls. In addition, the subsequent progression from compensated RV to early decompensated RV was characterized by a decrease in triglyceride

metabolism, fatty acid β-oxidation and cell cycle regulation (Figure 20a). In contrast, there was a significant association between late decompensated RV and a substantial increase in ECM and collagen network reorganization, activation of cytokines and regulation of the hypoxia response (Figure 20a).

a

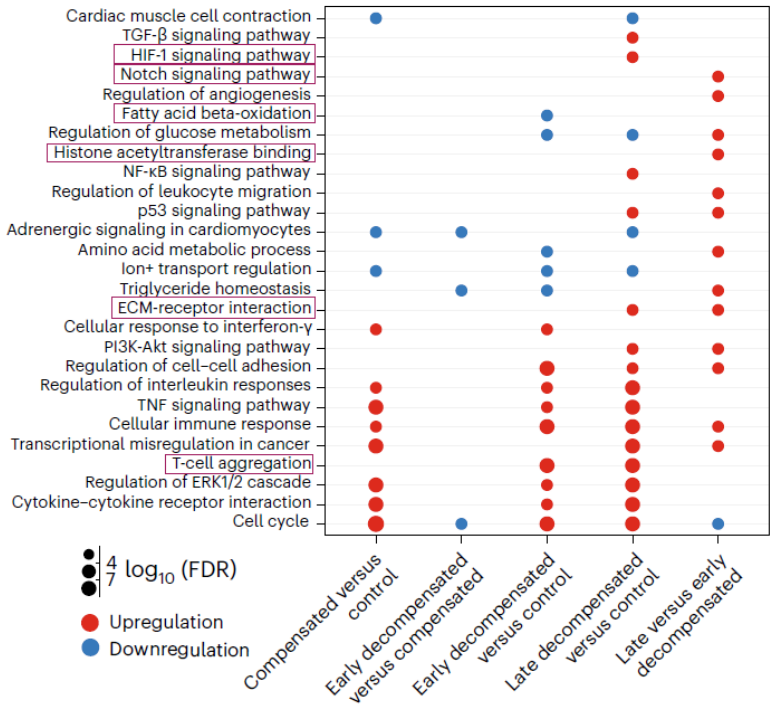

b

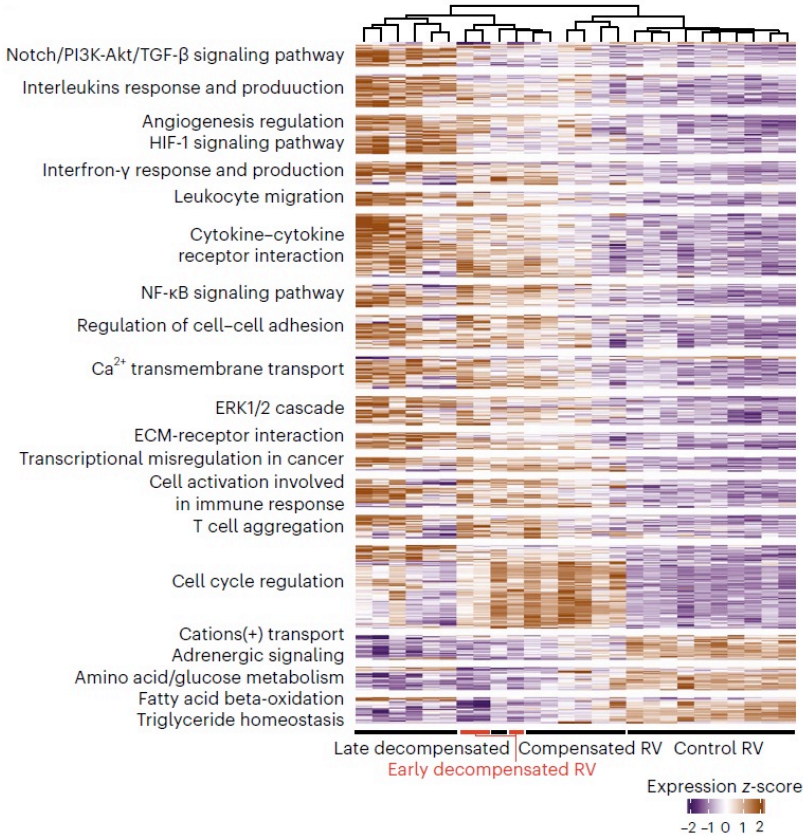

Figure 20; Cumulative gene set enrichment analysis and corresponding gene expression. (a) The integrative dot plot demonstrates the shortlisted important pathways differentially regulated in each pair of RV subgroups. Distinguishing pathways regarding early- to late-decompensated RV transition are highlighted in red. One-sided Fisher's exact test was used for all the enrichment analysis. FDR-corrected P value with Benjamini Hochberg method was used for multiple-hypothesis testing. (b) Scaled gene expression (z-score) representation of the 576 cumulative DEGs corresponding to all the altered pathways associated with the transition from compensated to early- and late-decompensated RV in MCT-induced PH. Different groups of biological terms with similar regulation levels are highlighted along the y axis.

Furthermore, additional glucose and amino acid metabolism was detected in the late decompensated RV. This confirms the occurrence of a hypoxic metabolic shift during the transition from the early to the late stage of RV maladaptation. The cumulative set of 576 differentially regulated genes associated with the selected differentially enriched metabolic pathways in MCT-induced RV remodeling is shown in Figure 20b.

Using the information derived from transcriptome clustering and subsequent enrichment analysis, we were able to confirm the transcriptional landscape underlying the transition from compensated to early and late decompensated RV phases in MCT-induced rats.

We then re-evaluated the hemodynamic data from MCT-induced PH rats to determine if there was a correlation between the transcriptomic features of early decompensated RV and their hemodynamic state. Interestingly, we found that RVSP, RVEDP and RV hypertrophy hardly change between the compensated and early decompensated RV state (Figure 21a, c, d), whereas a significant decrease in CO (and to a lesser extent SV) (Figure 21e-f) and a significant increase in TPR (Figure 21b) clearly indicate the functional transition of the compensated RV to the early decompensated phase. Based on these two criteria, we can distinguish the early decompensated RV samples from the compensated ones, reflecting the functional transition. However, transcriptomic analysis revealed that the RV molecular profile is more consistent with the compensated group than the decompensated group, which is not only consistent with the similar RVSP and RV hypertrophy of the early decompensated RV, but more importantly, RVEDP maintains the same levels as in the compensated RV group, demonstrating that the increase in RVEDP specifically characterizes the late phase of decompensation (Figure 21d). Overall, the assessment of RV transcriptomic profiles in combination with hemodynamic features confirmed the existence of a transitional phase (early decompensated RV) between the compensated and late decompensated stages in the pathogenesis of MCT-induced PH with unfavorable RV remodeling.

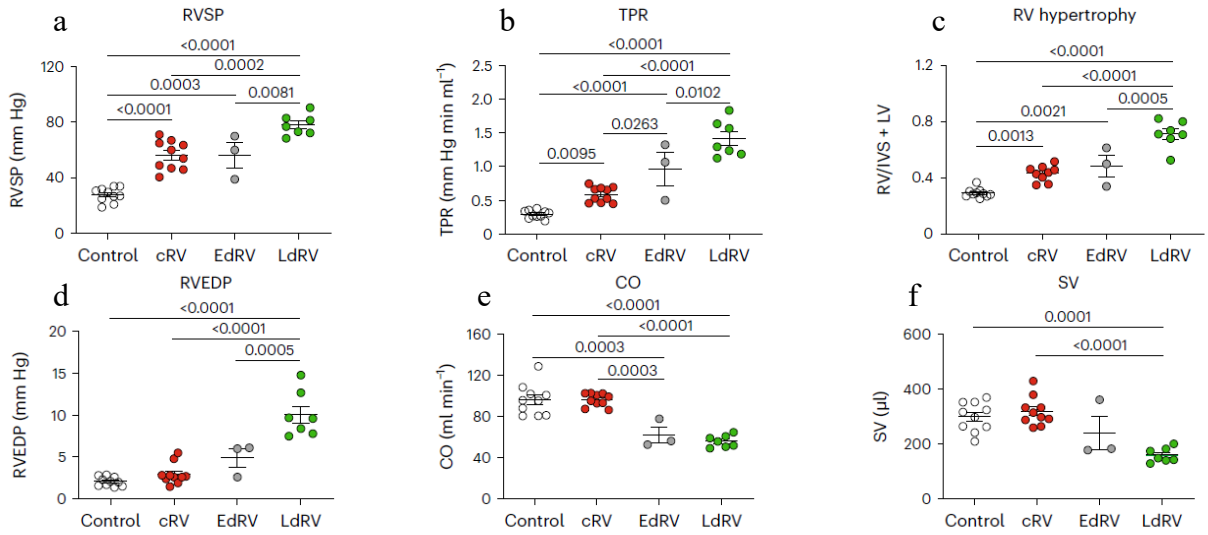

Figure 21; Hemodynamic assessment of MCT-induced PH in rats validates the early decompensated RV states. (a) changes in RV systolic pressure (RVSP), (b) total pulmonary resistance (TPR), (c) RV hypertrophy (right ventricular weight to left ventricular plus septal weight ratio), (d) RV end-diastolic pressure (RVEDP), (e) cardiac output (CO), and (f) and stroke volume (SV). n(control) = 10, n(compensated) = 10, n(early-decompensated) = 3, n(late decompensated) = Data are presented as the mean ± SEM. P values were calculated by one-way ANOVA followed by Tukey's multiple-comparisons test.

4.6.2 Unsupervised clustering of human transcriptome identified subgroups of compensated and decompensated RVs

Continuing with the human RV transcriptome, we delved deeper into the molecular heterogeneity of human RV samples by using the same unsupervised k-means clustering approach, where we identified the presence of five clearly delineated clusters among the 40 RV samples and labeled them as clusters A to E. The PC analysis shows all samples together with their assigned clusters by PC1 and PC2, based on their overall gene expression profile (Figure 22a). The distribution of clusters by the first two PCs shows the heterogeneity between the compensated and decompensated RV groups, in contrast to the normal RV samples, which all belong to the same clusters due to the greater similarity of their gene expression patterns. Cluster A contained all normal RV samples, eight compensated and three decompensated RV samples. In fact, many of the compensated samples, which had a similar gene expression profile to normal RVs, were categorized in this cluster. This could be related to their primary functional similarity reflected at the molecular level. Cluster E contains only four samples from the decompensated group, while clusters B, D and C each contain a different combination of primary compensated and decompensated RV samples (Figure 22a).

To further investigate the identified subgroups and their divergence, we then conducted a DEG analysis for each cluster in comparison to the normal RV group. The number of DEGs in each pair has been shown in Figure 22b. As expected, comparison of cluster A versus normal RV group resulted in the lowest number of DEG (Figure 22b). To confirm the identity of the k-means clusters with respect to compensated or decompensated RV states, we performed an additional analysis of DEGs within RV subgroups (groups 1 to 6), in which we included only compensated or decompensated RV samples from the same cluster. The results of this DEG analysis (Figure 22c) were very similar to the DEGs from the clusters (Figure 22b) and showed a similar identity of clusters B, C, D and E with groups 2, 3, 5 and 6, respectively. Therefore, we classified each cluster as either a subset of compensated (B and C) or decompensated RVs (D and E), determined by the predominant sample composition within each cluster. These results show that molecular distinctions between different RV subgroups can differentiate between compensated and decompensated RV samples, which goes beyond the primary classification based on hemodynamic analysis.

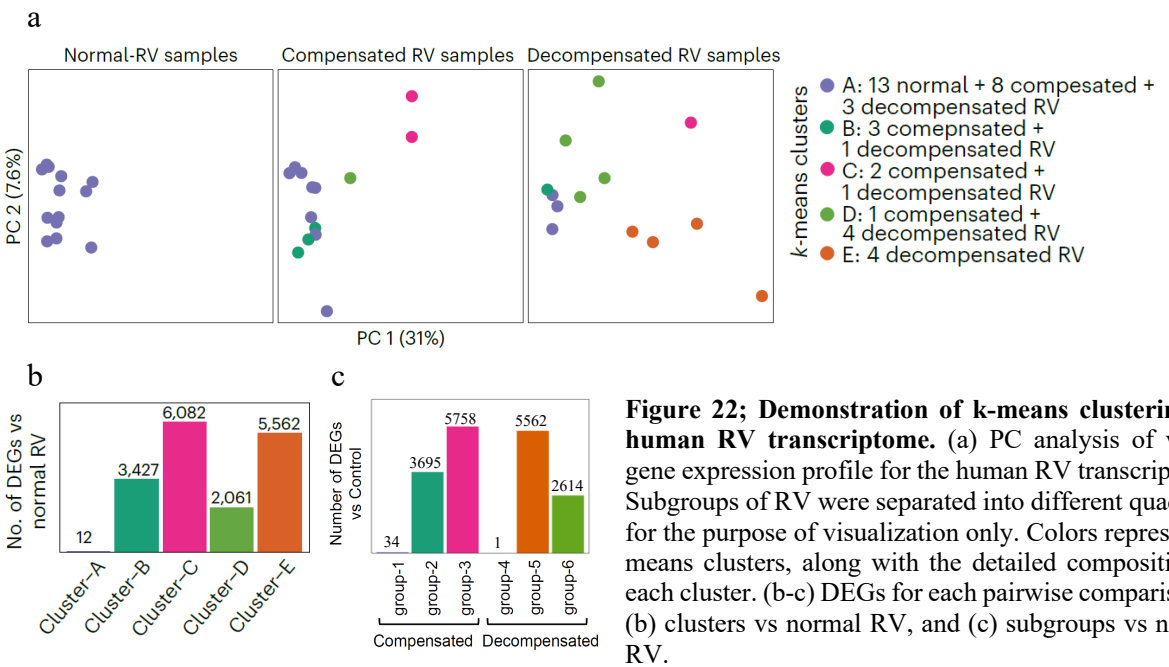

Figure 22; Demonstration of k-means clustering on human RV transcriptome. (a) PC analysis of whole gene expression profile for the human RV transcriptome. Subgroups of RV were separated into different quadrates for the purpose of visualization only. Colors represent k-means clusters, along with the detailed composition of each cluster. (b-c) DEGs for each pairwise comparison of (b) clusters vs normal RV, and (c) subgroups vs normal RV.

4.6.3 k-mean derived subgroups of human compensated and decompensated RV demonstrate distinct pathways regulation

Moving forward with the DEG sets, we performed enrichment analysis for all specific gene sets identified for pairwise comparison of each subgroups with the normal RV, as well as a one-to-one comparison of the different clusters. Overall, the initial enrichment results showed a significant upregulation of mitochondrial oxidative phosphorylation in cluster B (subgroups compensated RV), while mitochondrial respiration was downregulated in clusters D and E (subgroups of decompensated RV), confirming that the transition from compensated to decompensated RV is accompanied by an anaerobic metabolic shift. The downregulation of mitochondrial respiration in cluster D was accompanied by an increased regulation of HIF1A factor (Figure 23). Moreover, we found a significant similarity in the expression profiles of clusters C and E, mainly related to inflammatory responses by cytokines and especially NF-κB activation, as well as the same extent of downregulation of mitochondrial oxidative phosphorylation (Figure 23). These results indicate that in both clusters the inflammatory phenotype is strongly activated, possibly leading to an end-stage of RV failure. A look at the patient background data for the samples belonging to cluster C confirmed a severe hypertrophic RV profile in two out of three samples, which is also consistent with the fibrotic gene expression pattern of this cluster. This suggests that mismatch might develop in this subgroup by a different pathway than in cluster E (decompensated subgroup). Furthermore, based on one-to-one differential gene expression (1261 genes) and enrichment analysis, we found

several significant differences between these two subgroups, primarily related to Notch signaling pathways and the citric acid cycle (TCA cycle). (Figure 24a).

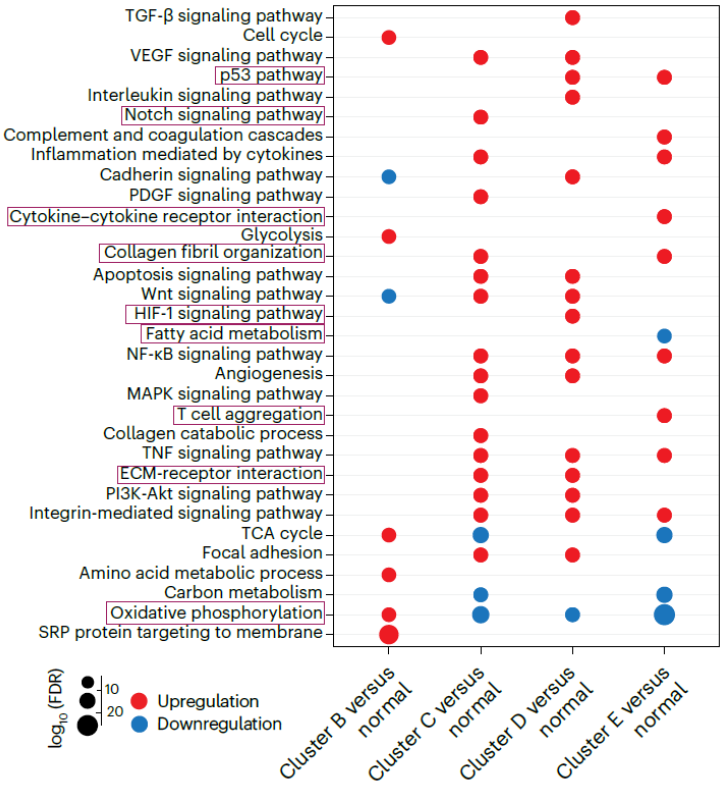

Figure 23; Cumulative gene set enrichment analysis for the shortlisted important pathways differentially regulated in each cluster vs. control. Red =upregulation, and blue=downregulation. Distinguishing terms are highlighted. One-sided Fisher's exact test was used for the enrichment analysis, and Benjamini–Hochberg method to adjust the P-value.

Next, we were interested in the main differences between two decompensated subgroups (cluster D, and E), in which we identified 1038 DEGs (corrected P-value ≤0.05; log2FC≥1 and ≤−1). The enrichment analysis showed that ECM receptor reorganization, cell adhesion molecules, and HIF1A regulation were among the most upregulated metabolic pathways in cluster D of decompensated individuals, while EMT, recruitment of multiple immune cells, and activation of various cytokines were significantly upregulated in cluster E of decompensated individuals. In addition, higher cardiomyocyte activity was observed in cluster D, demonstrating the markedly impaired cardiomyocyte function in cluster E (Figure 24b). In addition, we observed a strong increase in fatty acid metabolism, especially fatty acid transport in cluster D. However, comparison with the enrichment results of cluster E compared to normal RV indicates a probable downregulation of FAO and transport in this metabolic pathway in cluster E (Figure 24b).

Comparison of these differential expression results between clusters D and E with early and late decompensated RV changes in MCT-induced rats suggests differential regulation in two decompensated RV subgroups of the human transcriptome. Despite the strong metabolic shift from oxidative to non-oxidative respiration observed in both groups, one of the decompensated subgroups (cluster D) shows upregulation of ECM components and cell adhesion as well as

HIF1A, which are similar to metabolic pathways mainly regulated in the late decompensated RV group of MCT rats. In contrast, cluster E relies more on downregulation of fatty acid metabolism, while on the other hand it has a strong inflammatory profile and therefore exhibits a unique and human-specific pattern of RV dysfunction. Therefore, we were cautious about labeling human decompensated subgroups D and E as early or late decompensated and instead proceeded with two different subgroups of decompensated to perform a more comprehensive downstream analysis in humans.

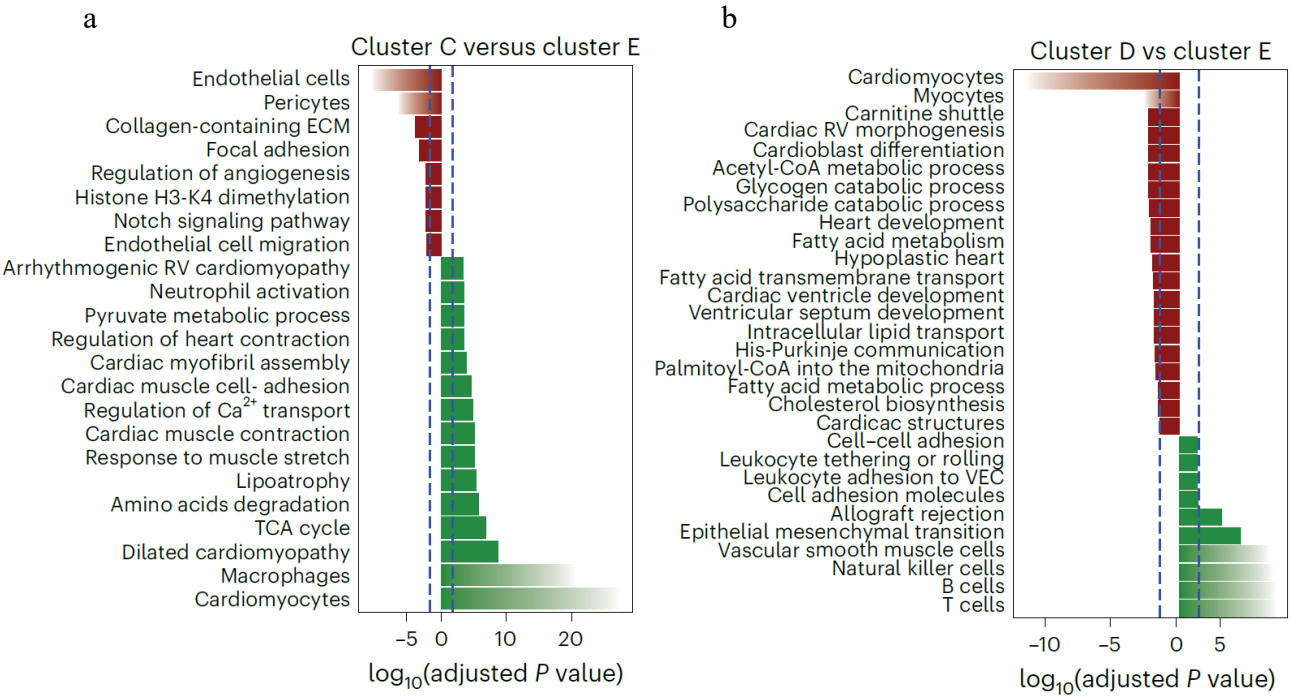

Figure 24; Differential enrichment analysis of clusters C, and D with cluster E (late-stage decompensated RV). Selected GO terms and KEGG pathways of cluster E (green) versus (a) cluster C and (b) cluster D. Dashed line represents FDR=0.05.

Based on patient characteristics (Table 2), there was another level of divergence within the decompensated RV samples. Of the 13 decompensated RV samples, 8 were from PAH patients, while the other 5 samples were failed RV caused by either ischemic or non-ischemic dilated cardiomyopathy (DCM). We performed an additional DEG analysis between these two subgroups and found 534 differentially regulated genes between the PAH-associated decompensated RV and the DCM-associated decompensated RV (corrected P value ≤ 0.05; log2FC≥ 1 and ≤ -1), followed by enrichment analysis. The main differentially regulated signaling pathways between these two groups are shown in Figure 25. This comparative enrichment analysis suggests that in patients with PAH-associated RV insufficiency, the upregulation of inflammation and EMT together with the differential regulation of ECM via collagens are the predominant distinguishing factors associated with the structural and physiological transition of the RV from a compensated to a decompensated state in PAH.

Moreover, the above changes were very similar to those observed for cluster E, suggesting that the strong activation of the immune response and the unique ECM remodeling pattern of RV failure are associated with the late stage of PAH (Figure 25). On the other hand, interferon-α-, β- and γ-mediated signaling pathways along with activation of vascular endothelial cells and pattern recognition receptors were strongly upregulated in the DCM-associated decompensated RV, suggesting a different pathway to RV failure.

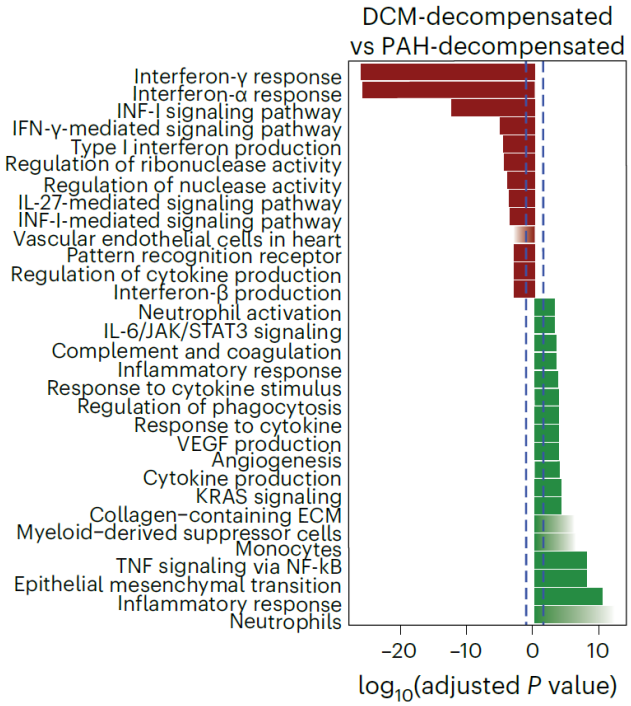

Figure 25: Differential enrichment analysis of two decompensated subgroups. Selected GO terms and KEGG pathways of DCM-associated (red) versus (a) PAH-associated (green) decompensated RV.

Overall, the classification of human RV samples into subgroups led to the identification of different upstream signaling pathways and transcriptional changes in the transition between compensated and decompensated states and described a broader spectrum of molecular heterogeneity in RV remodeling in humans. Figure 26 shows the normalized expression of 659 selected genes corresponding to the total significantly regulated pathways in different RV subgroups.

From the results of the subgroup analysis in both MCT-induced PAH and RV samples of patients, we identified an early decompensated phase that resembles the active remodeling from compensated to decompensated RV state. This intermittent phase, particularly in MCT-induced rats, exhibits a unique pattern of gene expression that is also partially found in one of the decompensated subsets in human RVs. While we have detailed the specific gene expression associated with each subset in both species, we were interested to see if there is a common pattern of gene expression between the two species for the transition from early to late decompensated RV.

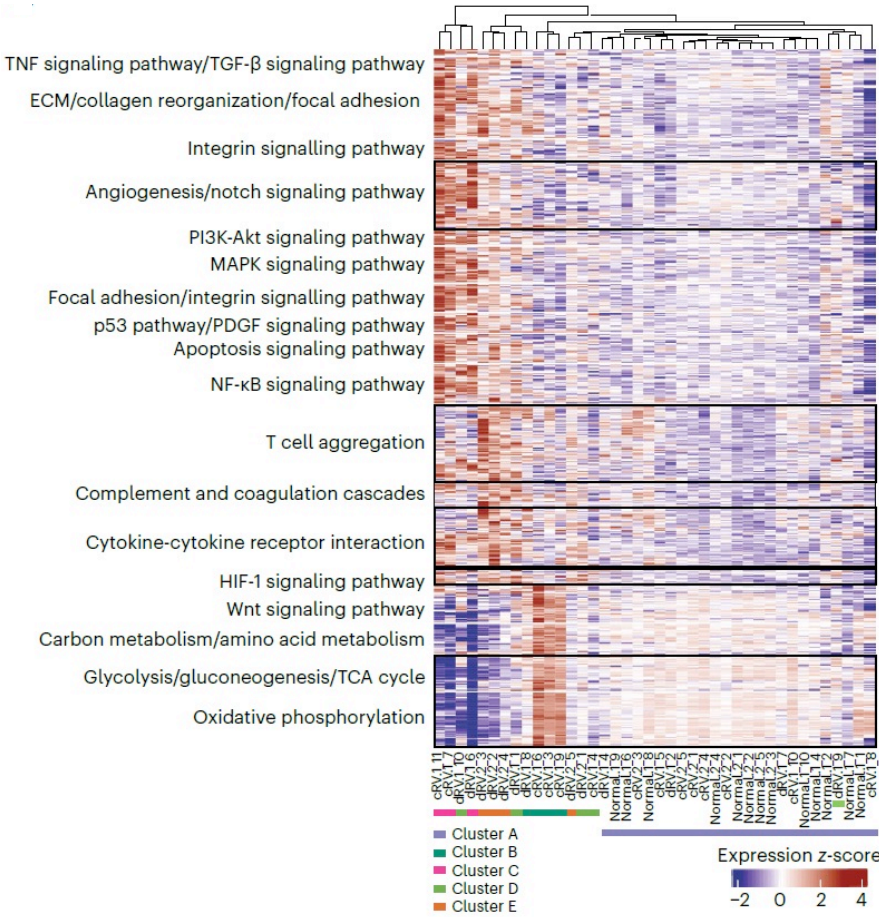

Figure 26; Relative gene expression pattern corresponding to the main differentially regulated pathways in human RV. Scaled gene expression (z-score) value of significant genes corresponding to the top selected pathways dysregulated between human RV subgroups of compensated and decompensated. Different groups of biological and molecular process with similar pattern of gene expression are grouped along the y axis.

4.7 Describing compensated to decompensated transition via comparative analysis of human RV remodeling and MCT-induced PH

4.7.1 Common dysregulated genes between human RV and MCT-induced rats

To this aim, we combined the 576 and 659 selected DE genes in MCT rats and humans, respectively (Figure 20b, 26), resulting in 85 common DEGs of PH-associated RV (Figure 27a-b, Table 3). Additional enrichment analysis of these 85 genes divided them into three main subgroups, mainly representing the following: ECM interactions and collagen reorganization, cell cycle regulation and hypoxia regulation. When looking at the pattern of change of these pathways in the three main subgroups of compensated and decompensated genes in the two datasets, we observed similar behavior in both species with respect to cell cycle and hypoxia regulation. However, the changes in the reorganization of ECM components were slightly different between MCT rats and human RV. It appears that in MCT-induced PH, the upregulation of collagens and other ECM components occurs earlier in the compensated phase and the RV is therefore more prone to develop a maladaptive RV due to fibrosis, whereas the major changes in ECM interactions in the human RV occur only in the decompensated phase. (Figure 27c-d)

Genes	Pathways
Col11a1, Col1a1, Col3a1, Col5a1, Fmod, Foxc2, Lox, Loxl2, Scx, Sfrp2, Grem1, Col4a1, Col4a2, Col4a6, Col6a2, Col6a6, Fn1, Itga10, Itga2b, Itga5, Itgb6, Itgb8, Lama5, Lamc1, Reln, Sdc4, Hmmr, Spp1, Tnc, Tnn, Thbs3, Vtn, Vwf, Cd36, Timp1, Mmp9	ECM-receptor interaction Collagen fibril organization
Slc2a1, Serpine, Pfkfb3, Pfkl, Pik3cg, Hk2, Hmox1, Eno3, Cybb, Angpt1, Camk2a	Hypoxia response
Birc5, Ccna2, Ccnb1, Cdc25c, Cdc7, Cdkn1a, Cdkn2b, Chek2, Clspn, Foxm1, Gpr132, Pkmyt1, Plcb1, Tpx2, Cdc25b	Cell cycle regulation
Fgfr4, Agt, Ripk3, Tgfb1, Il6, Pik3r5, Hspa2, Il1b, Fgf9, Il18, Myc, Wnt5a, Edn1, Bcl2l1, Gadd45b, Csf2rb, Ccl2, Hspa1a, Map2k6, Nr4a1, F2rl1, Foxc1, Nppa	NF-κB activity, T-cell aggregation, TNF signaling, MAPK activity, Apoptosis, Angiogenesis, Cardiac muscle contraction

Table 3: 85 common differentially regulated genes of PH-associated RVs from patients and MCT-rats.

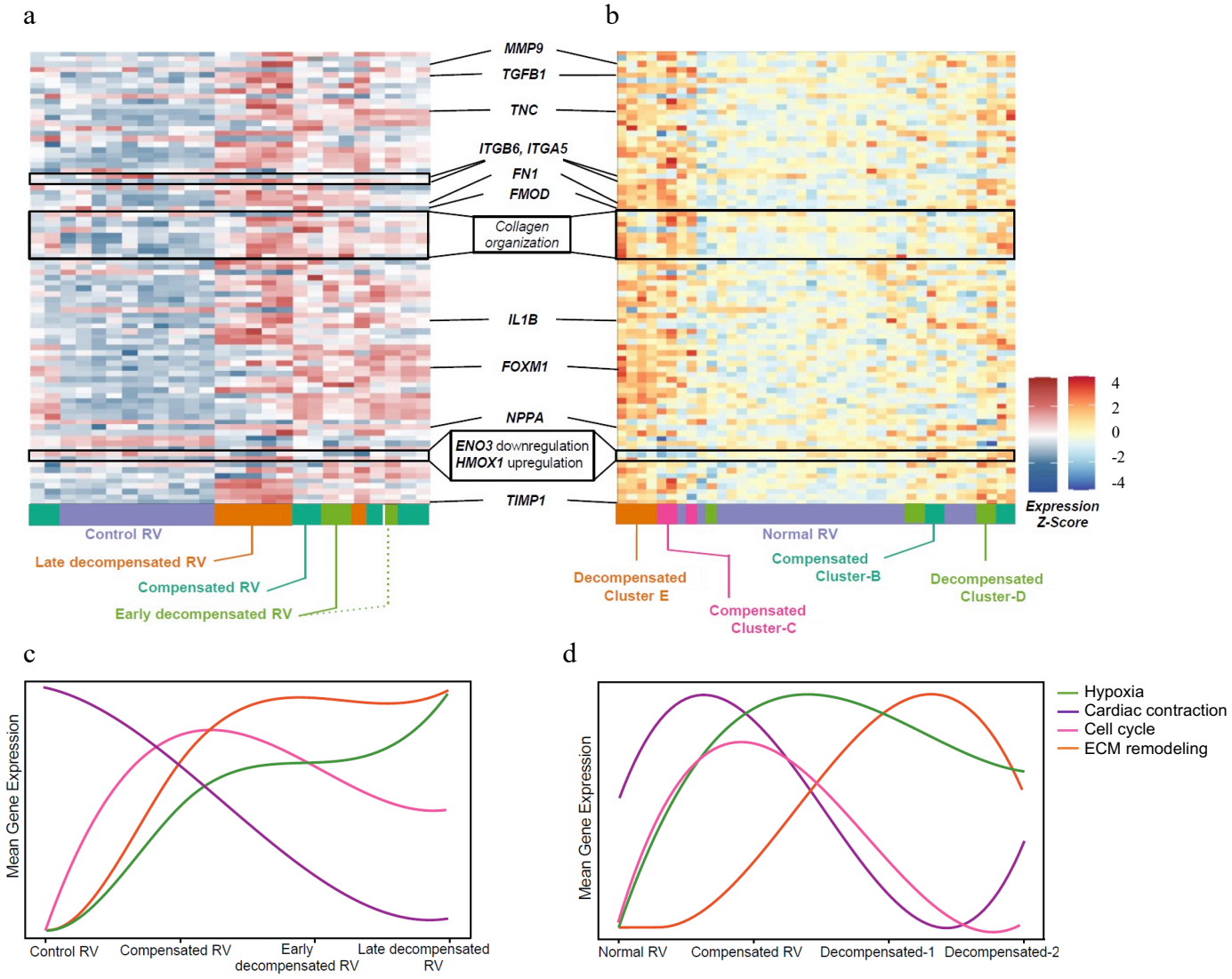

Figure 27; Summary of common dysregulated genes and associated pathways in (a,c) MCT-rat RVs, and (b,d) human RV samples and in. Colors of the heatmap samples shown on the bottom represent k-means clusters.

4.7.2 Changes in the extracellular matrix stand out as the main dysregulated pathway in both rodent models of PH and the RV remodeling of PAH patients.

In our initial integrative analysis, ECM remodeling was the most highly regulated metabolic pathway in all datasets (Figure 15b). It also emerged when we compared the transcriptome pattern of common dysregulated genes between human RV and MCT-induced RV subgroups (Figure 27), with 36 of 85 genes directly associated with an ECM role or regulation (Table 3). To determine whether the expression of ECM-associated genes can distinguish between the compensated and decompensated phases of RV, we selected several key regulators of ECM for further evaluation by two different approaches.

First, we considered only the common transcriptome signature and shortlisted four ECM candidates: *COL1A1* as one of the most dysregulated collagens, two structural glycoproteins of cardiac ECM, fibronectin (*FN1*) and integrin beta-6 (*ITGB6*), and a non-structural ECM-related protein, tenascin-C (*TNC*). These four, in addition to *NPPA*, the known marker for PAH-associated hypertrophy, were selected for further PCR validation and correlation analysis. Among these, *NPPA* and *FN1* were upregulated in both compensated and decompensated RVs of both species and correlated significantly with RVEDP (Figure 28a-f). On the other hand, *Tnc* and *Col1a1* were only upregulated in the compensated phase of RVs from MCT rats, and therefore their correlation with RVEDP was not significant (Figure 28g-l). In contrast, *Itgb6* was significantly downregulated in decompensated RV of MCT rats, while it was slightly correlated with RVEDP (P-value=0.09) (Figure 28m-o).

In addition, we detected increased expression of two key regulators of ECM, matrix metallopeptidase-9 (*MMP9*) and *TIMP1* (Tissue Inhibitors of MMPs), in both compensated and decompensated RVs of both species, with *MMP9* also significantly correlated with RVEDP in MCT rats (Figure 28p-u).

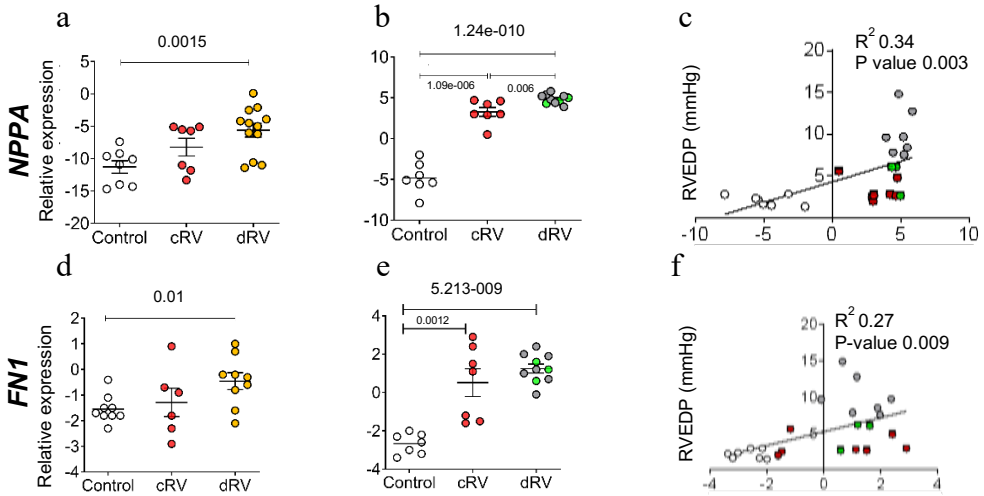

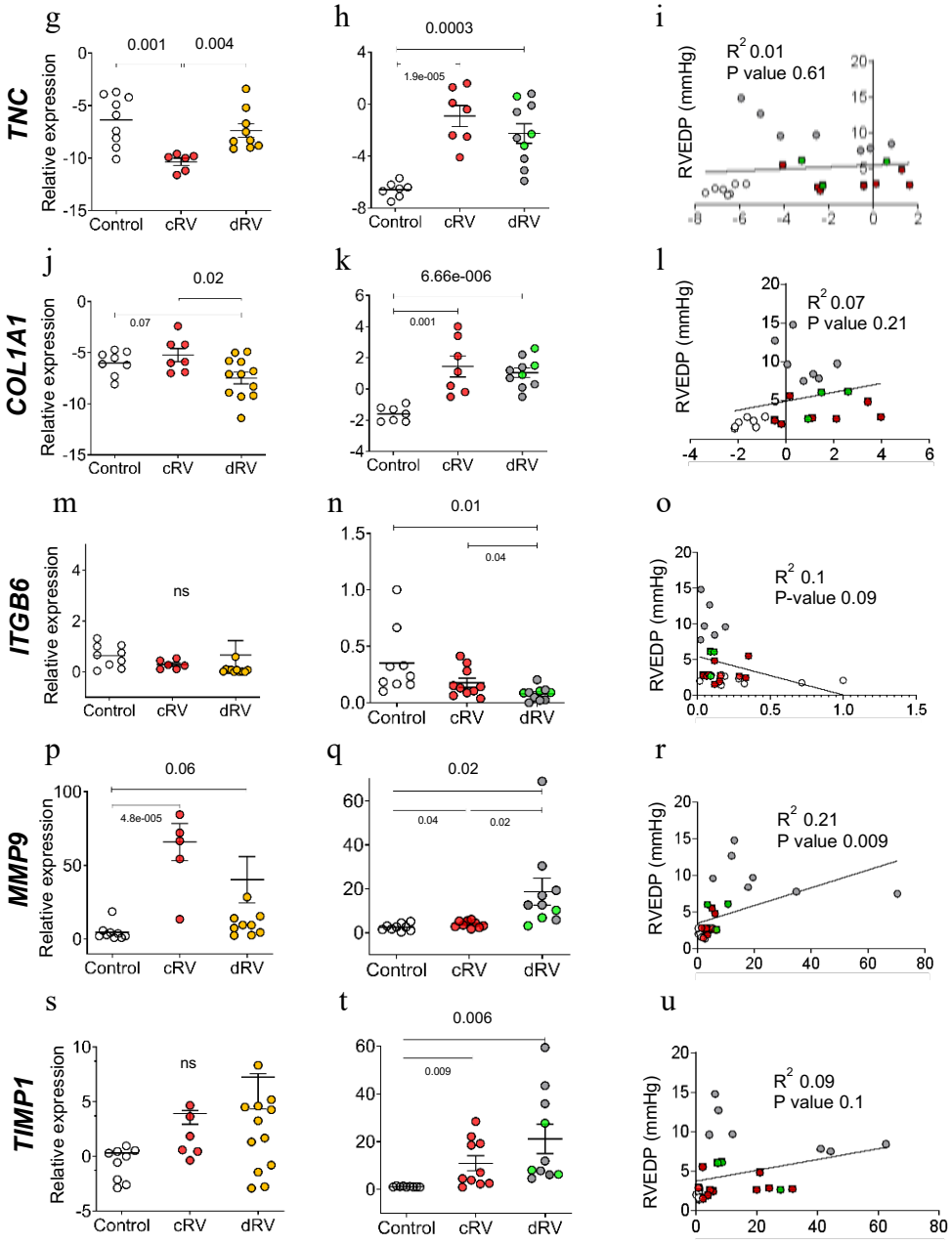

Figure 28: Selected differentially regulated genes associated with ECM in human RV and MCT-rat RV samples. The relative expression values of five selected genes: *NPPA, FN1, TNC, COL1A1*, *ITGB6, MMP9, and TIMP1* analyzed by qPCR. (a, d, g, j, m, p, s) from human control, compensated, and decompensated RVs, and (b, e, h, k, n, q, t) from compensated, and decompensated RVs isolated from rat MCT-induced PH and respective controls. (c, f, i, l, o, r, u) Correlation between expression levels of the respective genes and right ventricular end-diastolic pressure (RVEDP). Data are presented as mean ± SEM.

In another approach, in addition to these generally dysregulated ECM-related genes, we focused on the regulation of certain ECM candidates identified as specific for different subgroups of compensated and decompensated RV samples.

Comparing PAH- and DCM-associated decompensated RVs, we found that eight ECM regulators were specifically upregulated in human PAH-induced decompensated RVs, including *THBS1, NPPA, ITGA5, TNC, ITGB6, FN1, COL1A1*, and *ITGA10*. In addition, 16

other ECM-related genes (*COL2A1, COL6A5, COL9A1, COMP, DAG1, GP6, TNR, ITGA4, ITGB7, LAMA1, LAMA4, ITGB6, TNC, TNN, HMMR* and *SPP1*) were specifically dysregulated in cluster E compared to cluster D, while there were only a few ECM-associated genes that were exclusively regulated in cluster C (severe hypertrophic samples), including *COL4A3, COL9A3, HSPG2, TNXB, ITGA5, LAMA5* and *COL6A2*. To shortlist these three ECM-related gene sets, we selected those that appeared in both the common list of dysregulated genes (85) and at least one of the three subsets, and we selected 13 final target genes (including *NPPA*) for further validation.

In order to confirm whether those 13 ECM-related transcripts are altered at the protein level, we assessed proteome datasets that were publicly accessible for human RV and the common animal models of PH, where we initially identified seven proteins with significant regulation across four RV proteomic datasets from different rat models of PH, along with the recently published human RV proteome of PAH patients[147,150–152,180] (Table 4), confirming the presence of newly discovered ECM molecules in our study along with those previously found. Four other proteins (ITGB6, HMMR, MMP9, and TIMP1) which had no proteomics record in those researched RV datasets, demonstrate robust plasma-level regulation in various PAH patients' cohorts (MMP9 and TIMP1)[163,181], or showing similar regulation pattern in rat models, such as SuHx at transcriptome level (*Itgb6*, and *Hmmr*)[146,148] (Table 4). We then performed western blotting, to confirm the regulation of the remaining two genes, which we newly discovered (ITGA10 and SPP1) without any public evidences at protein level. Interestingly, western blot results showed that both ITGA10 and SPP1, which were not detected in any of those public proteome or literature, were significantly upregulated at the protein level in decompensated RVs from MCT-PH rats (Figure 29). As a control for our western blot, we additionally assessed protein levels of NPPA, and ITGA5 in the same tissues, which determined upregulation of both in decompensated, and compensated RV, respectively. Together with the above-mentioned proteome evidences, we validated all 13 ECM candidates that were explicitly dysregulated in human RV remodeling associated with PAH, and possibly in the early phase of decompensation (cluster E).

ECM targets	rats RV Proteome[147, 150,151]	human RV Proteome[152]	Plasma Proteome[181 ,182]	rats RV transcriptome 146,148	current study WB* / transcriptome
FN1	Increase	Increase in dRV	Not detected	Increase	Increase+
COL1A1	Increase	Increase (NS)	Not detected	Increase	Increase+
TNC	Increase	Increase in dRV	Not detected	Increase	Increase+
LAMA5	Increase	Increase in both (NS)	Not detected	Increase	Increase+
COL6A2	Decrease (NS)	Increase in dRV	Not detected	Increase	Increase+ / Increase*(NS)
ITGB6	Not detected	Not detected	Not detected	Decrease	Decrease+
HMMR	Not detected	Not detected	Not detected	Increase	Increase+
MMP9	Not detected	Not detected	Increase	Not detected	Increase+
TIMP1	Not detected	Not detected	Increase	Increase	Increase+
NPPA	Increase	Not detected	Not detected	Increase	Increase in dRV*
ITGA5	Increase	Not detected	Not detected	Increase	Increase in dRV/cRV*
ITGA10	Not detected	Not detected	Not detected	Increase	Increase in dRV*
SPP1	Not detected	Not detected	Not detected	Increase	Increase in dRV*

Table 4: Protein validations of 13 selected ECM targets in MCT-RV and human RV. +RV transcriptome evidence, *Western Blot evidences in MCT-rats (cRV = compensated, dRV= decompensated), NS = not significant.

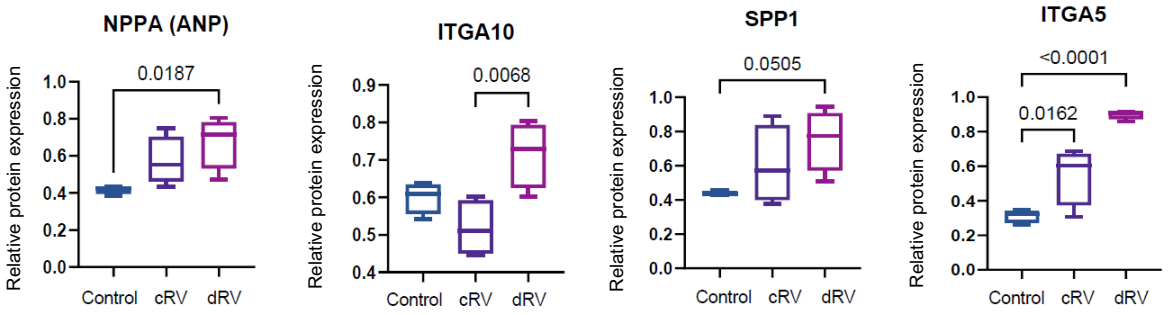

Figure 29: Western blot validations of 4 ECM proteins in MCT-RV. Western blot quantifications for ANP, ITGA10, SPP1, and ITGA5, and normalized to the corresponding loading control (Vinculin). Protein expression levels has been tested by one-way ANOVA followed by Dunnett's multiple comparisons test (exact P-value has been demonstrated when significant). Data are presented as mean ± SEM. n(control)=4, n(cRV)=4, n(dRV)=4.

4.8 Olink plasma proteome of an independent cohort of PAH patients

As mentioned above, the ECM was the most dysregulated signaling pathway in the RV transcriptome of human PAH patients and in both animal models with RV dysfunction (Figure 30a)

In Section 4.7, we have listed several important ECM-related markers for the compensated and decompensated phases that may serve as RV-specific candidates for diagnosis and treatment. However, we did not review their potential for prognosis and prediction of RV functional outcome. Therefore, as a next step, we decided to investigate the potential of dysregulated ECM proteins as circulating biomarkers for the diagnosis or prognosis of PAH-associated RV dysfunction. To this end, we used an independent PAH cohort in which an Olink® Cardiometabolic Panel was performed. This cohort was used as the discovery cohort (referred to as the German Cohort in the figures) and included a total of 35 PAH patients. Patients were primarily divided into two groups: 20 patients with compensated and 15 patients with decompensated (end-stage) RV. For this classification, we used RV-PA coupling, the ratio of

RV end-systolic elasticity (Ees) (as a measure of RV contractility) to arterial elasticity (Ea) (as a measure of afterload) of PAH patients, as previously described161. Patients with Ees/Ea > 0.8 were considered to have a compensated RV, whereas Ees/Ea < 0.8 was indicative of a decompensated RV.

In our study, we first identified the most significant DEGs (P < 0.05) across all pairs in our transcriptome, accounting for approximately 30% of the total transcripts (15,305 genes). We then selected the top 25% of differentially expressed proteins from the Olink biomarker panel, resulting in 23 proteins in the cohort. We then merged these candidates from the transcriptome and plasma proteome datasets to identify common genes/proteins. Surprisingly, we found that over 60% of the plasma-regulated proteins (15 out of 23) corresponded to dysregulated entities of the transcriptome. Of these, eight proteins were associated with ECM remodeling or cell adhesion (Figure 30b). We specifically selected these eight ECM proteins for further analysis and checked their differential abundance in plasma between compensated and decompensated groups in the proteome cohort, with five proteins (CRTAC1, NID1, SPARCL1, MEGF9 and C1QTNF1) selected for further confirmatory analysis (Figure 30c). The first four had a P-value = 0.05. The P-value of C1QTNF1 was 0.07, but was considered for further evaluation as it is frequently regulated in decompensated and compensated RV. NID1 and C1QTNF1 were elevated in the plasma of patients with decompensated compared to those with compensated RV, while the remaining three showed higher expression in the compensated RV compared to the decompensated state in PAH patients in the discovery cohort (Figure 31a-e).

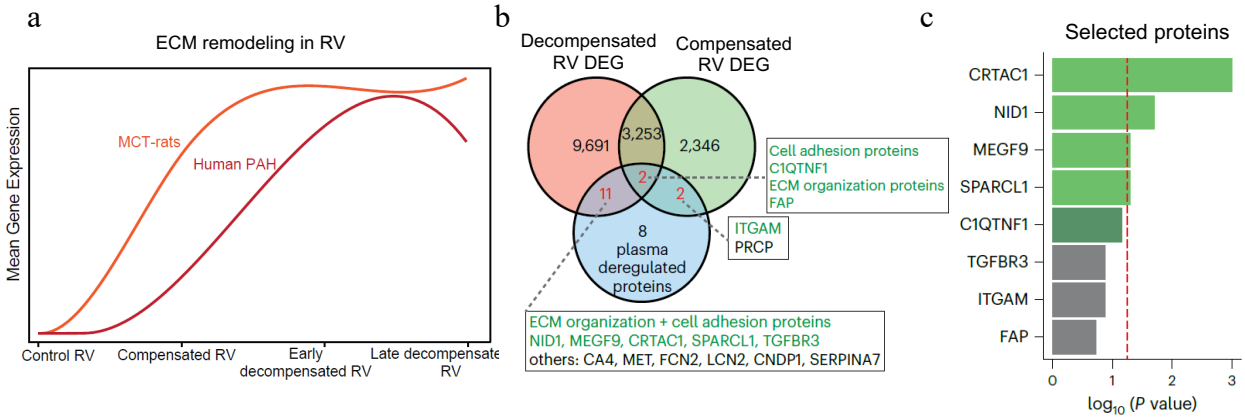

Figure 30: Regulation of extracellular matrix proteins in plasma. (a) Transcriptome regulation of ECM-associated genes in both human and MCT rat RV samples. (b) Inclusion of all dysregulated transcripts (base mean expression ≥ 5; −0.585 ≤ log2FC ≥ 0.585; FDR ≤ 0.05) in human RV, and top 25% of deregulated plasma proteins between participants with compensated and decompensated RV in German plasma cohort. Green shows the proteins associated with ECM or cell adhesion. (c) Eight common ECM proteins regulated in both transcriptomes and the PAH proteome, and their corresponding *P-value* (calculated by unpaired t-test comparison) between compensated and decompensated subgroups of participants in the discovery cohort. CRTAC1 = 0.001, NID1 = 0.02, MEGF9 = 0.05, SPARCL1 = 0.05, C1QTNF1 = 0.07, TGFBR3 = 0.13, ITGAM = 0.13, FAP = 0.19. Top five proteins selected to check for their biomarker capacity are highlighted in green on the bar plot, and the dashed line highlights *P-value* = 0.05.

To evaluate the changes observed in the plasma levels of these five proteins between compensated and decompensated RV, we first checked their transcriptome changes. Increased levels of *NID1* and *C1QTNF1* and decreased levels of *MEGF9* in RV tissue correlated with the changes in their plasma levels in the PAH detection cohort. However, the decreased expression of two other proteins in plasma, particularly *CRTAC1*, was inconsistent with the increased mRNA levels observed in the transcriptome of the decompensated RV (Figure 31f-j).

In addition, we performed qRT-PCR and western blot analysis for the panel of five candidate proteins in compensated and decompensated RV tissues of MCT-induced to validate the corresponding alterations in RV tissues. Firstly, we were able to detect the similar RNA regulation of all five proteins between compensated to decompensated RV in MCT-induced PH, with their human transcriptome counterparts (Figure 31k-o). Moreover, in the western blot results, despite lacking the significant *p-value* in three proteins due to the high variability of gel-based detection for high molecular weight proteins, the RV protein alteration levels remained consistent with their plasma alterations, rather than the transcriptome (Figure 31p-t). Overall, these results suggest that NID1 and C1QTNF1 exhibit absolute upregulation in both the compensated and decompensated RV states, which correlates with the increase in their plasma levels. Second, the downregulation of MEGF9 protein was consistent in both RV tissue and plasma in compensated and decompensated RV compared to control. However, we observed a similar downregulation in compensated RV only in human mRNA levels, whereas in MCT-induced RVs there was a primary upregulation of mRNA and then a significant decrease in the decompensated phase. This could be due to differences in transcription rates in humans and rats, but also to intrinsic differences between human RV hypertrophy and the MCT-induced hypertrophy state in rats. Nevertheless, its downregulation in the late stage of RV decompensation was consistent in all samples, demonstrating its potential as a circulating biomarker. Finally, as mentioned above, the observed pattern of downregulation of plasma levels of CRTAC1 and SPARCL1 was inconsistent with their increased RV mRNA levels (in both species), whereas the pattern of change in RV protein levels detected by Western blot was also consistent with their plasma alteration. These differences may also be attributed to post-transcriptional changes of these two proteins in the RV, possibly related to different PAH conditions.

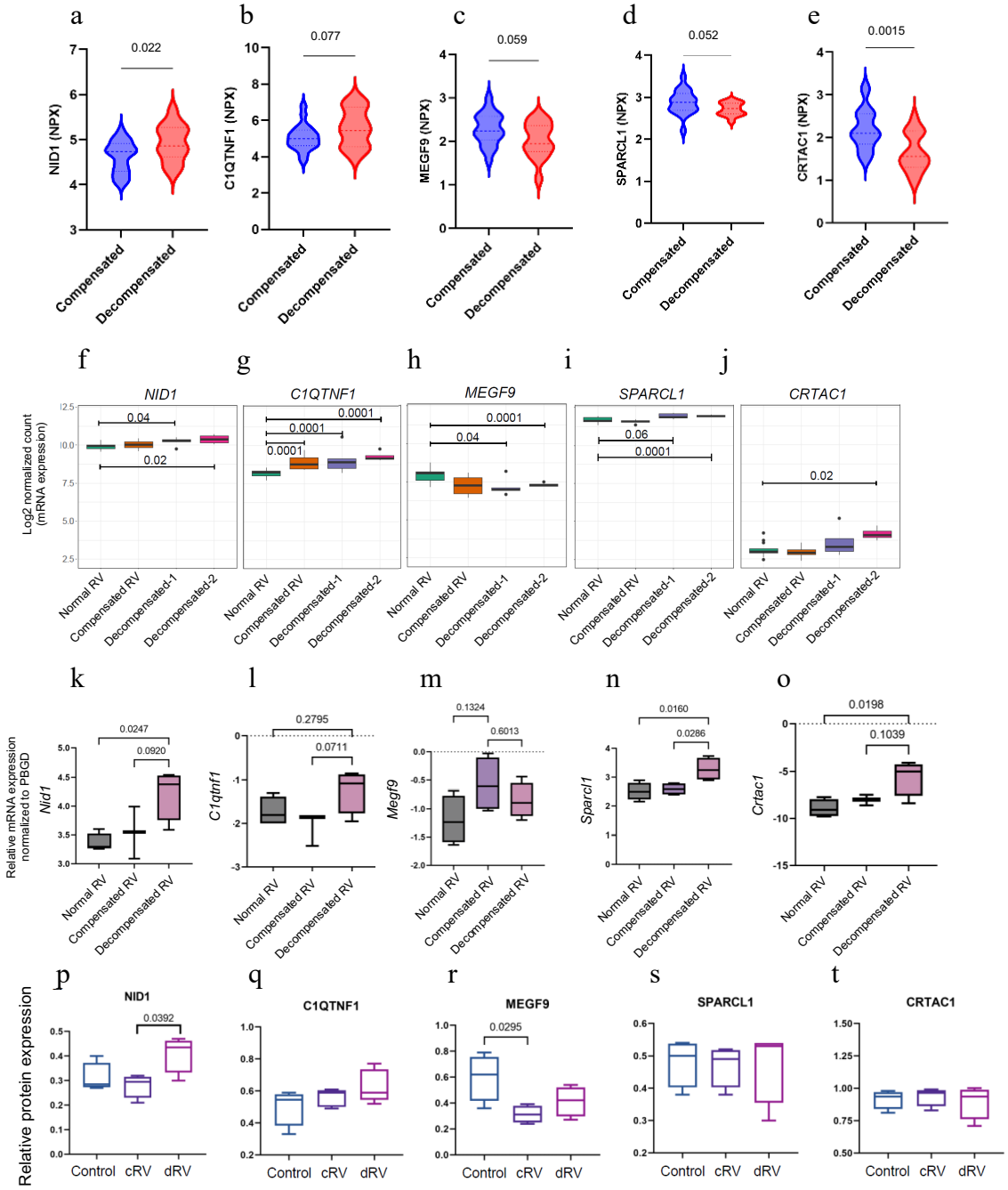

Figure 31: Plasma proteome, mRNA, and protein expression in RV samples of human PAH patients, as well as MCT-induced rats. (a-e) Olink protein expression levels (NPX), in two groups of PAH patients with compensated or decompensated. (f-j) Transcriptome level of five candidate genes in normal, compensated, and two decompensated subgroups of human RV. (k-o) Relative mRNA expression measured by qPCR for five selected proteins in control, compensated and decompensated RVs from MCT-induced rats. (p-t) Western blot quantifications for five selected proteins, normalized to the corresponding loading control of each blot (Vinculin). Both mRNA and protein expression levels has been tested by one-way ANOVA followed by Tukey's multiple comparisons test. Exact P-value has been demonstrated where significant. Data are presented as mean ± SEM. n(control)=4, n(cRV)=4, n(dRV)=4.

4.9 Panel of five ECM proteins act as potential biomarker for PAH

4.9.1 Correlations between plasma proteins and RV functional parameters

To evaluate the biomarker potential of these five deregulated proteins in PAH, we first examined the correlations between these proteins (NPX) and mPAP, PVR, CI and NT-proBNP plasma levels in the same patients. We found that the increased protein levels of NID1 and C1QTNF1 correlated significantly with increased mPAP and proBNP. In addition, NID1 showed a positive correlation with PVR and a negative correlation with CI (Figure 32a-b). Conversely, reduced MEGF9 levels correlated strongly with PVR, CI and proBNP levels (Figure 32c). However, we did not detect a significant correlation between CRTAC1 and SPARCL1 protein levels and RV functional factors when corrected for age distribution, which could be due to their inconsistent expression changes, but also their age-dependent expression. Taken together, these results suggest that the regulation of three ECM proteins (NID1, C1QTNF1 and MEGF9) is highly associated with RV function, making them potential prognostic markers for PAH.

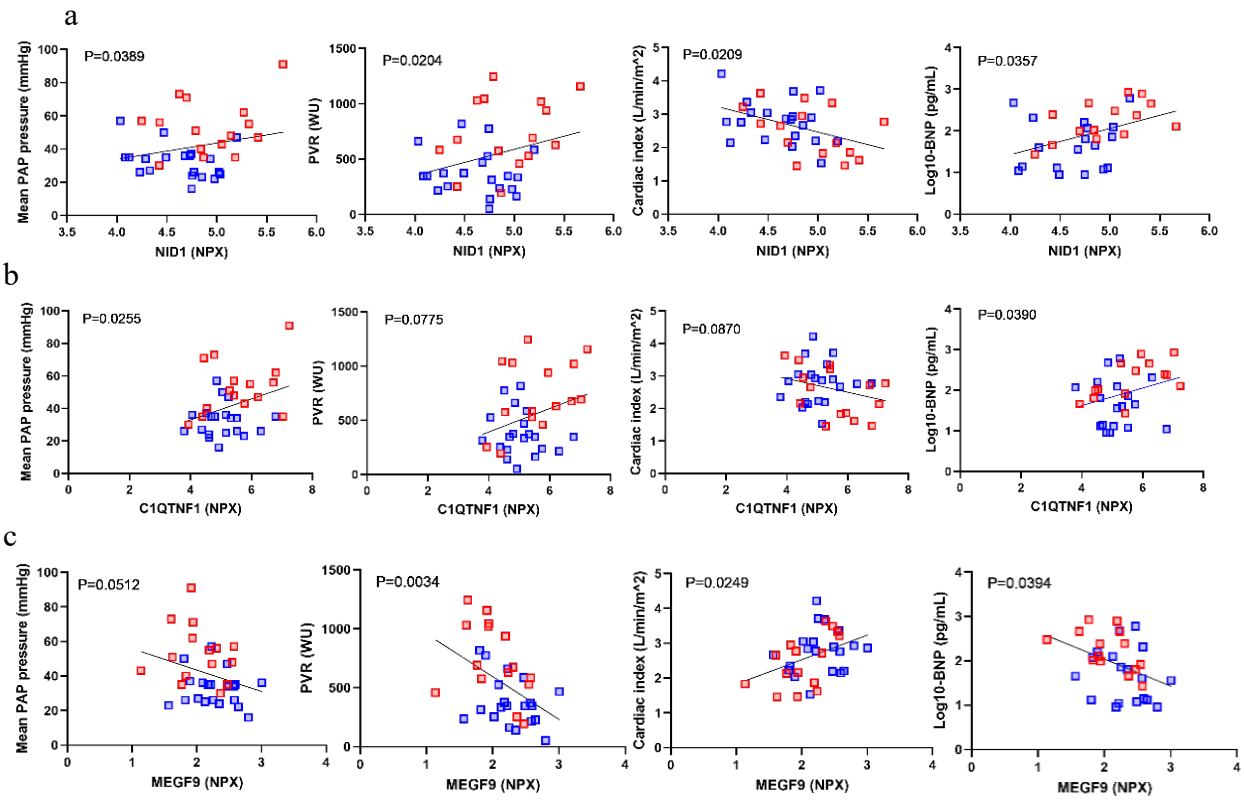

Figure 32: Simple linear regression for protein expressions with four main ~RV functional parameters in PAH patients with compensated (blue) and decompensated (red) RV, (a) NID1, (b) C1QTNF1, and (c) MEGF9. Linear regression model test adjusted for age/sex. (mPAP = mean pulmonary arterial pressure, PVR= pulmonary vascular resistance, CI = Cardiac Index).

4.9.2 Using an independent validation cohort to assess the expression and functional correlations of five potential biomarkers

To validate the functional results offering the biomarker potential of our proposed five proteins, we used a second independent plasma proteome cohort of PAH (indicated as UK cohort), containing 117 participants, including 61 PAH patients and 56 donors with normal RV function, and the plasma protein expressions were similarly quantified by an Olink® cardiometabolic protein panel, targeting higher range of target proteins[159].

Of the 61 PAH cases, 26 were primarily classified as compensated RV and the other 35 as decompensated RV, based on the cardiac index, similar to the RV transcriptome (Methods). Notably, we confirmed a significant increase in the expression of NID1 and C1QTNF1 and decreased expression of CRTAC1 and MEGF9 in patients with decompensated RV compared to patients with compensated RV, similar to what we observed in the discovery cohort. However, SPARCL1 showed no significant change between the different patient groups in the validation cohort (Figure 33).

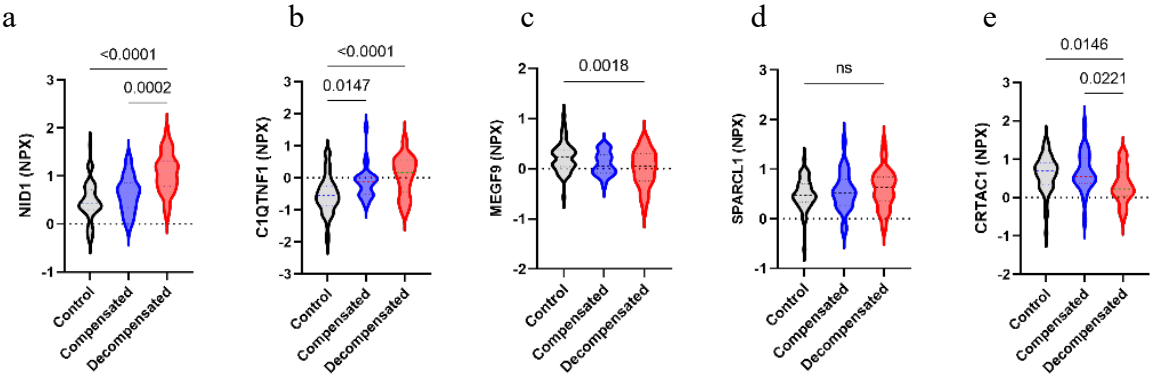

Figure 33: Plasma protein expression in RV samples of human PAH patients from validation cohort (UK). (a-e) Olink expression levels (NPX), in three groups of participants, with Normal RV, and PAH patients with compensated or decompensated RV. ns = non-significant.

Similar to the discovery cohort, NID1 showed a negative correlation with functional RV factors such as CI, but a positive correlation with mPAP, PVR and proBNP levels (Figure 34a), whereas this pattern was reversed for the downregulated proteins (CRTAC1 and MEGF9) (Figure 34b-c). The expression of C1QTNF1 showed a positive correlation only with proBNP levels in our validation cohort, similar to SPARCL1 (Figure 34d-e).

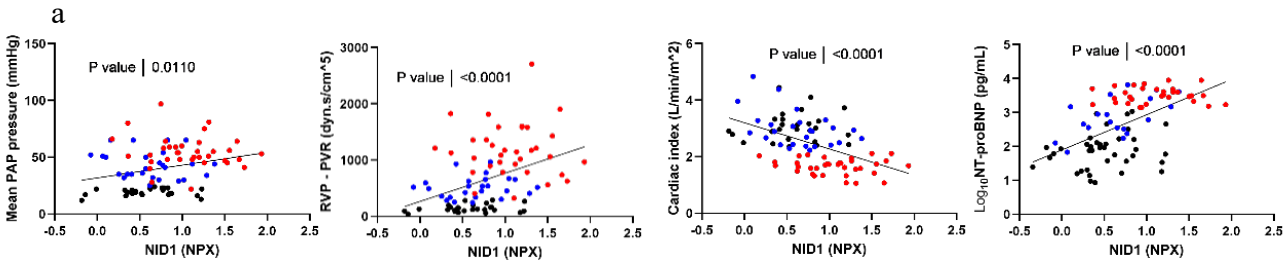

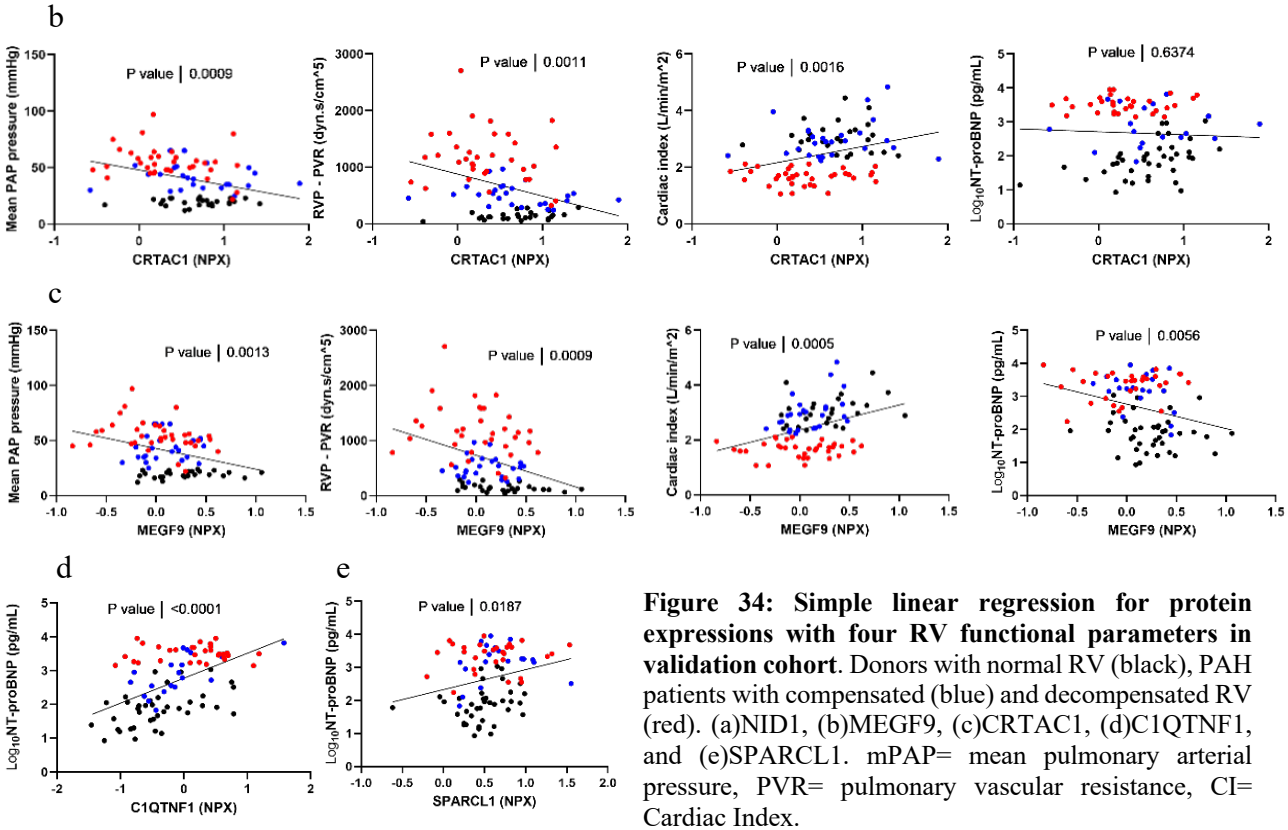

Figure 34: Simple linear regression for protein expressions with four RV functional parameters in validation cohort. Donors with normal RV (black), PAH patients with compensated (blue) and decompensated RV (red). (a)NID1, (b)MEGF9, (c)CRTAC1, (d)C1QTNF1, and (e)SPARCL1. mPAP= mean pulmonary arterial pressure, PVR= pulmonary vascular resistance, CI= Cardiac Index.

4.9.3 Plasma profile of five ECM proteins effectively distinguishes between compensated and decompensated RV conditions

Following the assessment of functional correlation, we additionally investigated how well these five proteins can predict or classify two different states of RV hypertrophy and dilation that resemble the severity of PAH. To this end, we used a random forest (RF) model (Methods) for the five proteins and their different combinations and then analyzed the receiver operating characteristic (ROC) curve to evaluate the performance of our RF model. We demonstrated that the panel of five proteins could effectively discriminate between PAH patients with compensated or decompensated RV in the discovery cohort and achieved an ROC-AUC of 0.83 (P-value=0.001) with an accuracy of 81%. (Figure 35a). Similarly, using the same RF approach in the validation cohort, we confirmed that these five proteins could significantly discriminate patients with compensated or decompensated RV (AUC−ROC = 0.78, P-value = 0.0004 and accuracy = 80%) (Figure 35b).

In addition, the decision tree model allows the calculation of a feature weight score for each protein (method). Based on this score, CRTAC1 and NID1 showed strong predictive power in the discovery cohort, while in the validation cohort NID1 and C1QTNF1 and (to a lesser extent) CRTAC1 showed the strongest predictive power in discriminating between PAH patients with

compensated and decompensated state of the RV (Figure 35c). The results of both cohorts suggest that NID1 has the greatest predictive potential as a prognostic biomarker.

Moreover, the combination of NID1 with C1QTNF1 and CRTAC1 gave the best overall performance in discriminating between two groups of PAH patients with different RV function (AUC=0.88 in the discovery cohort and AUC=0.77 in the validation cohort) (Figure 35d-e). In addition, the combination of NID1 with C1QTNF1 and MEGF9 in the validation cohort also yields an AUC=78, accuracy=80% for the similar prediction (Figure 35g), while the combination of NID1, CRTAC1 and SPARCL1 in the discovery cohort also showed high performance (AUC=82, accuracy=83%) (Figure 35f).

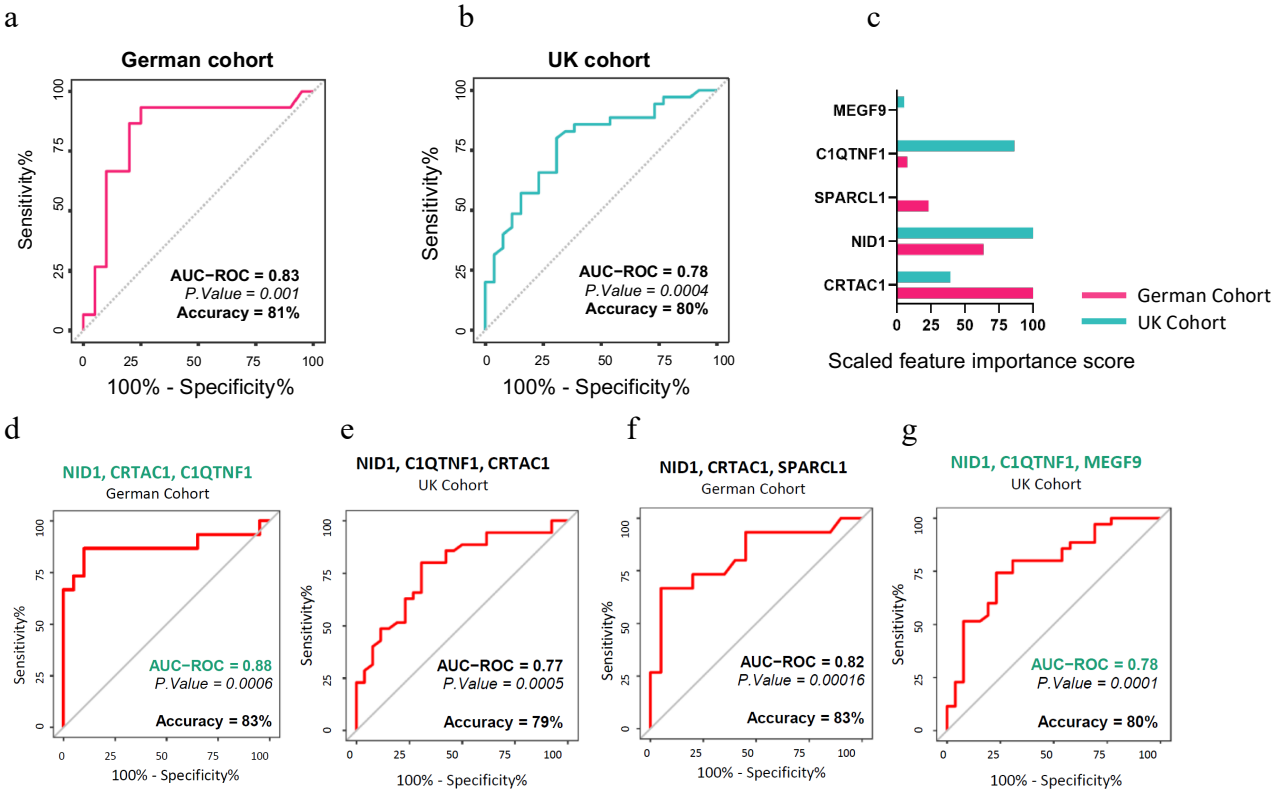

Figure 35: ROC analysis showing the performance of random forest model for different combination of five proteins in classifying two groups of patients with decompensated vs. compensated RV. (a) Discovery cohort (German), and (b) Validation cohort (UK) corresponding AUC (area under the curve) results, along with accuracy and the ROC P-value (using one-sided Mann-Whitney (Wilcoxon-based) test for the H0: AUC=0.5). (c) Feature (proteins) importance score measurement in each cohort, which shows the relative influence of each protein in classifying performance. (d-g) ROC analysis showing the performance of random forest model for (d) NID1+CRTAC1+C1QTNF1 in discovery cohort, (e) in validation cohort. (f) NID1+CRTAC1+SPARCL1 in discovery cohort, and (g) NID1+C1QTNF1+MEGF9 in validation cohort classifying two groups of patients with decompensated vs. compensated RV. Corresponding AUC (area under the curve), along with accuracy and the ROC P-value are demonstrated on the plots. The most powerful combination for each prediction highlighted in green.

4.9.4 Plasma profile of five ECM proteins predicts the survival outcomes of PAH patients.

In order to assess the predictive potential of the panel five ECM proteins in prediction of PAH outcome, we utilized the follow-up information from patients accessible within the validation cohort. Out of the 61 PAH patients in this cohort, 31 either deceased or underwent lung

transplantation, whereas the remaining 30 survived throughout a median follow-up period of 4.5 years[159].

Interestingly, the ROC analysis of survival showed that the panel of five proteins could significantly discriminate PAH patients with poorer survival outcome with AUC=0.76 (Figure 36a). Among the five proteins, NID1 and SPARCL1 served as two independent predictors of patient survival (AUC=0.73 for both) (Figure 36b-c), and when NID1 was combined with either SPARCL1 or MEGF9, the accuracy of survival prediction increased to AUC=0.76 and 0.74, respectively (Figure 36d-e). This was consistent with the effect of SPARCL1 and MEGF9 in increasing the predictive power of the RF model while adding them to the main predictive factors in the discovery and validation cohorts, respectively.

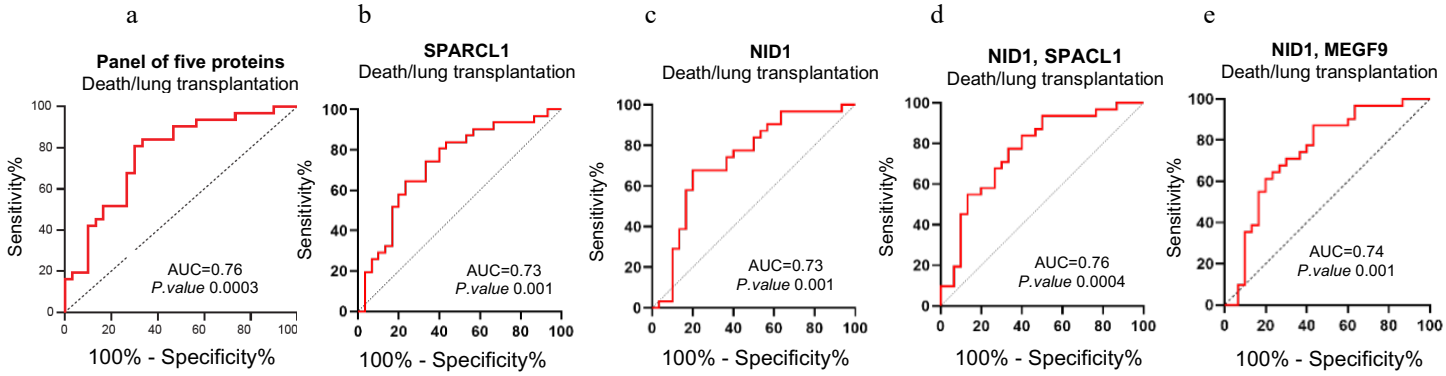

Figure 36: ROC curve measuring the risk of death/lung transplantation in PAH patients during years of follow-up. (a) ROC analysis for combination of five proposed biomarkers, (b) SPARCL1, (c) NID1, (d) NID1+SPARCL1, and (e) NID1+MEGF9 predicting the death vs. survival in validation (UK) cohort. The ROC accuracy has been tested with one-sided Wilson/Brown.

Finally, we performed an analysis to estimate transplant-free survival using the optimal cut-off values defined by the ROC analysis for each protein based on their performance in predicting event-free survival after transplantation (Figure 37). The results confirmed that NID1 alone, similar to SPARCL1, could differentiate PAH patients with a lower transplant-free survival rate, as shown by the log-rank test (P-value=0.007 and 0.002, respectively) (Figure 37a-b). In addition, NID1 in combination with one of the other proteins SPARCL1, MEGF9 and C1QTNF1 could also significantly predict transplant-free survival in PAH patients, but not in combination with CRTAC1 (Figure 37c-e). Finally, to demonstrate the predictive power of all five proteins together, we divided the patients into three groups based on the total number of proteins that were equal to or higher than the cut-off values, and the estimate of transplant-free survival was presented in a combined Kaplan–Meier plot (Figure 37f).

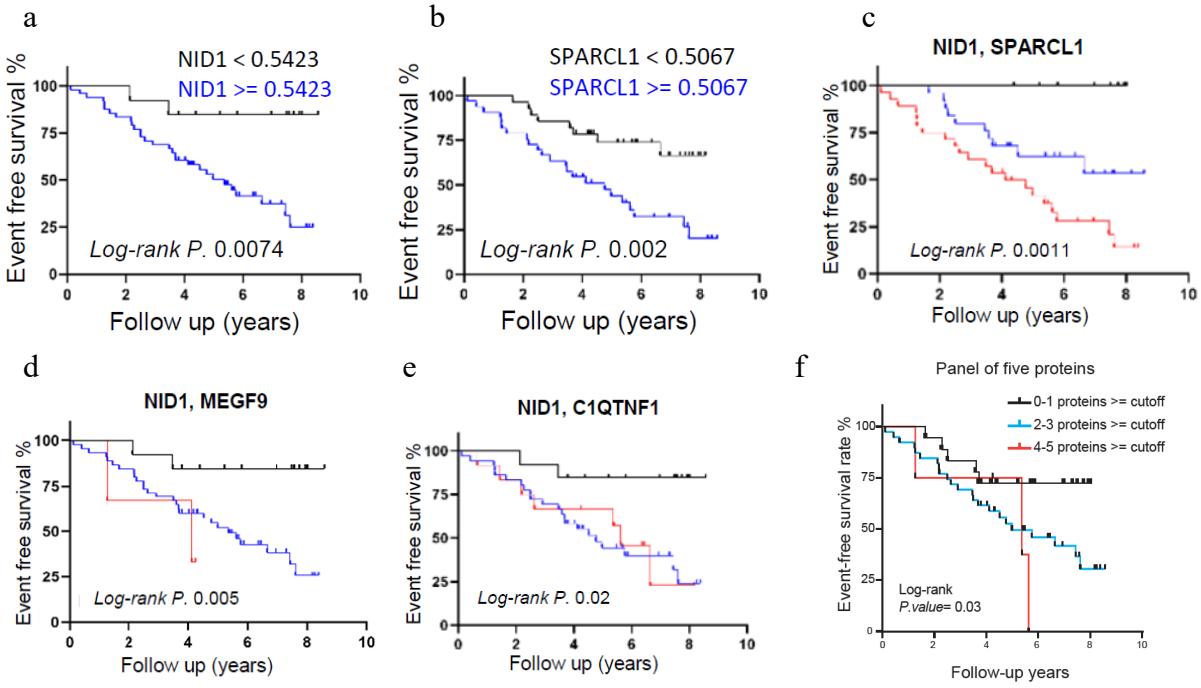

Figure 37: The event-free survival rate and associated log-rank test p-value for each single or combination of proteins. The Kaplan–Meier analysis shows the comparison between two groups: survived vs death/transplantation, using the optimal protein expression cut-off from the ROC curves for (a) NID1, (b) SPARCL1, and (c-e) NID1 in combination of three other proteins. Black = both expression lower than cutoff, blue= one cutoff criteria met, red= both expression higher than cutoff. (f) Comparison between two groups: survived vs death/transplantation, using panel of five proteins and based on total number of proteins that had expression equal or more than cut-off. Black= 0-1(proteins), blue= 2-3(proteins), and red = 4-5(proteins).

Overall, examination of our panel of five proteins in terms of their correlation with functional RV parameters from both cohorts and their impact on survival outcome from the validation cohort demonstrates that NID1 alone and in combination with other four ECM markers is associated with the development of a maladaptive right heart phenotype and can be targeted not only for prediction of RV status but also for prognosis and assessment of patient outcome in PAH.

4.10 Plasma levels of NID1, and C1QTNF1 can classify PAH patients with early vs. late decompensated RV

Since we found two subgroups of decompensated RV with a different transcriptional signature in both human and MCT-induced rats, we wanted to see if the proposed panel of five ECM proteins could also distinguish between the early and late decompensated phenotype of RV. To do so, we first needed an additional classification of PAH patients in plasma cohorts based on their RV function into early and late decompensated. Therefore, we utilized patients' MRI and echocardiography data to delineate the early and late stages of RV decompensation available

for the discovery cohort. Because RV-PA coupling accurately reflects right ventricular adaptation, it is a highly sensitive measure of the early stages of maladaptation.

Thus, we described the early vs. late stages of decompensated RV, similar to the compensated RV characterization, based on Ees/Ea ratio, calculated by the pressure-volume loop analysis as previously outlined[161], so that we considered patients with $0.8 < Ees/Ea < 1.2$ in early decompensation phase and patients with $Ees/Ea < 0.8$ in late-stage RV decompensation. However, in the validation cohort, we used the stroke volume to end-systolic volume ratio (SV/ESV), as a validated surrogate as previously established[183,184], to determine early vs late decompensated RV. Patients with $0.5 < SV/ESV < 0.8$ were classified as being in an early decompensated RV state, whereas those with $SV/ESV < 0.5$ were considered to be in a late decompensated state (Figure 38a-b).

We then compared the plasma expression of our potential biomarker panel within the newly defined decompensated subgroups, also in comparison to patients with compensated RV. Interestingly, C1QTNF1 and CRTAC1 showed significant regulation from early to late decompensated RV, while NID1, MEGF9 and SPARCL1 showed robust regulation specifically in patients with late decompensated RV in the discovery cohort (Figure 38c–g). On the other hand, in the validation cohort, significantly different regulation of NID1 and CRTAC1 expression was observed in PAH patients with early decompensated and late decompensated RV compared to patients with compensated RV (Figure 38h-i), whereas C1QTNF1 and MEGF9 were only regulated in patients with late decompensated RV (Figure 38j-k). Despite minor differences in expression changes between the two cohorts, the ROC results indicated that the panel of five proteins significantly discriminated between late and early stages of RV decompensation in PAH patients. (AUC−ROC =0.71 and accuracy=0.76 for the discovery cohort and AUC-ROC=0.73, accuracy=0.75 for the validation cohort) (Figure 38m). Of note, the prediction performance and accuracy are very similar when only four proteins (NID1, CRTAC1, C1QTNF1 and MEGF9) are used to accurately predict the early and late stages of RV decompensation in PAH patients (Figure 38n). This observation is consistent not only with the less significant expression of SPARCL1 in plasma and the RV, but also with the low RV tissue specificity of this protein[91].

Furthermore, assessment of feature importance in the RF model revealed that NID1 and C1QTNF1 were the most effective overall performances in predicting late decompensated RV in both cohorts (Figure 38o). In addition, CRTAC1 and MEGF9 proved to be promising factors for the same prediction in the discovery and validation cohorts, respectively. This is also reflected in the additional ROC analysis for the combination of the most effective factors in

each individual cohort (Figure 38p-q). The heart tissue-specific regulation of the two main factors present in both cohorts (NID1 and C1QTNF1) supports their higher predictive performance in discriminating stage-specific RV remodeling associated with PAH.

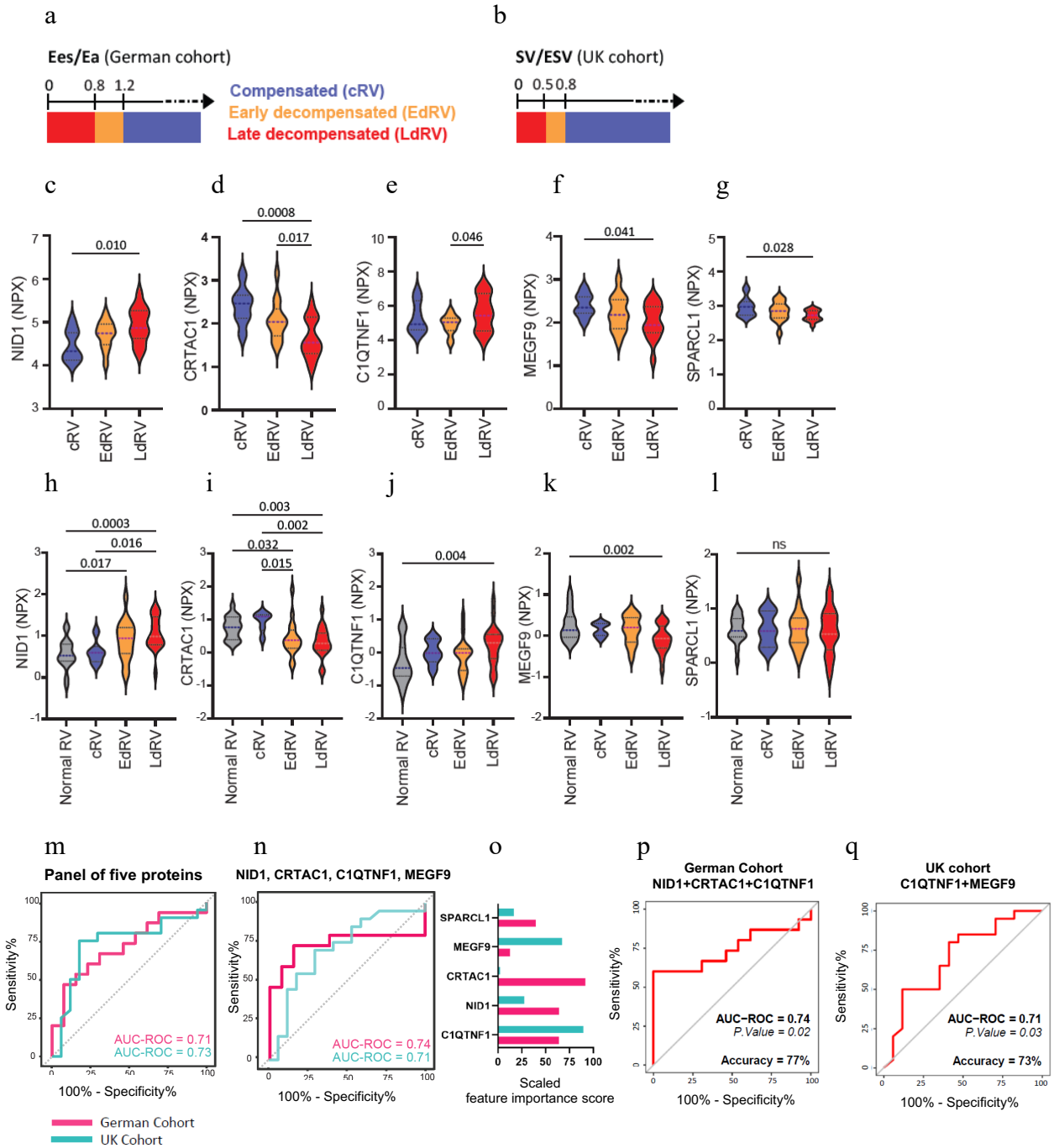

Figure 38: NID1 and C1QTNF1 proteins predict early vs. late decompensated RV in PAH. (a-b) thresholds that is used to group early vs late decompensated RV based on (a) Ees/Ea ratio, and (b) SV/ESV ratio. Plasma levels of five selected proteins in the (c-g) discovery cohort, and (h-l) validation cohort. *P-values* are calculated by one-way ANOVA. (m-n) ROC curve for both cohorts showing the prediction performance of the panel of five proteins (m), and four proteins, excluding SPARCL1 (n), distinguishing patients with late vs. early decompensated RV. (o) Scaled feature importance score for all five proteins in prediction of late vs. early decompensated RV. (p-q) ROC curve for the most effective factors in each cohort independently. (cRV = compensated RV, EdRV = early decompensated RV, LdRV = late decompensated RV).

5. DISCUSSION

Although right heart failure can be caused by a variety of etiologic processes, it is critical to identify common molecular signatures underlying the pathophysiologic transition of the RV from an adaptive to an irreversibly maladaptive state. Using human RV tissues and a rodent model induced by monocrotaline and pulmonary artery banding, we identified a comprehensive transcriptomic profile associated with the stages of RV hypertrophy and dysfunction in both men and women. This profile was further enhanced by integrative analysis of transcriptomic patterns with plasma proteomic data from PAH patients from two different cohorts (as discovery and validation), which yielded a number of significant results.

First, unsupervised k-means clustering of whole transcriptome profiles revealed molecular subgroups within both the compensated and decompensated RV states beyond their characterization based on hemodynamics. Second, significant dysregulation of interconnected biological pathways related to ECM, cell cycle regulation, energy metabolism and hypoxia, TNF-α and other inflammatory signaling was identified. Along the same pathway, we validated the expression of several candidate genes and proteins among the highlighted signaling pathways, especially those related to ECM components, suggesting that they underlie the pathological progression from an adaptive to a maladaptive state of RV failure. Third, the molecular mechanisms underlying sex-specific variations in RV adaptation in both human and animal models of RV dysfunction were uncovered. Fourth, we detected five ECM-associated biomarkers that show alterations in both the RV transcriptome and the plasma proteome: NID1, C1QTNF1, CRTAC1, MEGF9 and SPARCL1, which distinguish between compensated and decompensated states of the RV in PAH patients and are associated with worse clinical outcomes. Finally, we demonstrated that of these five parameters, circulating levels of NID1 and C1QTNF1 are indicative of early and late decompensated RV states in PAH patients, with an overall higher performance in predicting late stage RV decompensation in both cohorts. The identification of correlations between the underlying RV transcriptome pattern, plasma proteome and their clinical correlation in PAH patients has ultimately led us to identify RV-specific biomarkers and therapeutic targets using omics-based sub-phenotyping of RV remodeling in PAH patients.

5.1 Differentiating compensated and decompensated RV states reveals progressive pathophysiological stages in PH animal models

This research stands out as it aimed to contrast compensated and decompensated RV tissue from humans and two widely recognized PH animal models (MCT- and PAB-induced RV dysfunction). With the aim of considering similar rat strain (SD) for sequencing analysis and high similarity between the Su/Hx model and MCT-induced model[149,186]. we selected MCT –SD– rats for investigating pulmonary vascular-dependent RV remodeling, as it closely mimics human PAH pathophysiology, as well as development of prominent RV hypertrophy and failure, despite of exhibiting systemic toxicity, induced by monocrotaline[187,188]. In addition, to study vascular-independent mechanisms concerning RV remodeling, we performed transcriptome for PAB –SD– rats, which provides a significant insight into RV remodeling and failure, closely resembling the changes seen in human PAH-associated RV[189]. Furthermore, the banding of the pulmonary artery can have different degrees of constriction, as in our study allowing for controlled and predictable RV afterload increase, leading to either long-term compensatory hypertrophy, or RV failure with tight constriction[190,191]. On the other hand, SuHx rat model, leading to severe PAH in rats[192], poses several advantages, while in terms of RV remodeling, it is significantly dependent on the hypoxic condition, and therefore, variation in RV response and the possibility of reversed RV remodeling after being exposed to normoxic condition is higher in this model compared with MCT[190,193]. However, we appreciate that SU5416 + chronic hypoxia in rats over a prolonged period may better mimic the pathological condition of human PAH, which requires further comparison.

Nevertheless, using both MCT and PAB models in the same rat strain we made a comprehensive comparison between three RV transcriptomic profiles (using human RV), which verified a continuous progression from the initial adaptive phase to the uncoupled maladaptive stages, and distinctively highlighted genes and pathways associated with each stage and subgroup of the RV, offering deeper understanding into RV remodeling mechanisms associated with PAH. Furthermore, we described the progression from an adaptive to a maladaptive RV state as the early decompensated RV phase, which is distinguished by a unique transcriptomic phenotype, and further validated through the hemodynamic characterization.

Enrichment analysis results between our two animal models highlighted several important pathways commonly regulated in both. In both models, cell cycle regulations and proliferation were upregulated in the compensated phase of RV, and the adrenergic signaling of

cardiomyocytes was downregulated. These results are unique in delineating the molecular pathways underlying the compensated hypertrophy, as of today no other preclinical omics study provided the phenotypic transition of the compensated RV in MCT- and /or PAB-induced PH models, and they only focused on end-stage RV failure remodeling mainly after MCT treatment[150,194]. In addition, we observed that response to interleukin-1 was commonly upregulated in both MCT- and PAB- compensated RV, while IL-6 response was stronger in the MCT model. Moreover, a few metabolic pathways like amino acids, pyruvate, and triglyceride were exclusively downregulated in PAB-associated compensated RV. These results indicate an increased inflammation in the compensated RV along with the vascular remodeling in MCT-rats, which might be due to MCT's direct effects on heart inflammation[195], whereas in the PAB model, the metabolic shift occurs earlier due to acute pressure overload, independently of the pulmonary vessels.

Furthermore, we showed that many molecular pathways are regulated in a similar direction between MCT and PAB-induced decompensated RV. This includes ECM receptor reorganization, cell adhesion, PI3K/Akt signaling, several immunological pathways such as leukocyte aggregation, and TNF-α regulation, as well as dysregulation of multiple metabolic processes, notably the oxidative phosphorylation and FAO, reflecting the strong hypoxic shift between compensated and decompensated RV. These findings were a great extension to the available RV transcriptome from other animal models of PH, as it provides a comprehensive comparison between PAB and MCT models, and with human RV dysfunction. Potus et al in 2018 provided an overall characterization of RV failure in MCT rats associated with fibrotic, inflammatory, antigenic, and metabolic abnormalities[194]. Later in 2020, Cao et al performed a similar RNA-seq on RVs from PAB-rats and showed pathways such as ECM–receptor interaction, Toll-like receptor (TLR), and NF-κB signaling were upregulated in the PAB-RVs compared to sham[196]. However, this study focused only on acute banding effects, which do not reflect the RV responses in the MCT treatment or the PAH pathology. Park et al in 2021, performed a comprehensive transcriptome analysis on both MCT and SuHx rat models and identified the common pattern of RV failure is significantly associated with upregulated endothelial to mesenchymal transition, inflammation, TNF-α regulation, and angiogenesis, while they precisely described the downregulation of oxidative phosphorylation and fatty acid metabolism in these two models[146]. Findings from this study accurately complement our results where we showed that the downregulation of oxidative metabolism and FAO is in line with the hypoxic shift happening in decompensated RV development. Further evaluation of

mitochondrial oxidative metabolism and TCA cycle-associated genes in SuHx-induced rats RV failure was performed by Kobayashi et al in 2022, where they reversed this effect by Chrysin and therefore improved RV function[148]. The current study, further supports that this metabolic shift between compensated and decompensated is essentially associated with dysregulation of fatty acid metabolism as we demonstrated a similar pattern in PAB rats, in line with two other models. It has been also shown that preventing this downregulation reduces the RV systolic and diastolic dysfunction in MCT rats[197].

In addition, ECM receptors interaction shown as the top regulated pathway in the transition from RVH to RVF in our study confirms the previous observation in the SuHx rats[148], in line with a recent observation in rats following 8 weeks of PAB[198]. This suggests that ECM reorganization is one of the main alterations associated with pressure overload hypertrophy and subsequent failure as it is observed in earlier stages in our PAB model compared to MCT, while it was not a common regulation between SuHx and MCT model[146]. Consistently, ECM reorganization was regulated in the early decompensated phase of RV in our MCT model, confirming its role in the transition from adaptive to maladaptive hypertrophy. Interestingly, we observed that reorganization of the extracellular matrix emerges as the most pronounced dysregulation in PAH patients with decompensated RV, in line with two animal models. In addition, responses to various cytokines and inflammatory substrates were dysregulated in PAH-associated decompensated RVs similar to both rat models. However, the molecular changes underlying the decompensated state of the RV in the MCT model were more prominent compared with PAB-induced RVs, and better mirrored human PAH-associated RV decompensation.

5.2 Establishing an extensive molecular profiling of RV remodeling in patients with PAH through advanced transcriptome analysis

Following the characterization of compensated and decompensated RV functional and molecular transitions in animal models, we obtained over 40 human RV specimens, predominantly associated with PAH. These patients samples were categorized into two distinct groups based on cardiac index and TAPSE measurements, delineating them with either compensated or decompensated RVs. Through the initial transcriptome analysis, we observed a greater differential expression in the decompensated RV condition, while no significant DEGs were identified within the compensated group. This observation can be attributed to the considerable heterogeneity found across the human RV samples, as revealed by transcriptome

analysis, which was not only limited to the compensated and decompensated RV groups but was also evident among the donor samples, as they were derived from individuals with diverse clinical backgrounds. Consequently, despite identifying certain molecular pathways, including ECM receptors, TNF-α activation, and oxidative metabolic pathways, this pronounced heterogeneity limited our ability to identify a precise molecular profile for compensated and decompensated RV conditions in PAH patients. To address this challenge, we established a strategy to dissect the heterogeneity of human RV remodeling from multiple aspects, which included unraveling the molecular distinctions between male and female subjects, as well as identifying molecular subgroups within the compensated and decompensated RV samples by an unsupervised approach.

Despite the observed heterogeneity among our PAH-associated RV samples, it led to the discovery of the second independent human RV transcriptome, published in Nature Cardiovascular Research[159] in September 2023, and it is unique in several aspects when compared with the last published human RV-omics study[152]. Following a different aim, here we first performed a precise molecular phenotyping of RV remodeling by identifying subgroups within compensated and decompensated states of the RV in PH patients and in animal models to assess whether any of these alterations could serve as biomarkers for early detection of maladaptive RV remodeling. In contrast, Boucherat et al. aimed to identify novel molecular players involved in maladaptive RV remodeling with the goal of optimizing risk stratification in PAH. Second, the current study/manuscript focuses primarily on phenotyping subsets of RV dysfunction in PAH patients using an unsupervised clustering approach and identifying the differences underlying RV remodeling heterogeneity in humans. In addition, the current study is unique in terms of providing knowledge on several other levels: 1. Examining the landscape of the sex-specific transcriptome in human and animal models with compensated and decompensated states of RV, which allows us to characterize the similar and different molecular mechanisms, as well as changes related to sex hormones underlying the transition from compensated to decompensated state in males and females. 2. The study compares transcriptomes from two different animal models of RV dysfunction with human data and confirms a phenotypic subdivision (early and late) of RV dysfunction beyond clinical parameters. 3. The study provides a new set of transcriptome-based ECM molecules that can distinguish not only between adaptive and maladaptive states of the RV but also between early and late RV decompensation in PAH patients, suggesting new targets for the diagnosis and prognosis of early to late RV hypertrophy in PAH. It also demonstrates that a group of secreted

ECM proteins can better predict survival of PH patients than a single protein, which significantly correlates with the state of RV hypertrophy rather than pulmonary artery remodeling. 4. Finally, genes and signaling pathways beyond ECM regulation have been proposed to distinguish between different clusters of decompensated RV (e.g., in cardiomyopathy and PAH-associated decompensation).

5.3 Estrogen and fatty acid metabolism: key major molecular drivers of female-specific RV adaptation in PAH

Our RNA-seq analysis of human RV tissue from both sexes and female RV tissue from MCT-induced rats provided crucial information on the sex-specific molecular profile of RV adaptation. The results highlighted that although there are pivotal molecular distinction in the transition from the compensated to the early and late decompensated phases regardless of sex, females may take a different path to the onset of the decompensated phase or maintain the compensated state of the RV for a longer period of time. Our results suggest that the potential protective mechanism against decompensated RV states in female PAH patients is primarily due to estrogen responses as well as fatty acid metabolism, while highlighting a distinct histone methylation activity in the females via specific histone demethylase enzymes such as KDM2B. Indeed, the data suggests that estrogen responses are the main contributing factors for the prolonged compensated RV in female but not in male PAH patients. Moreover, compensated RV function in males' exhibits a similar pattern of deterioration as observed in the decompensated phase, characterized by enhanced cell death signaling and premature activation of immune cells, including T cells and neutrophils. This suggests an increased vulnerability to pro-apoptotic and pro-inflammatory signaling pathways in the absence of estrogen[95,199], consistent with the altered cardiac phenotype observed in other cardiovascular diseases[200–202]. In contrast, decompensated RV in females is largely determined by hypoxia regulation and fatty acid metabolism, which are directly or indirectly modulated by the additional presence of estrogen. Analysis of female MCT rats showed that female rats follow a different pathway to develop a decompensated state or to maintain the compensated state of the RV in the long term. We observed that the protective mechanism against the decompensated RV in the female animal model depends mainly on fatty acid β-oxidation, whereas in the male animal model the RV undergoes maladaptive development associated with massive remodeling of ECM collagens, as described in previous publications[203].

Indeed, the female rats exhibited a similar pattern of hypoxia and fatty acid metabolism as PAH-associated RVs from patients, consistent with the superior RV function reflected in the

higher cardiac output of female MCT rats. However, the relationship between estrogen and mitochondrial fatty acid metabolism and its influence on female RV function remains to be further elucidated.

In addition, evaluation of the components of estrogen and progesterone metabolism revealed that several downstream signaling pathways are significantly regulated in female PAH-decompensated RV, such as both “membrane-initiated steroid signaling pathways (ADCY, MAPK, AKT3)” and “nuclear-initiated steroid signaling” pathways" (RARA, KRT, HSPA), cAMP biosynthetic processes and G-protein-mediated signaling pathways. These data suggest that adverse RV hypertrophy and remodeling in female PAH patients is not directly influenced by estrogen, but rather that upstream or downstream signaling pathways regulated by sex hormones influence RV remodeling[108,204].

Conversely, male PAH patients did not show similar upregulation of the corresponding genes, suggesting that estrogen signaling is not as effective in male as in female. Of note, differential co-expression of certain transcription factor complexes (HIF1A/NFkB1 in female rats versus IRF5/EGR2 in male MCT rats), along with unique histone demethylase activities associated with the sex chromosomes (KDM6A and KDM5C in female rats versus DDX3, KDM5D, and EIF2S3Y in males), demonstrated that the sex-specific differences in RV remodeling in both human and animal models with RV dysfunction are not only due to the existence of different sex hormones, but are also controlled by the sex chromosomes as an upstream sex-related regulatory element. The role of sex chromosomes has been studied previously[205,206], in particular the protective role of Kdm5d expression together with several other factors on the Y chromosome has been deciphered in the MCT animal model of PH[207]. As our study was conducted in transplanted end-stage RVs, longitudinal studies in PAH patients and in animal models could confirm and provide a better understanding of the sex-specific differences in RV adaptation in PAH.

5.4 Comprehensive analysis of human RV remodeling reveals molecular subgroups of adaptive to maladaptive hypertrophy

To further delineate the heterogeneity of RV remodeling, we used an unsupervised clustering approach and determined different subgroups of compensated and decompensated RV in PAH patients by transcriptome profiling. Remarkably, most signaling pathways, especially in the two decompensated states in human RVs, were regulated in a similar direction as in MCT-treated rat RVs, which not only confirms the identified changes but also demonstrates the

relevance of current animal models to study PH. Within the compensated human RV samples, a subset (cluster C) of samples exhibited a molecular profile very similar to that of decompensated end-stage RV (cluster E). Further investigation revealed that two out of three samples were cases of severe RV/LV hypertrophy, which explained their different molecular phenotype. Our results suggest that a specific compensatory RV state may (more rapidly) transition to maladaptive hypertrophy and promote RV failure. The exclusive signaling pathways leading to this particular compensatory state involve the regulation of angiogenesis, the Notch signaling pathway and in particular endothelial cell migration and dysregulation. This emphasizes the critical role of dysregulated angiogenesis in the development of maladaptive RV failure, as previously described[69,85,208,209]. Indeed, RV hypertrophy may be beneficial if the proper balance between angiogenesis and increased mass ratio is maintained, and these data suggest that disruption of the angiogenesis balance, e.g., by altering Notch signaling, impairs adaptive RV hypertrophy.

Furthermore, we compared two decompensated RV subgroups (clusters D and E) and showed a strong reorganization of ECM and fibrillar collagens, which were upregulated in both groups, but already increased in the early stages of decompensation and further increased in the late decompensated RV. In addition, one of the subgroups (cluster E) relies mainly on downregulation of fatty acids and shows high levels of inflammation and leukocyte activation, while the other (cluster D) shows significant upregulation in hypoxia regulation such as HIF-1a signaling. When compared with MCT-induced rat RVs, early decompensation was more similar to cluster E, as downregulation of FAO was observed at this stage, whereas the higher ECM interactions and hypoxia regulation observed in MCT-late decompensated RVs were closer to cluster D gene expression. On the one hand, these results suggest that the point at which RV hypertrophy fails to adapt begins with a sudden downregulation of FAO, followed by hypoxic metabolism. The role of FAO previously shown in the RV[69,210,211] is consistent with our findings and, together with the corresponding genes identified in this study, particularly the carnitine shuttle protein, provides novel therapeutic targets for RV remodeling.

On the other hand, although we found similarities with MCT-induced decompensated RV, we cannot confidently assign the early and late phases to human clusters D, E of this study. First, immune responses are more pronounced in MCT rat RVs and occur in both the early and late phases of decompensation, whereas in PAH patients increased activation and recruitment of immune cells specifically found in cluster E. This may be partly due to monocrotaline toxicity, which induces more persistent inflammation in the MCT model[212]. However, aggregation of

immune cells, such as T cells, in cardiac tissue has been previously demonstrated as a feature of maladaptive RV insufficiency in late-stage PAH as well as other cardiac dysfunctions[213–216].

Second, the immense downregulation of oxidative phosphorylation accompanied by an upregulation of glycolysis, known as the "Warburg effect" in energy metabolism, is more pronounced in cluster E, similar to late decompensated RV in MCT rats. This shift in energy metabolism towards anaerobic metabolism has previously been associated with maladaptive RV hypertrophy and fibrosis[69,209,210,217–219], so in this respect cluster E may resemble the later stage of RV remodeling in PAH patients. Therefore, although our integrative transcriptome with the MCT rat model allowed us to describe some crucial signaling pathways associated with the transition from adaptive to maladaptive RV, we are cautious about using early and late designations for the decompensated RV in humans and prefer to stick to two distinct subgroups of the decompensated RV in humans. A summary of the main signaling pathways that distinguish between the two subgroups of decompensated RV is shown in Figure 39.

Overall, through the extensive and integrative transcriptomic profiles of the RV, our subphenotyping approach suggests that the molecular transition may precede the functional transition (in terms of hemodynamic parameters such as PVR, RVEDP, and CO) from an adaptive to a maladaptive RV, providing valuable insight into the pathobiology of disease progression. These findings are unique compared to other published transcriptomic studies in human and animal models of RV dysfunction[146,148–150,152,194] and suggest that the transition from initial stages to adaptive, maladaptive, and RV failure stages is a continuum in which specific biological pathways change fluidly through the stages. The genes and pathways associated with each RV stage/subgroup identified in this study provide a deeper understanding of the RV remodeling mechanisms associated with the different PAH stages and open up new therapeutic opportunities.

Furthermore, we have demonstrated that distinct signaling pathways such as TNF-α activation via NF-κB, epithelial mesenchymal transition, and activated inflammatory responses serve as distinguishing features between decompensated RVs associated with PAH and those associated with cardiomyopathy. In contrast, in RV failure with dilated cardiomyopathy, interferon signaling pathways and the corresponding genes and molecules were significantly enriched. This was consistent with previous studies of myocardial infarction, in which massive synchronous cardiac cell death leads to the release of damage-associated molecular patterns

and an abnormal response to self-DNA and induces the release of type 1 interferon, followed by an innate immune response and deterioration of LV function[220].

5.5 An integrative transcriptomic analysis of MCT-rats and human RV dysfunction highlights key genes involved in adaptive to maladaptive RV transition

Through our interspecies (human, rat) integrative transcriptome analysis, we identified key biological signaling pathways associated with the adaptive-to-maladaptive transition, particularly changing in the early decompensated RV phase, and then shortlisted the corresponding genes as potential candidates to test their expression at both RNA and protein levels. Three hypoxia-regulated factors (*Hmox1*, *Eno3* and *Angp1*) showed a strong correlation with the transition from adaptive to maladaptive RV, suggesting that the augmentation of hypoxia response[221] and altered glycolytic activity are exclusively associated with impaired angiogenesis in the decompensated RV[222], which is consistent with previous studies[223], and suggests them as strong candidates for further validation and functional assessment in PAH. In terms of proliferation and cell cycle activity, we found a significant downregulation of *WNT5A* and *FGF9* that correlates with the transition from compensated to decompensated RV. This suggests that an imbalance in proliferation control, triggered by an increase in TGFB1 (proto-oncogene) and pro-inflammatory cytokines such as IL18, mediates this transition and is associated with maladaptive RV formation[224].

Alterations in ECM component and receptors was predominant in this study, demonstrating drastic upregulation throughout the transition of adaptive to maladaptive RV in both human and rat samples. As previously described[121], the structural remodeling of the myocardium and alterations in cardiac ECM composition and abundance are directly linked to for adaptive cardiac response to chronic pressure overload[225,226]. Moreover, myocardial fibrosis, primarily involving the restructuring of collagen fibrils, plays a pivotal role in the development of RV failure[128], and in both adaptive and maladaptive RV formation in PH[132,227].

In our study, we shortlisted and validated two groups of ECM-related targets in PAH-associated RV. First, we selected seven candidates known to be regulated in cardiac hypertrophy and remodeling[146,150,228,229]: *Nppa, Fn1, Col1a1, Itgb6, Tnc, Mmp9* and *Timp1*, considering their differential impact on global RV remodeling from adaptive to maladaptive RV. Further RNA expression and functional correlations with RVED in MCT rats revealed a strong correlation between the expression of *Nppa*, *Fn1*, *Itgb6* and *Mmp9* and increased RVEDP in the maladaptive RV. Furthermore, our observation of increased *Mmp9* expression

and its correlation with RVEDP is consistent with increased plasma MMP9 levels previously reported in patients with diastolic heart failure[230]. Remarkably, MMP9 not only processes a variety of ECM substrates such as collagen and fibronectin, but also non-ECM substrates such as interleukin IL-1β and latent TGF-β[231], which we found to be upregulated in both compensated and decompensated RVs in human and MCT-induced rat samples. These results suggest that all of these seven candidates play a potential role in maladaptive RV remodeling associated with PAH. In particular, the alteration of five proteins (NPPA, FN1, TNC, COL1A1 and MMP9), which have been shown previously[232–236] to have a critical impact on cardiac ECM development and remodeling, indicated a strong increase in collagen turnover and RV fibrotic remodeling during the transition from compensated hypertrophy to decompensated RV failure. However, as ECM turnover is a continuous process during the transition from hypertrophy to failure, we found only *Itgb6*, *Mmp9* as well as the already known *Nppa* to be significantly altered between the compensated and decompensated RV, making them potential prognostic candidates for PAH-associated RV dysfunction.

In addition, we validated the second list of ECM-related targets (13) that we shortlisted based on the collective DEG analysis between the newly identified human RV subgroups at the protein level in the RV. First, using five curated RV proteome datasets that were publicly available[147,150–152,180], we were able to find seven proteins that share the same expression pattern in the RV, indicating a strong correlation between mRNA regulation and protein abundance. Among the six remaining proteins, we found evidence for regulation of MMP9 and TIMP1 in two different plasma proteomes[181,182]. The absence of these proteins in the RV proteome could have two possible reasons: First, protein levels in RV tissue are inherently low, making them undetectable by proteomic assays, which is particularly relevant for secreted proteins such as TIMP1 that do not persist long enough in the cell post-translation. TIMP1 was identified in the RV transcriptome of another PAH animal model, supporting this hypothesis[146,148]. Second, the low protein levels in the RV coupled with a strong increase in the plasma proteome may indicate that other tissues and cells affected in PAH actively release these proteins into the blood. In particular, MMP9 shows significant upregulation at the transcriptome level in pulmonary artery smooth muscle cells (PASMCs), supporting this idea[237].

Four additional candidates (ITGB6, ITGA10, HMMR and SPP1) that did not show proteomic evidence in the public RV datasets were additionally detected in other relevant public transcriptomes, confirming our findings on transcriptional regulation[146,148,163]. By adding our Western blot analysis to validate their RV protein levels, we demonstrated that ITGA10 and

SPP1 are significantly regulated in the decompensated versus compensated RV, in correlation with their mRNA regulation, suggesting their potential influence on ECM remodeling that enables the transition from an adaptive to a maladaptive RV in PAH.

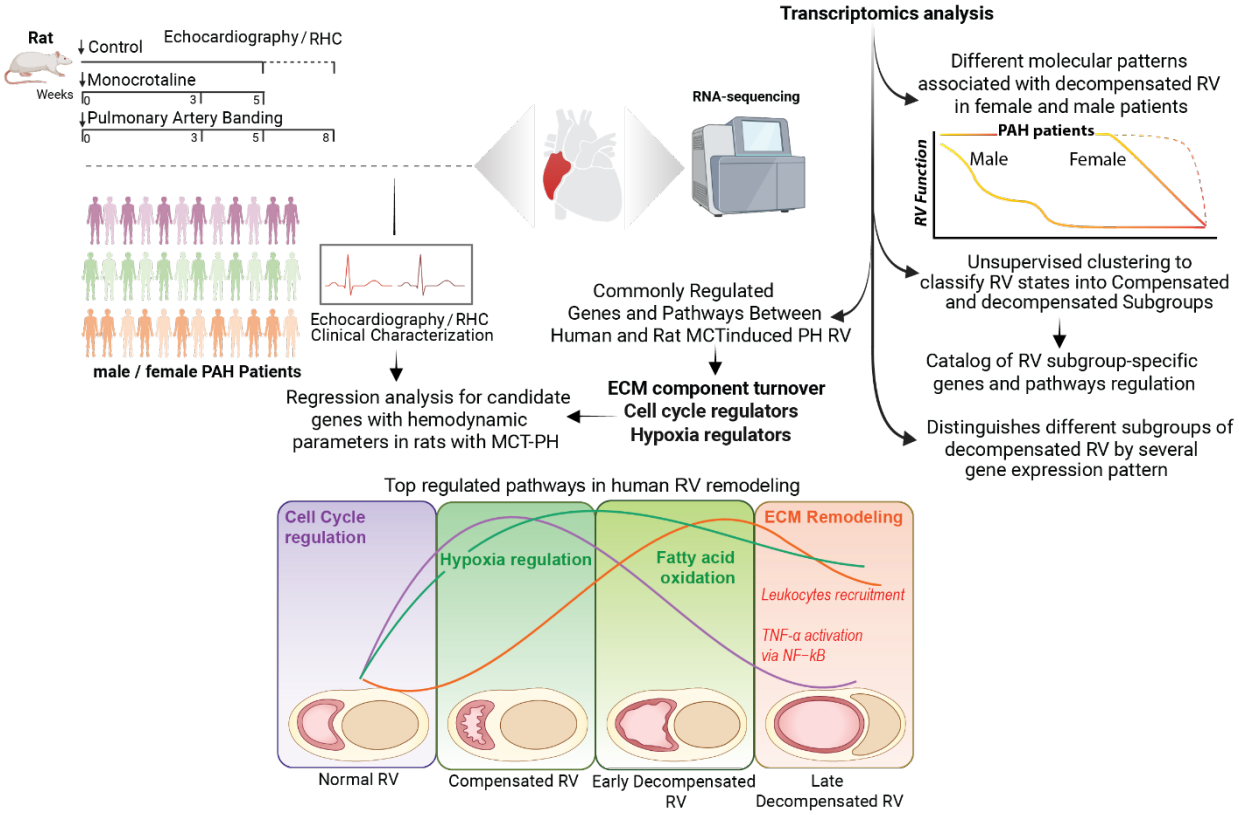

Figure 39; Schematic overview of integrative RV transcriptome analysis approach employed in this study. *Created with BioRender.com.*

5.6 ECM remodeling determines RV failure and PAH patients outcome

Although the altered pulmonary vasculature is the primary cause of PAH progression, it is safe to say that extensive remodeling of the ECM and cardiac basement membrane is a key determinant of the extent of RV adaptive response and ultimate failure, and therefore contributes directly to morbidity and mortality in PAH[113,227]. Alterations in various components of the ECM have been identified in a variety of cardiac pathological conditions[238]. In addition to the important role of structural and non-structural cardiac matrix proteins, ECM homeostasis is maintained by a delicate balance between MMPs and TIMPs (MMP modulators) that control remodeling of the ECM and its key components, such as collagens, thereby maintaining ECM integrity and facilitating its function. There are several reports that patients with PH have elevated MMP and TIMP levels, indicating remodeling of the ECM[127,239]. In the heart, cardiomyocytes and fibroblasts express MMPs (primarily MMP-2, MMP-9, and MMP-13) that degrade ECM collagens, including types I and III. MMPs are primarily stored as inactive extracellular forms and, once activated, degrade various ECM proteins, affecting tissue

structure and cell function[240]. While the differential expression of MMPs provides a detailed insight into the remodeling phases of the RV in PAH, their detection in both RV tissue and blood circulation requires highly sensitive assays.

As fibrosis may play a dual role in the transition from compensated to decompensated RV, firstly by supporting the collagen network to prevent dilation and secondly by causing excessive RV stiffness potentially leading to RV failure[128], we must be cautious in identifying the specific ECM-related targets and their contribution to RV fibrosis while associated with the adaptive to maladaptive transition. It is now clear that targeting ECM proteins is one of the potential routes to innovative therapies and prognostic methods in PAH. Further translational research should identify the key ECM protein alterations responsible for RV remodeling and failure in PAH[113]. On the other hand, although ECM proteins have gained importance in studies of vascular remodeling, their role in RV remodeling in PAH requires further research, including determining whether changes in ECM protein expression directly contribute to the cause of RV dysfunction in PAH. In this regard, combining the RV proteome and further functional assessment of the RV with our transcriptome subphenotyping approach is an essential next step in targeting cardiac ECM and potentially reversing RV remodeling in PAH. Such studies could pave the way to improve prognostic and therapeutic methods to preserve RV function and improve outcomes for PAH patients. In this study, we investigated both structural and non-structural key ECM components, as well as enzymes that regulate ECM turnover in the RV, and provided additional evidence for their changes during the transition from adaptive to maladaptive states. Our new candidates, together with the known ECM markers, provide a panel for RV-specific therapeutic targets. Therefore, our study represents a major extension of previous investigations into the role of ECM-related proteins in RV remodeling in PAH and explores their potential therapeutic and prognostic significance.

5.7 Circulating levels of ECM-associated proteins serves as potential RV-specific biomarkers

It is not only the dysregulation of cardiac ECM in RV tissue that determines disease severity and transitions between RV stages in PAH, but also the increased (or decreased) circulating levels of several ECM-related proteins (such as collagens and MMPs, thrombospondin-1/endostatin) [127,241,242] that have been shown to be associated with RV remodeling and poorer outcome in PAH patients. Assessment of circulating levels of ECM-related markers therefore shows promise for the diagnosis and prognosis of PAH in relation to the state of the RV. To

this end, we combined the results of our RV transcriptome analysis with proteomic data from the plasma samples of a PAH cohort, which also confirmed a massive deregulation of ECM molecules between different RV states that may serve as pathophysiologic RV-specific biomarkers. For confirmation, we detected five ECM-related biomarkers: NID1, C1QTNF1, CRTAC1, MEGF9 and SPARCL1, which can distinguish between compensated and decompensated states of the RV and are significantly associated with worse clinical outcomes in PAH cohorts (Figure 40).

NID1, which has been shown to be the major dysregulated plasma protein in our study (significantly upregulated in patients with early and late decompensated RV) and has been shown to be associated with prediction of the maladaptive phase of RV, is an essential component of the basal lamina of cardiac tissue and plays a crucial coordinating role in basement membrane assembly, while nidogen-laminin interactions are essential for basal lamina stabilization[243]. Kim et al. pointed out that differential protein expression of collagen IV, laminin α2 and NID1 during basal lamina remodeling and decreased myocyte adhesion accompany basal lamina remodeling in ischemic injured hearts compared to non-injured human hearts[244]. On the other hand, NID1 has been shown to significantly improve cardiac function and angiogenesis in a mouse model after myocardial infarction[245]. Whether the upregulation of *NID1* plays a protective or pathological role in RV remodeling requires further investigation. In our study, we found that NID1 has the best predictive power for discriminating between patients with decompensated and compensated RV, demonstrating its potential as an RV-specific prognostic biomarker in PAH. Given its key role in maintaining the basal lamina of RV tissue, *NID1* also offers itself as a potential target for RV-specific therapies that may promote the adaptive RV response in PAH patients.

C1QTNF1 (CTRP1), the second predictive biomarker in our study, is from a family of adiponectin paralogs, many of which have been studied in recent years for their role in cardiovascular disease. Circulating C1QTNF1 levels have been found to be elevated in patients with coronary artery disease and closely associated with adverse events[246–249]. In our study, *C1QTNF1* expression is elevated in both RV tissue and plasma levels in the early decompensation stage of RV. Based on previous studies, our results suggest that upregulation of *C1QTNF1* in RV tissue may modulate maladaptive RV remodeling by promoting further inflammation and oxidative stress through macrophage activation[250,251].

SPARCL1, another dysregulated plasma protein in our study, is a matrikine with a structural similarity to SPARC that binds to calcium upon secretion and interacts with the ECM to create intermediate states of cell adhesion[252]. Due to its dynamic extracellular functions, SPARCL1 is upregulated in pathological cardiac remodeling and plays an important role in regulating fibrotic, inflammatory and angiogenic processes[252,253]. In the RV context, *SPARCL1* has been shown to be more highly expressed in the RV than in the LV[254]. Elevated levels of SPARCL1 are a biomarker of pathologic RV remodeling and have been associated with RV maladaptation and ventriculoarterial uncoupling in PH[255]. However, our study showed that plasma SPARCL1 levels were significantly altered in only one of the PAH cohorts (Germany), suggesting that further studies on this protein and its regulation in the RV are essential to uncover its potential as a prognostic biomarker to distinguish between adaptive and maladaptive RV in PAH.

CRTAC1 (cartilage acidic protein-1) is primarily known as a glycosylated extracellular matrix protein found in the deep cartilage matrix. Previous studies have identified the CTRAC1 protein as a blood biomarker for ischemic stroke outcome[256]. In addition, another study showed that inhibition of *CRTAC1* significantly reduced TNF-α and interleukin-6 levels, thereby reducing inflammation[257]. In contrast, *CRTAC1* expression was found to be downregulated in atherosclerosis macrophages compared to normal macrophages in human tissue[258]. In this study, the reduced expression of CRTAC1 proteins in plasma was in contrast to the increased mRNA levels observed in the transcriptome of the decompensated RV. This discrepancy could be due to lower gene expression in RV tissue, resulting in a lower detection rate of the transcriptome experiment. However, it could also indicate a greater release of these two proteins from other organs affected by PAH, such as pulmonary artery cells in the lung[253,259,260]. These results are consistent with previous studies and suggest that differential expression of *CRTAC1* across different human tissues and conditions may be responsible for the contractive results. Therefore, further studies on this protein are needed, especially with regard to RV remodeling in the context of PAH.

Finally, MEGF9 was identified in our study as a potential marker that is decreased in maladaptive RV tissue compared to adaptive RV tissue, which correlates with its decreased plasma levels in end-stage PAH patients. Recent studies have shown increased expression of *MEGF9* in myocardial infarction[261], warranting further analysis of its role and therapeutic potential in PAH-related RV remodeling, while this study highlights the promising prognostic value of *MEGF9* in the context of PAH.

In this study, we used a random forest model to assess the ability of the five ECM proteins to predict different RV dysfunction states in relation to disease severity and showed that the panel of five identified proteins (even when excluding SPARCL1) significantly discriminated between PAH patients with compensated RV and those with decompensated RV in both the discovery and validation cohorts. Furthermore, we demonstrated that plasma levels of NID1 (also in combination with MEGF9, SPARCL1 and C1QTNF1) can significantly differentiate PAH patients with poorer survival, suggesting that the panel of the five ECM proteins individually or in combination with other prognostic factors such as proBNP levels, hemodynamic or imaging findings may serve as prognostic biomarkers. The five proteins (specifically NID1, C1QTNF1, CRTAC1 and MEGF9) were able to distinguish early from late stages of RV decompensation as defined by various RV functional parameters in both cohorts, with NID1 and C1QTNF1 remaining the most significant predictive and prognostic factors associated with early stage RV dysfunction.

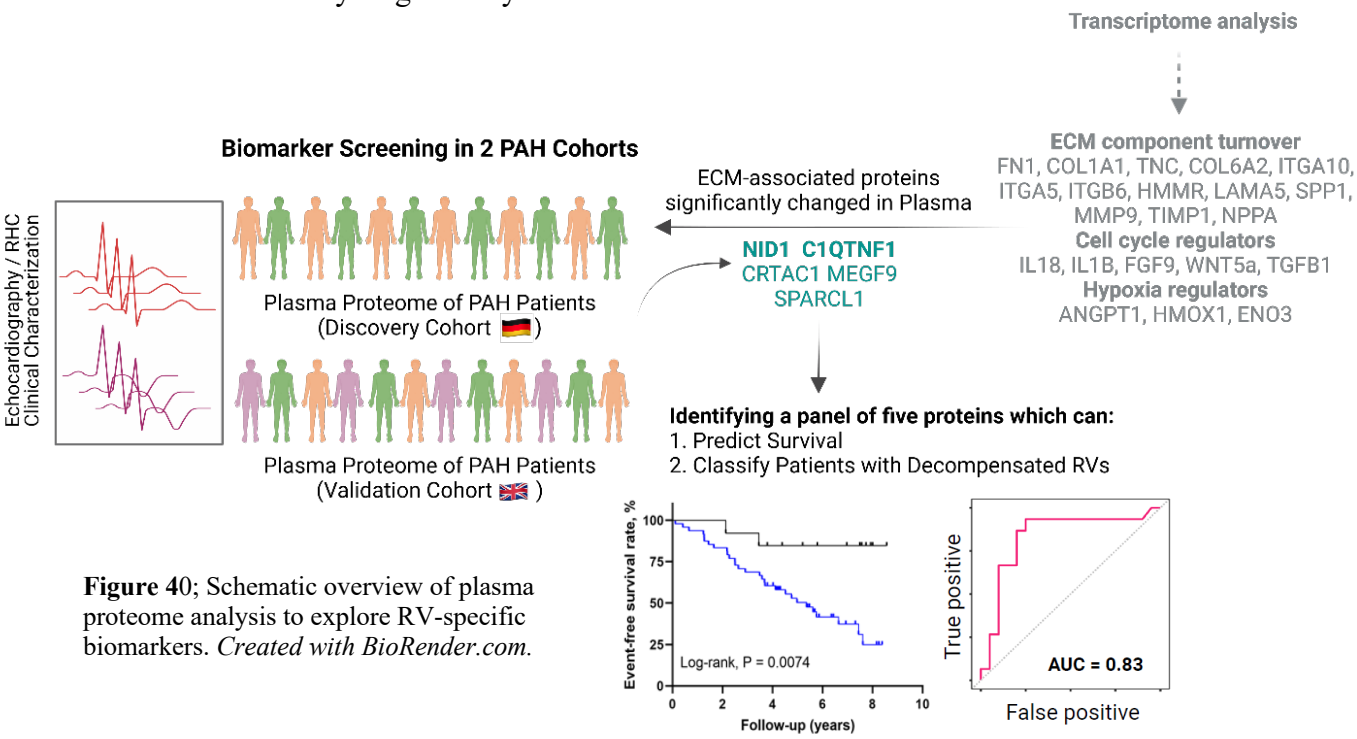

Figure 40; Schematic overview of plasma proteome analysis to explore RV-specific biomarkers. *Created with BioRender.com.*

5.8 Extensive multi-omics analysis offers several benefits but also has certain limitations

The increasing number of molecular profiles of PAH underscores the transformative role of omics technologies in PAH treatment. Omics data and their comprehensive analysis contribute to early diagnosis, improved prognostic stratification and drug repurposing[141]. Omics approaches are instrumental in improving prognosis by identifying biomarkers that predict disease stage, severity and response to treatment, leading us to personalized PAH therapy. Our study takes a similar approach and focuses on proposing a panel of prognostic biomarkers for

right ventricular remodeling - an area that is less explored in PAH compared to vascular remodeling, but is critical for patient outcomes.

In this study, we used different machine learning (ML) methods to test our hypothesis at each step, including both unsupervised (k-means) and supervised learning algorithms. Choosing the right ML method depends on several factors, such as sample size, metadata heterogeneity and its influence, and the relevant biological question. In this study, we used a regression model to analyze the functional correlations of protein expressions and a random forest model to evaluate the predictive accuracy of biomarker panels. Both methods are widely recognized in PAH research for their robustness among all supervised machine learning methods in this field[141]. We used a random forest model to discriminate PAH cases with compensated and decompensated RV based on the expression of the five proteins. To avoid overfitting due to the limited sample size in the training group, we used a cross-validation approach, while the model demonstrated robust validity in a separate, independent cohort, confirming the consistency and reliability of its performance and results[262]. The choice of the random forest model to assess the accuracy of our ROC analysis offers several advantages, such as: Versatility in handling different types of data (categorical such as sex and RV phenotype and numerical such as gene and protein expression), randomness and reduction of variance of the model, and reduction of overfitting[263]. In addition, the random forest model is able to measure the relative importance of each feature in prediction, which in our study helped to identify the most effective proteins in discriminating between early and late decompensated RV in PAH cohorts (NID1 and C1QTNF1) and shed light on their specific role in maladaptive RV formation.

Our study has some limitations. The primary limitation in performing unbiased molecular profiling (omic) methods, as in our study, is the limited availability of clinical samples from human subjects at different stages of RV dysfunction, along with the limitations in performing longitudinal studies during different disease stages, resulting in a small number of human samples in each subset of RV states for in-depth computational analysis. In addition, due to the small number of human samples for machine learning methods such as k-means clustering and linear regression to infer correlations between RV conditions and confounding metadata factors (such as patient sex and age), we should be cautious about drawing definitive conclusions. The limited sample size likely results in underpowered machine learning and thus lower ROC-AUC values, both for positive and negative/no differences[264]. Furthermore, the heterogeneity within our human RV samples, reflecting the intricate etiologic complexity of RV remodeling in PAH, attenuates the results of differential expression analysis. Due to the inherent heterogeneity, the transcriptome changes may only partially reflect the dysregulation of transcriptional regulatory

processes associated with disease progression. Despite these limitations, the use of RNA-seq for transcriptome profiling remains a valuable method for mapping and revealing gene expression patterns underlying changes in RV myocardial structure and function during the pathologic cardiac remodeling process, such as RV remodeling in PAH.

Although a strong correlation between mRNA expression and protein content of ECM molecules was observed in RV tissues by either analyzing publicly available proteomic data or performing Western blot analysis, a proteomic assay may provide more valuable insights on this topic. However, the low occurrence of gene-protein correlations observed when combining proteome and transcriptome datasets may not only be attributed to post-translational regulatory mechanisms, but also to the insufficient coverage and sensitivity of proteomic techniques, as there are several limitations with current proteomic platforms, especially with respect to ECM components in cardiac tissue[265]. Similarly, the use of the O-link panel for biomarker screening could limit the exploratory aspect, especially compared to the number of differentially regulated genes in the RV[266]. We anticipate that future efforts to further develop the technological aspects of clinical plasma proteomics will focus primarily on improving specificity, sensitivity and the number of proteins measured. Furthermore, additional investigations using cell-specific techniques such as single-cell sequencing methods[235,267] will be critical to elucidate the stage-specific molecular transitions within the regulatory landscape that contribute to RV dysfunction associated with various cardiopulmonary diseases.

6. FUTURE OUTLOOK

6.1 Comprehensive definition of early and late RV decompensation

Our results indicate the presence of distinct subphenotypes within both the compensated and decompensated RV states in PAH, suggesting that molecular features defined by specific signaling pathways and genes go beyond the current clinical classification of RV function. Currently, RVEF, CO, PA coupling ratio and TAPSE serve as benchmarks for the assessment of RV function. However, more comprehensive clinical assessment is needed to accurately identify and classify patients in the spectrum of early to late stages of adaptive and maladaptive hypertrophy. A future framework should integrate advanced imaging techniques and molecular diagnostics to increase sensitivity. This will be possible through rigorous studies in different PAH cohorts spanning different stages of RV disease progression.

6.2 Validation and functional assessment of the proposed biomarkers

In this research, we proposed a panel of five RV-associated biomarkers and demonstrated their potential to discriminate different RV states in PAH patients and their association with clinical outcomes. While we have validated their changes in RV protein levels in the MCT animal model, the next step is to verify these proteins in human RV tissue to determine their suitability as RV-specific prognostic markers.

At the level of circulating biomarkers, we were able to demonstrate that biomarkers change in PAH patients with different RV stages using two independent cohorts. However, further validations and functional assessments will be essential steps to propose them as relative PAH-RV associated biomarkers as well as therapeutic targets. Validation of RV-specific biomarkers should be performed at two levels: First, protein expression and alterations of NID1, C1QTNF1, CRTAC1, MEGF9 and SPARCL1 should be validated in plasma samples from an independent cohort using ELISA assays. Subsequently, the evaluation should be extended to other PAH plasma cohorts that may not have used the Olink platform for protein quantification to confirm changes at different stages of the disease. In addition, it is critical to investigate the functional impact of decompensated RV at early and late stages in a separate PAH cohort, in correlation with the identified panel of five proteins. (This will be performed in collaboration with UKGM clinicians and cardiologists to confirm the clinical relevance of the biomarkers)

6.3 Functional assessments of ECM targets

We identified ECM remodeling as a key factor in the transition from adaptive to maladaptive RV hypertrophy and validated 18 targets (13 genes + 5 biomarkers) related to cell adhesion and ECM through our integrative analysis. These specific candidates associated with different stages of RV hypertrophy in PAH should be further functionally investigated in the future by targeted gene knockdown (KD) or overexpression experiments in vitro, especially in fibroblasts and cardiomyocytes, as well as in vivo in animal models of PH-RV dysfunction, such as PAB.

6.4 Fatty acid metabolism and role of estrogen response

We found that fatty acid metabolism, especially fatty acid oxidation (FAO) and mitochondrial transport (by carnitine shuttle), are among the most dysregulated metabolic pathways in early decompensated RV. Although impaired FAO has previously been associated with RV maladaptation in PAH[78,211], it remains unclear whether the accumulation of fatty acids in cardiomyocytes causes the maladaptive remodeling or whether it occurs as a consequence of upstream enzyme or transporter dysfunction. The following experiments could be performed to clarify this aspect:

1. Expose neonatal cardiomyocytes or cell lines with altered carnitine transporter gene expression to stretch or hypoxia to simulate pressure overload. Assess hypertrophy, viability, apoptosis, expression of hypertrophy and FAO markers, and ATP production over time to investigate the relationship between hypertrophy and FAO.
2. Subject mice or rats with altered (overexpression or KD) carnitine transporter gene expression (or other FAO enzymes) to PAB. Investigate RV function and hypertrophy by imaging, histologic analysis, and molecular analysis of FAO-related protein expression to confirm the relationship between FAO and hypertrophy in vivo.
3. Exploring metabolic modulation in the treatment of RV hypertrophy using preclinical models. After the establishment of RV hypertrophy by PAB, FAO-modulating agents (such as PPAR agonists or carnitine supplements) should be administered and the effects on RV function, structure and metabolic state should be evaluated by imaging and histologic studies.

Furthermore, our results suggest that the protective mechanism against decompensated RV conditions in women depends primarily on estrogen-mediated responses and fatty acid

metabolism. Measurement of estrogen-related metabolites and proteins in the above experiments will elucidate the potential role of the upstream estrogen response in RV remodeling.

6.5 Single nuclei multiomics to uncover the heterogeneity of RV remodeling

As mentioned above, there is an urgent need to extend multimodal omics technology to further investigate the underlying heterogeneity of the RV, not only in the context of PAH-associated RV remodeling, but also in other cardiovascular pathologies that lead to abnormal states of the RV. An important step in this direction is a comprehensive single-cell transcriptome analysis of MCT-induced RV hypertrophy to uncover the cell type-specific changes associated with the transition from adaptive to maladaptive RV. An initial investigation of the cell type heterogeneity behind the RV hypertrophy response using a PH animal model that will provide insights into the cellular subtypes and composition at different time points of RV hypertrophy as it is performed in a controlled, time-dependent preclinical model.

Furthermore, multiomics deciphering of RV hypertrophy and RV failure using human RV data is essential. This will be achieved by integrating paired single-core RNA and chromatin accessibility data analyzes from compensated and decompensated RV samples in the context of PAH, which in turn will enable us to: 1. Identify the cell type-specific changes associated with the transition from adaptive to maladaptive RV, 2. Compare the cell type-specific transition from adaptive to maladaptive RV in humans with the MCT animal model data, 3. Identify the upstream promoters and enhancers and their differential activity associated with each RV state, and 4. Identify the different transcription factors that leave a footprint in different cell types and RV states.

Finally, the reconstruction and analysis of a stage-specific enhancer-based gene regulatory network (eGRN) of RV remodeling in PAH using single-cell multi-omics will allow us to identify the novel upstream regulatory elements associated with early stages of adaptive and maladaptive RV hypertrophy and with different cell types involved in RV.

7. SUMMARY

The functionality of the right ventricle (RV) has a significant impact on prognosis and functional outcome in patients with pulmonary hypertension (PH). However, our knowledge of RV remodeling and its molecular properties under different disease conditions such as PH is limited. Therefore, the aim of this study is to describe the molecular profile of adaptive and maladaptive right ventricular remodeling and dysfunction in PH.

To achieve this goal, we adopted an integrative analysis approach using transcriptomics and proteomics in humans as well as different animal models of PH with RV dysfunction. First, we performed a comparative analysis of two animal models (MCT and PAB). Using an unsupervised clustering approach, we identified different subgroups within the decompensated RV states and described the "early" to "late" maladaptive RV transition, a classification that was largely confirmed by the hemodynamic measurements. In addition, we generated RNA-seq data from RV tissue of 40 patients clinically categorized as adaptive and maladaptive RV hypertrophy and identified distinct subgroups of compensated and decompensated RV by their distinct molecular phenotype through a similar analytical approach. Our integrative analysis revealed that extracellular matrix remodeling together with a strong downregulation of fatty acid β-oxidation characterizes the early decompensation phase of RV, while several estrogen-related signaling pathways are associated with the sex-specific differences in RV adaptation. Next, we integrated the RV transcriptome with an independent plasma proteome cohort to assess the circulating levels of our targets. We then validated our final candidates in a second independent cohort of pulmonary arterial hypertension (PAH) patients and introduced a panel of five ECM-related proteins that could significantly classify patients with compensated or decompensated RV. In particular, NID1 and C1QTNF1 were found to be particularly significant in predicting early and late decompensated RV state, while correlating with functional parameters and clinical outcomes, demonstrated their potential as prognostic biomarkers for PAH-associated RV dysfunction.

Altogether, our study uncovered novel subgroups of human RV remodeling beyond clinical measurements, while the combination with proteomic analysis revealed five potential RV-specific biomarkers for PAH. Furthermore, highlighting the molecular phenotype of the early and late subgroups of maladaptive RV provides new potential therapeutic targets for RV dysfunction to intervene in the transition from compensation to decompensation, thereby enhancing survival and quality of life in PAH.

8. ZUSAMMENFASSUNG

Die Funktionalität des rechten Ventrikels (RV) spielt eine entscheidende Rolle bei der Prognose und dem funktionellen Ergebnis von Patienten mit pulmonaler Hypertonie (PH). Trotzdem ist unser Verständnis über den Umbau des rechten Ventrikels und seine molekularen Eigenschaften unter verschiedenen Krankheitsbedingungen wie der PH begrenzt. Das Ziel dieser Studie war es, das molekulare Profil des adaptiven und maladaptiven rechtsventrikulären Remodellings und der Dysfunktion bei PH zu charakterisieren.

Um dieses Ziel zu erreichen, wurde ein integrativer Analyseansatz gewählt, der Transkriptomik und Proteomik beim Menschen sowie bei verschiedenen Tiermodellen von PH mit RV-Dysfunktion kombinierteZunächst wurde eine vergleichende Analyse von zwei Tiermodellen (MCT und PAB) durchgeführt. Durch einen unüberwachten Clustering-Ansatz konnten verschiedene Untergruppen innerhalb der dekompensierten RV-Zustände identifiziert werden, wobei der "frühe" bis "späte" maladaptive RV-Übergang beschrieben wurde, was durch hämodynamische Messungen bestätigt wurde. RNA-seq-Daten aus RV-Gewebe von 40 Patienten wurden generiert, die klinisch als adaptive und maladaptive RV-Hypertrophie eingestuft wurden. Verschiedene Untergruppen kompensierter und dekompensierter RV wurden anhand ihres unterschiedlichen molekularen Phänotyps identifiziert. Die integrative Analyse zeigte, dass der Umbau der extrazellulären Matrix zusammen mit einer starken Herabregulierung der Fettsäure-β-Oxidation die frühe Dekompensationsphase des RV charakterisiert. Zudem wurden mehrere östrogenbezogene Signalwege mit geschlechtsspezifischen Unterschieden in der RV-Anpassung in Verbindung gebracht. Das RV-Transkriptom wurde mit einer unabhängigen Plasmaproteom-Kohorte integriert, um die zirkulierenden Konzentrationen zu bewerten. Anschließend validierten wir unsere endgültigen Kandidaten in einer zweiten unabhängigen Kohorte von Patienten mit pulmonaler arterieller Hypertonie (PAH), PH der Gruppe 1, und stellten eine Gruppe von fünf ECM-bezogenen Proteinen vor, die Patienten mit kompensierter oder dekompensierter RV signifikant klassifizieren konnten. Insbesondere NID1 und C1QTNF1 erwiesen sich als besonders aussagekräftig bei der Vorhersage des frühen und späten dekompensierten RV-Zustands, während sie mit funktionellen Parametern und klinischen Ergebnissen korrelierten, was ihr Potenzial als prognostische Biomarker für PAH-assoziierte RV-Dysfunktion belegt.

Insgesamt wurden in unserer Studie neue Untergruppen des menschlichen RV-Remodellings aufgedeckt, die über klinische Messungen hinausgehen, während die Kombination mit der Proteomanalyse fünf potenzielle RV-spezifische Biomarker für PAH ergab. Darüber hinaus bietet die Hervorhebung des molekularen Phänotyps der frühen und späten Untergruppen der maladaptiven RV-Dysfunktion neue potenzielle therapeutische Ziele für die RV-Dysfunktion, um in den Übergang von der Kompensation zur Dekompensation einzugreifen und so das Überleben und die Lebensqualität bei PAH zu verbessern.

9. REFERENCES

1. Mocumbi, A. *et al.* Pulmonary hypertension. *Nat. Rev. Dis. Primer* **10**, 1 (2024).
2. Humbert, M. *et al.* 2022 ESC/ERS Guidelines for the diagnosis and treatment of pulmonary hypertension. *Eur. Respir. J.* **61**, 2200879 (2023).
3. Corris, P. A. & Seeger, W. Call it by the correct name—pulmonary hypertension not pulmonary arterial hypertension: growing recognition of the global health impact for a well-recognized condition and the role of the Pulmonary Vascular Research Institute. *Am. J. Physiol.-Lung Cell. Mol. Physiol.* **318**, L992–L994 (2020).
4. Rose-Jones, L. & Mclaughlin, V. Pulmonary Hypertension: Types and Treatments. *Curr. Cardiol. Rev.* **11**, 73–79 (2014).
5. Simonneau, G. *et al.* Updated Clinical Classification of Pulmonary Hypertension. *J. Am. Coll. Cardiol.* **62**, D34–D41 (2013).
6. Thomson, J. R. Sporadic primary pulmonary hypertension is associated with germline mutations of the gene encoding BMPR-II, a receptor member of the TGF-beta family. *J. Med. Genet.* **37**, 741–745 (2000).
7. Trembath, R. C. *et al.* Clinical and Molecular Genetic Features of Pulmonary Hypertension in Patients with Hereditary Hemorrhagic Telangiectasia. *N. Engl. J. Med.* **345**, 325–334 (2001).
8. Souza, R. *et al.* Pulmonary arterial hypertension associated with fenfluramine exposure: report of 109 cases. *Eur. Respir. J.* **31**, 343–348 (2008).
9. Chin, K. M., Channick, R. N. & Rubin, L. J. Is Methamphetamine Use Associated With Idiopathic Pulmonary Arterial Hypertension? *Chest* **130**, 1657–1663 (2006).
10. De Groote, P. *et al.* Evaluation of cardiac abnormalities by Doppler echocardiography in a large nationwide multicentric cohort of patients with systemic sclerosis. *Ann. Rheum. Dis.* **67**, 31–36 (2008).
11. Sitbon, O. *et al.* Prevalence of HIV-related Pulmonary Arterial Hypertension in the Current Antiretroviral Therapy Era. *Am. J. Respir. Crit. Care Med.* **177**, 108–113 (2008).
12. Krowka, M. J., Swanson, K. L., Frantz, R. P., McGoon, M. D. & Wiesner, R. H. Portopulmonary hypertension: Results from a 10-year screening algorithm. *Hepatology* **44**, 1502–1510 (2006).
13. Besterman, E. ATRIAL SEPTAL DEFECT WITH PULMONARY HYPERTENSION. *Heart* **23**, 587–598 (1961).
14. Lapa, M. *et al.* Cardiopulmonary Manifestations of Hepatosplenic Schistosomiasis. *Circulation* **119**, 1518–1523 (2009).
15. Gladwin, M. T. *et al.* Pulmonary Hypertension as a Risk Factor for Death in Patients with Sickle Cell Disease. *N. Engl. J. Med.* **350**, 886–895 (2004).
16. Montani, D. *et al.* Pulmonary Veno-Occlusive Disease: Clinical, Functional, Radiologic, and Hemodynamic Characteristics and Outcome of 24 Cases Confirmed by Histology. *Medicine (Baltimore)* **87**, 220–233 (2008).
17. Ruopp, N. F. & Cockrill, B. A. Diagnosis and Treatment of Pulmonary Arterial Hypertension: A Review. *JAMA* **327**, 1379 (2022).
18. Benza, R. L. *et al.* An Evaluation of Long-term Survival From Time of Diagnosis in Pulmonary Arterial Hypertension From the REVEAL Registry. *Chest* **142**, 448–456 (2012).
19. Montani, D. *et al.* Pulmonary arterial hypertension. *Orphanet J. Rare Dis.* **8**, 97 (2013).
20. Benza, R. L. *et al.* Predicting Survival in Pulmonary Arterial Hypertension: Insights From the Registry to Evaluate Early and Long-Term Pulmonary Arterial Hypertension Disease Management (REVEAL). *Circulation* **122**, 164–172 (2010).
21. Humbert, M. *et al.* Pulmonary Arterial Hypertension in France: Results from a National Registry. *Am. J. Respir. Crit. Care Med.* **173**, 1023–1030 (2006).
22. Schermuly, R. T., Ghofrani, H. A., Wilkins, M. R. & Grimminger, F. Mechanisms of disease: pulmonary arterial hypertension. *Nat. Rev. Cardiol.* **8**, 443–455 (2011).
23. Gaine, S. & McLaughlin, V. Pulmonary arterial hypertension: tailoring treatment to risk in the current era. *Eur. Respir. Rev.* **26**, 170095 (2017).
24. Toma, M. *et al.* Left Heart Disease Phenotype in Elderly Patients with Pulmonary Arterial Hypertension: Insights from the Italian PATRIARCA Registry. *J. Clin. Med.* **11**, 7136 (2022).
25. Sarzyńska, K. *et al.* Quality of life of patients with pulmonary arterial hypertension: a meta-analysis. *Eur. Rev. Med. Pharmacol. Sci.* **25**, 4983–4998 (2021).
26. Brown, L. M. *et al.* Delay in Recognition of Pulmonary Arterial Hypertension. *Chest* **140**, 19–26 (2011).
27. Vonk Noordegraaf, A. & Galie, N. The role of the right ventricle in pulmonary arterial hypertension. *Eur. Respir. Rev.* **20**, 243–253 (2011).

28. Eichstaedt, C. A. *et al.* Genetic counselling and testing in pulmonary arterial hypertension: a consensus statement on behalf of the International Consortium for Genetic Studies in PAH. *Eur. Respir. J.* **61**, 2201471 (2023).
29. Kim, G. H., Ryan, J. J., Marsboom, G. & Archer, S. L. Epigenetic Mechanisms of Pulmonary Hypertension. *Pulm. Circ.* **1**, 347–356 (2011).
30. Bonnet, S. *et al.* Clinical value of non-coding RNAs in cardiovascular, pulmonary, and muscle diseases. *Am. J. Physiol.-Cell Physiol.* **318**, C1–C28 (2020).
31. Wharton, J. *et al.* Antiproliferative Effects of Phosphodiesterase Type 5 Inhibition in Human Pulmonary Artery Cells. *Am. J. Respir. Crit. Care Med.* **172**, 105–113 (2005).
32. Christman, B. W. *et al.* An Imbalance between the Excretion of Thromboxane and Prostacyclin Metabolites in Pulmonary Hypertension. *N. Engl. J. Med.* **327**, 70–75 (1992).
33. Davie, N. *et al.* ET $_{A}$ and ET $_{B}$ Receptors Modulate the Proliferation of Human Pulmonary Artery Smooth Muscle Cells. *Am. J. Respir. Crit. Care Med.* **165**, 398–405 (2002).
34. Tabima, D. M. & Chesler, N. C. The effects of vasoactivity and hypoxic pulmonary hypertension on extralobar pulmonary artery biomechanics. *J. Biomech.* **43**, 1864–1869 (2010).
35. Tuder, R. M. *et al.* Expression of angiogenesis-related molecules in plexiform lesions in severe pulmonary hypertension: evidence for a process of disordered angiogenesis. *J. Pathol.* **195**, 367–374 (2001).
36. Tuder, R. M., Groves, B., Badesch, D. B. & Voelkel, N. F. Exuberant endothelial cell growth and elements of inflammation are present in plexiform lesions of pulmonary hypertension. *Am. J. Pathol.* **144**, 275–285 (1994).
37. Pullamsetti, S. S. *et al.* Inflammation, immunological reaction and role of infection in pulmonary hypertension. *Clin. Microbiol. Infect.* **17**, 7–14 (2011).
38. Xu, W. *et al.* Alterations of cellular bioenergetics in pulmonary artery endothelial cells. *Proc. Natl. Acad. Sci.* **104**, 1342–1347 (2007).
39. Tournier, A. *et al.* Calibrated automated thrombography demonstrates hypercoagulability in patients with idiopathic pulmonary arterial hypertension. *Thromb. Res.* **126**, e418–e422 (2010).
40. Oikawa, M. *et al.* Increased [18F]Fluorodeoxyglucose Accumulation in Right Ventricular Free Wall in Patients With Pulmonary Hypertension and the Effect of Epoprostenol. *J. Am. Coll. Cardiol.* **45**, 1849–1855 (2005).
41. Bogaard, H. J., Abe, K., Vonk Noordegraaf, A. & Voelkel, N. F. The Right Ventricle Under Pressure. *Chest* **135**, 794–804 (2009).
42. Pokreisz, P., Marsboom, G. & Janssens, S. Pressure overload-induced right ventricular dysfunction and remodelling in experimental pulmonary hypertension: the right heart revisited. *Eur. Heart J. Suppl.* **9**, H75–H84 (2007).
43. Badagliacca, R. *et al.* Prognostic relevance of right heart reverse remodeling in idiopathic pulmonary arterial hypertension. *J. Heart Lung Transplant.* **37**, 195–205 (2018).
44. Greyson, C. R. The Right Ventricle and Pulmonary Circulation: Basic Concepts. *Rev. Esp. Cardiol. Engl. Ed.* **63**, 81–95 (2010).
45. Brimioulle, S. Effects of low flow on pulmonary vascular flow–pressure curves and pulmonary vascular impedance. *Cardiovasc. Res.* **42**, 183–192 (1999).
46. Buckberg, G. D. The ventricular septum: the lion of right ventricular function, and its impact on right ventricular restoration☆. *Eur. J. Cardiothorac. Surg.* **29**, S272–S278 (2006).
47. Dell'Italia, L. J. The right ventricle: anatomy, physiology, and clinical importance. *Curr. Probl. Cardiol.* **16**, 658–720 (1991).
48. Ho, S. Y. Anatomy, echocardiography, and normal right ventricular dimensions. *Heart* **92**, i2–i13 (2006).
49. Sakuma, M. *et al.* Right Ventricular Ejection Function Assessed by Cineangiography. Importance of Bellows Action.: Importance of Bellows Action. *Circ. J.* **66**, 605–609 (2002).
50. Santamore, W. P. & Amoore, J. N. Buffering of respiratory variations in venous return by right ventricle: a theoretical analysis. *Am. J. Physiol.-Heart Circ. Physiol.* **267**, H2163–H2170 (1994).
51. Zehender, M. *et al.* Right Ventricular Infarction as an Independent Predictor of Prognosis after Acute Inferior Myocardial Infarction. *N. Engl. J. Med.* **328**, 981–988 (1993).
52. Rouleau, J. L., Paradis, P., Shenasa, H. & Juneau, C. Faster time to peak tension and velocity of shortening in right versus left ventricular trabeculae and papillary muscles of dogs. *Circ. Res.* **59**, 556–561 (1986).
53. Kret, M. & Arora, R. Pathophysiological Basis of Right Ventricular Remodeling. *J. Cardiovasc. Pharmacol. Ther.* **12**, 5–14 (2007).
54. Roncon-Albuquerque, R. *et al.* Acute changes of biventricular gene expression in volume and right ventricular pressure overload. *Life Sci.* **78**, 2633–2642 (2006).

55. Faber, M. J. *et al.* Time dependent changes in cytoplasmic proteins of the right ventricle during prolonged pressure overload. *J. Mol. Cell. Cardiol.* **43**, 197–209 (2007).
56. Zagorski, J., Sanapareddy, N., Gellar, M. A., Kline, J. A. & Watts, J. A. Transcriptional profile of right ventricular tissue during acute pulmonary embolism in rats. *Physiol. Genomics* **34**, 101–111 (2008).
57. Davlouros, P. A. The right ventricle in congenital heart disease. *Heart* **92**, i27–i38 (2006).
58. Belenkie, I., Dani, R., Smith, E. R. & Tyberg, J. V. Effects of volume loading during experimental acute pulmonary embolism. *Circulation* **80**, 178–188 (1989).
59. Konstam, M. A. *et al.* Evaluation and Management of Right-Sided Heart Failure: A Scientific Statement From the American Heart Association. *Circulation* **137**, (2018).
60. Keranov, S. *et al.* CILP1 as a biomarker for right ventricular maladaptation in pulmonary hypertension. *Eur. Respir. J.* **57**, 1901192 (2021).
61. Van Der Bruggen, C. E. E., Tedford, R. J., Handoko, M. L., Van Der Velden, J. & De Man, F. S. RV pressure overload: from hypertrophy to failure. *Cardiovasc. Res.* **113**, 1423–1432 (2017).
62. Vonk-Noordegraaf, A. *et al.* Right Heart Adaptation to Pulmonary Arterial Hypertension. *J. Am. Coll. Cardiol.* **62**, D22–D33 (2013).
63. Haddad, F., Hunt, S. A., Rosenthal, D. N. & Murphy, D. J. Right Ventricular Function in Cardiovascular Disease, Part I: Anatomy, Physiology, Aging, and Functional Assessment of the Right Ventricle. *Circulation* **117**, 1436–1448 (2008).
64. Haddad, F., Doyle, R., Murphy, D. J. & Hunt, S. A. Right Ventricular Function in Cardiovascular Disease, Part II: Pathophysiology, Clinical Importance, and Management of Right Ventricular Failure. *Circulation* **117**, 1717–1731 (2008).
65. Dong, Y. *et al.* Right ventricular septomarginal trabeculation hypertrophy is associated with disease severity in patients with pulmonary arterial hypertension. *Int. J. Cardiovasc. Imaging* **34**, 1439–1449 (2018).
66. Fang, Y.-H. *et al.* Therapeutic inhibition of fatty acid oxidation in right ventricular hypertrophy: exploiting Randle's cycle. *J. Mol. Med.* **90**, 31–43 (2012).
67. Cavasin, M. A. *et al.* Selective Class I Histone Deacetylase Inhibition Suppresses Hypoxia-Induced Cardiopulmonary Remodeling Through an Antiproliferative Mechanism. *Circ. Res.* **110**, 739–748 (2012).
68. Zhao, L. *et al.* Histone Deacetylation Inhibition in Pulmonary Hypertension: Therapeutic Potential of Valproic Acid and Suberoylanilide Hydroxamic Acid. *Circulation* **126**, 455–467 (2012).
69. Ryan, J. J. & Archer, S. L. The Right Ventricle in Pulmonary Arterial Hypertension: Disorders of Metabolism, Angiogenesis and Adrenergic Signaling in Right Ventricular Failure. *Circ. Res.* **115**, 176–188 (2014).
70. Ryan, J. J. *et al.* Right Ventricular Adaptation and Failure in Pulmonary Arterial Hypertension. *Can. J. Cardiol.* **31**, 391–406 (2015).
71. Rich, S. *et al.* Long-term Effects of Epoprostenol on the Pulmonary Vasculature in Idiopathic Pulmonary Arterial Hypertension. *Chest* **138**, 1234–1239 (2010).
72. Jacobs, W. *et al.* The Right Ventricle Explains Sex Differences in Survival in Idiopathic Pulmonary Arterial Hypertension. *Chest* **145**, 1230–1236 (2014).
73. Keen, J., Prisco, S. & Prins, K. Sex Differences in Right Ventricular Dysfunction: Insights From the Bench to Bedside. *Front. Physiol.* **11**, (2021).
74. Al-Qazazi, R. *et al.* Macrophage–NLRP3 Activation Promotes Right Ventricle Failure in Pulmonary Arterial Hypertension. *Am. J. Respir. Crit. Care Med.* **206**, 608–624 (2022).
75. Prins, K. W. *et al.* Interleukin-6 is independently associated with right ventricular function in pulmonary arterial hypertension. *J. Heart Lung Transplant.* **37**, 376–384 (2018).
76. Piao, L. *et al.* GRK2-Mediated Inhibition of Adrenergic and Dopaminergic Signaling in Right Ventricular Hypertrophy: Therapeutic Implications in Pulmonary Hypertension. *Circulation* **126**, 2859–2869 (2012).
77. Tian, L. *et al.* Epigenetic Metabolic Reprogramming of Right Ventricular Fibroblasts in Pulmonary Arterial Hypertension: A Pyruvate Dehydrogenase Kinase-Dependent Shift in Mitochondrial Metabolism Promotes Right Ventricular Fibrosis. *Circ. Res.* **126**, 1723–1745 (2020).
78. Brittain, E. L. *et al.* Fatty Acid Metabolic Defects and Right Ventricular Lipotoxicity in Human Pulmonary Arterial Hypertension. *Circulation* **133**, 1936–1944 (2016).
79. Bonnet, S. *et al.* An Abnormal Mitochondrial–Hypoxia Inducible Factor-1α–Kv Channel Pathway Disrupts Oxygen Sensing and Triggers Pulmonary Arterial Hypertension in Fawn Hooded Rats: Similarities to Human Pulmonary Arterial Hypertension. *Circulation* **113**, 2630–2641 (2006).
80. Ruiter, G. *et al.* Right ventricular oxygen supply parameters are decreased in human and experimental pulmonary hypertension. *J. Heart Lung Transplant.* **32**, 231–240 (2013).
81. Michaels, A. D., Chatterjee, K. & De Marco, T. Effects of Intravenous Nesiritide on Pulmonary Vascular Hemodynamics in Pulmonary Hypertension. *J. Card. Fail.* **11**, 425–431 (2005).

82. Klinger, J. R. *et al.* Pulmonary Hemodynamic Responses to Brain Natriuretic Peptide and Sildenafil in Patients With Pulmonary Arterial Hypertension. *Chest* **129**, 417–425 (2006).
83. Rain, S. *et al.* Right Ventricular Diastolic Impairment in Patients With Pulmonary Arterial Hypertension. *Circulation* **128**, 2016–2025 (2013).
84. Llucià-Valldeperas, A., De Man, F. S. & Bogaard, H. J. Adaptation and Maladaptation of the Right Ventricle in Pulmonary Vascular Diseases. *Clin. Chest Med.* **42**, 179–194 (2021).
85. Bogaard, H. J. *et al.* Chronic Pulmonary Artery Pressure Elevation Is Insufficient to Explain Right Heart Failure. *Circulation* **120**, 1951–1960 (2009).
86. Hessel, M., Steendijk, P., Den Adel, B., Schutte, C. & Van Der Laarse, A. Pressure Overload-induced Right Ventricular Failure is Associated with Re-expression of Myocardial Tenascin-C and Elevated Plasma Tenascin-C Levels. *Cell. Physiol. Biochem.* **24**, 201–210 (2009).
87. Ventetuolo, C. E. *et al.* Baseline Sex Differences in Pulmonary Arterial Hypertension Randomized Clinical Trials. *Ann. Am. Thorac. Soc.* **20**, 58–66 (2023).
88. Tello, K. *et al.* Sex Differences in Right Ventricular–Pulmonary Arterial Coupling in Pulmonary Arterial Hypertension. *Am. J. Respir. Crit. Care Med.* **202**, 1042–1046 (2020).
89. Mathai, S. C., Hassoun, P. M., Puhan, M. A., Zhou, Y. & Wise, R. A. Sex Differences in Response to Tadalafil in Pulmonary Arterial Hypertension. *Chest* **147**, 188–197 (2015).
90. Gabler, N. B. *et al.* Race and Sex Differences in Response to Endothelin Receptor Antagonists for Pulmonary Arterial Hypertension. *Chest* **141**, 20–26 (2012).
91. Dignam, J. P., Sharma, S., Stasinopoulos, I. & MacLean, M. R. Pulmonary arterial hypertension: Sex matters. *Br. J. Pharmacol.* bph.16277 (2024) doi:10.1111/bph.16277.
92. Frump, A. L. *et al.* Estradiol improves right ventricular function in rats with severe angioproliferative pulmonary hypertension: effects of endogenous and exogenous sex hormones. *Am. J. Physiol.-Lung Cell. Mol. Physiol.* **308**, L873–L890 (2015).
93. Wang, Y.-D. *et al.* 17β-estradiol preserves right ventricular function in rats with pulmonary arterial hypertension: an echocardiographic and histochemical study. *Int. J. Cardiovasc. Imaging* **35**, 441–450 (2019).
94. Yuan, P. *et al.* Oestradiol ameliorates monocrotaline pulmonary hypertension *via* NO, prostacyclin and endothelin-1 pathways. *Eur. Respir. J.* **41**, 1116–1125 (2013).
95. Umar, S. *et al.* Estrogen Rescues Preexisting Severe Pulmonary Hypertension in Rats. *Am. J. Respir. Crit. Care Med.* **184**, 715–723 (2011).
96. Cheng, T.-C. *et al.* Estrogen receptor-α prevents right ventricular diastolic dysfunction and fibrosis in female rats. *Am. J. Physiol.-Heart Circ. Physiol.* **319**, H1459–H1473 (2020).
97. Hemnes, A. R. *et al.* Testosterone Negatively Regulates Right Ventricular Load Stress Responses in Mice. *Pulm. Circ.* **2**, 352–358 (2012).
98. Wen, J. *et al.* DHT deteriorates the progression of monocrotaline-induced pulmonary arterial hypertension: effects of endogenous and exogenous androgen. *Am. J. Transl. Res.* **11**, 5752–5763 (2019).
99. Rodriguez-Arias, J. J. & García-Álvarez, A. Sex Differences in Pulmonary Hypertension. *Front. Aging* **2**, 727558 (2021).
100. Shapiro, S. *et al.* Sex Differences in the Diagnosis, Treatment, and Outcome of Patients With Pulmonary Arterial Hypertension Enrolled in the Registry to Evaluate Early and Long-term Pulmonary Arterial Hypertension Disease Management. *Chest* **141**, 363–373 (2012).
101. Ventetuolo, C. E. *et al.* Sex Hormones Are Associated with Right Ventricular Structure and Function: The MESA-Right Ventricle Study. *Am. J. Respir. Crit. Care Med.* **183**, 659–667 (2011).
102. Liu, A. *et al.* Estrogen maintains mitochondrial content and function in the right ventricle of rats with pulmonary hypertension. *Physiol. Rep.* **5**, e13157 (2017).
103. Sun, Y. *et al.* Sex Differences, Estrogen Metabolism and Signaling in the Development of Pulmonary Arterial Hypertension. *Front. Cardiovasc. Med.* **8**, 719058 (2021).
104. Pedram, A., Razandi, M., O'Mahony, F., Lubahn, D. & Levin, E. R. Estrogen Receptor-β Prevents Cardiac Fibrosis. *Mol. Endocrinol.* **24**, 2152–2165 (2010).
105. Babiker, F. A. *et al.* 17β-Estradiol Antagonizes Cardiomyocyte Hypertrophy by Autocrine/Paracrine Stimulation of a Guanylyl Cyclase A Receptor-Cyclic Guanosine Monophosphate-Dependent Protein Kinase Pathway. *Circulation* **109**, 269–276 (2004).
106. Sun, J. *et al.* Hypercontractile Female Hearts Exhibit Increased *S* -Nitrosylation of the L-Type Ca^{2+} Channel α1 Subunit and Reduced Ischemia/Reperfusion Injury. *Circ. Res.* **98**, 403–411 (2006).
107. Pedram, A. *et al.* Estrogen Inhibits Cardiac Hypertrophy: Role of Estrogen Receptor-β to Inhibit Calcineurin. *Endocrinology* **149**, 3361–3369 (2008).
108. Wang, M. *et al.* Estrogen receptor β mediates increased activation of PI3K/Akt signaling and improved myocardial function in female hearts following acute ischemia. *Am. J. Physiol.-Regul. Integr. Comp. Physiol.* **296**, R972–R978 (2009).

109. Lahm, T. *et al.* 17β-Estradiol mediates superior adaptation of right ventricular function to acute strenuous exercise in female rats with severe pulmonary hypertension. *Am. J. Physiol.-Lung Cell. Mol. Physiol.* **311**, L375–L388 (2016).
110. Dworatzek, E. *et al.* Sex-specific regulation of collagen I and III expression by 17β-Estradiol in cardiac fibroblasts: role of estrogen receptors. *Cardiovasc. Res.* **115**, 315–327 (2019).
111. Voloshenyuk, T. G. & Gardner, J. D. Estrogen improves TIMP-MMP balance and collagen distribution in volume-overloaded hearts of ovariectomized females. *Am. J. Physiol.-Regul. Integr. Comp. Physiol.* **299**, R683–R693 (2010).
112. Nadadur, R. D. *et al.* Reverse right ventricular structural and extracellular matrix remodeling by estrogen in severe pulmonary hypertension. *J. Appl. Physiol.* **113**, 149–158 (2012).
113. Ambade, A. S., Hassoun, P. M. & Damico, R. L. Basement Membrane Extracellular Matrix Proteins in Pulmonary Vascular and Right Ventricular Remodeling in Pulmonary Hypertension. *Am. J. Respir. Cell Mol. Biol.* **65**, 245–258 (2021).
114. Golob, M. J., Wang, Z., Prostrollo, A. J., Hacker, T. A. & Chesler, N. C. Limiting collagen turnover via collagenase-resistance attenuates right ventricular dysfunction and fibrosis in pulmonary arterial hypertension. *Physiol. Rep.* **4**, e12815 (2016).
115. Borgdorff, M. A., Bartelds, B., Dickinson, M. G., Steendijk, P. & Berger, R. M. F. A cornerstone of heart failure treatment is not effective in experimental right ventricular failure. *Int. J. Cardiol.* **169**, 183–189 (2013).
116. Cheng, T.-C., Philip, J. L., Tabima, D. M., Hacker, T. A. & Chesler, N. C. Multiscale structure-function relationships in right ventricular failure due to pressure overload. *Am. J. Physiol.-Heart Circ. Physiol.* **315**, H699–H708 (2018).
117. Stroud, J. D., Baicu, C. F., Barnes, M. A., Spinale, F. G. & Zile, M. R. Viscoelastic properties of pressure overload hypertrophied myocardium: effect of serine protease treatment. *Am. J. Physiol.-Heart Circ. Physiol.* **282**, H2324–H2335 (2002).
118. Lyon, R. C., Zanella, F., Omens, J. H. & Sheikh, F. Mechanotransduction in Cardiac Hypertrophy and Failure. *Circ. Res.* **116**, 1462–1476 (2015).
119. Hill, M. R. *et al.* Structural and Mechanical Adaptations of Right Ventricle Free Wall Myocardium to Pressure Overload. *Ann. Biomed. Eng.* **42**, 2451–2465 (2014).
120. Sharifi Kia, D., Fortunato, R., Maiti, S., Simon, M. A. & Kim, K. An exploratory assessment of stretch-induced transmural myocardial fiber kinematics in right ventricular pressure overload. *Sci. Rep.* **11**, 3587 (2021).
121. Sharifi Kia, D., Kim, K. & Simon, M. A. Current Understanding of the Right Ventricle Structure and Function in Pulmonary Arterial Hypertension. *Front. Physiol.* **12**, 641310 (2021).
122. Thenappan, T., Chan, S. Y. & Weir, E. K. Role of extracellular matrix in the pathogenesis of pulmonary arterial hypertension. *Am. J. Physiol.-Heart Circ. Physiol.* **315**, H1322–H1331 (2018).
123. Marcus, J. T. *et al.* Vena cava backflow and right ventricular stiffness in pulmonary arterial hypertension. *Eur. Respir. J.* **54**, 1900625 (2019).
124. Rosenkranz, S. *et al.* Left ventricular heart failure and pulmonary hypertension. *Eur. Heart J.* **37**, 942–954 (2016).
125. Hsu, S. *et al.* Right Ventricular Myofilament Functional Differences in Humans With Systemic Sclerosis–Associated Versus Idiopathic Pulmonary Arterial Hypertension. *Circulation* **137**, 2360–2370 (2018).
126. Rain, S. *et al.* Protein Changes Contributing to Right Ventricular Cardiomyocyte Diastolic Dysfunction in Pulmonary Arterial Hypertension. *J. Am. Heart Assoc.* **3**, e000716 (2014).
127. Safdar, Z. *et al.* Circulating Collagen Biomarkers as Indicators of Disease Severity in Pulmonary Arterial Hypertension. *JACC Heart Fail.* **2**, 412–421 (2014).
128. Andersen, S., Nielsen-Kudsk, J. E., Vonk Noordegraaf, A. & De Man, F. S. Right Ventricular Fibrosis: A Pathophysiological Factor in Pulmonary Hypertension? *Circulation* **139**, 269–285 (2019).
129. Polyakova, V., Hein, S., Kostin, S., Ziegelhoeffer, T. & Schaper, J. Matrix metalloproteinases and their tissue inhibitors in pressure-overloaded human myocardium during heart failure progression. *J. Am. Coll. Cardiol.* **44**, 1609–1618 (2004).
130. Kusakari, Y. *et al.* Impairment of Excitation-Contraction Coupling in Right Ventricular Hypertrophied Muscle with Fibrosis Induced by Pulmonary Artery Banding. *PLOS ONE* **12**, e0169564 (2017).
131. Trip, P. *et al.* Clinical relevance of right ventricular diastolic stiffness in pulmonary hypertension. *Eur. Respir. J.* **45**, 1603–1612 (2015).
132. Rain, S. *et al.* Right Ventricular Myocardial Stiffness in Experimental Pulmonary Arterial Hypertension: Relative Contribution of Fibrosis and Myofibril Stiffness. *Circ. Heart Fail.* **9**, e002636 (2016).
133. Bing, R. & Dweck, M. R. Myocardial fibrosis: why image, how to image and clinical implications. *Heart* **105**, 1832–1840 (2019).

134. Sarashina, T. *et al.* Reverse Right Ventricular Remodeling After Lung Transplantation in Patients With Pulmonary Arterial Hypertension Under Combination Therapy of Targeted Medical Drugs. *Circ. J.* **81**, 383–390 (2017).
135. Berman, M. *et al.* Right Ventricular Reverse Remodeling after Pulmonary Endarterectomy: Magnetic Resonance Imaging and Clinical and Right Heart Catheterization Assessment. *Pulm. Circ.* **4**, 36–44 (2014).
136. Fukui, S. *et al.* Right ventricular reverse remodelling after balloon pulmonary angioplasty. *Eur. Respir. J.* **43**, 1394–1402 (2014).
137. Katz, W. E. *et al.* Immediate effects of lung transplantation on right ventricular morphology and function in patients with variable degrees of pulmonary hypertension. *J. Am. Coll. Cardiol.* **27**, 384–391 (1996).
138. Tian, L. *et al.* Supra-coronary aortic banding improves right ventricular function in experimental pulmonary arterial hypertension in rats by increasing systolic right coronary artery perfusion. *Acta Physiol.* **229**, e13483 (2020).
139. Caputo, A. *et al.* Medical Management of Right Ventricular Dysfunction in Pulmonary Arterial Hypertension. *Curr. Heart Fail. Rep.* **20**, 263–270 (2023).
140. Leopold, J. A. & Hemnes, A. R. Integrative Omics to Characterize and Classify Pulmonary Vascular Disease. *Clin. Chest Med.* **42**, 195–205 (2021).
141. Rhodes, C. J., Sweatt, A. J. & Maron, B. A. Harnessing Big Data to Advance Treatment and Understanding of Pulmonary Hypertension. *Circ. Res.* **130**, 1423–1444 (2022).
142. Hemnes, A. R. Using Omics to Understand and Treat Pulmonary Vascular Disease. *Front. Med.* **5**, 157 (2018).
143. Campo, A. *et al.* Outcomes of hospitalisation for right heart failure in pulmonary arterial hypertension. *Eur. Respir. J.* **38**, 359–367 (2011).
144. Tello, K., Gall, H., Richter, M., Ghofrani, A. & Schermuly, R. Right ventricular function in pulmonary (arterial) hypertension. *Herz* **44**, 509–516 (2019).
145. Lopez-Crisosto, C. *et al.* Novel molecular insights and public omics data in pulmonary hypertension. *Biochim. Biophys. Acta BBA - Mol. Basis Dis.* **1867**, 166200 (2021).
146. Park, J. F. *et al.* Transcriptomic Analysis of Right Ventricular Remodeling in Two Rat Models of Pulmonary Hypertension: Identification and Validation of Epithelial-to-Mesenchymal Transition in Human Right Ventricular Failure. *Circ. Heart Fail.* **14**, e007058 (2021).
147. Qin, X. *et al.* Proteomic and Metabolomic Analyses of Right Ventricular Failure due to Pulmonary Arterial Hypertension. *Front. Mol. Biosci.* **9**, 834179 (2022).
148. Kobayashi, T. *et al.* Multi-omics analysis of right ventricles in rat models of pulmonary arterial hypertension: Consideration of mitochondrial biogenesis by chrysin. *Int. J. Mol. Med.* **49**, 69 (2022).
149. Mendelson, J. B. *et al.* Multi-omic and multispecies analysis of right ventricular dysfunction. *J. Heart Lung Transplant.* **43**, 303–313 (2024).
150. Hindmarch, C. C. T. *et al.* An integrated proteomic and transcriptomic signature of the failing right ventricle in monocrotaline induced pulmonary arterial hypertension in male rats. *Front. Physiol.* **13**, 966454 (2022).
151. Havlenova, T. *et al.* Right versus left ventricular remodeling in heart failure due to chronic volume overload. *Sci. Rep.* **11**, 17136 (2021).
152. Boucherat, O. *et al.* Identification of LTBP-2 as a plasma biomarker for right ventricular dysfunction in human pulmonary arterial hypertension. *Nat. Cardiovasc. Res.* **1**, 748–760 (2022).
153. Park, J. F., Liang, J. & Umar, S. Electrical Remodeling in Right Ventricular Failure Due to Pulmonary Hypertension: Unraveling Novel Therapeutic Targets. *Int. J. Mol. Sci.* **24**, 4633 (2023).
154. Janowski, A. M. *et al.* Advanced hemodynamic and cluster analysis for identifying novel RV function subphenotypes in patients with pulmonary hypertension. *J. Heart Lung Transplant.* S1053249823021782 (2023) doi:10.1016/j.healun.2023.12.009.
155. Omura, J. *et al.* Identification of Long Noncoding RNA H19 as a New Biomarker and Therapeutic Target in Right Ventricular Failure in Pulmonary Arterial Hypertension. *Circulation* **142**, 1464–1484 (2020).
156. Amsallem, M. *et al.* Targeted proteomics of right heart adaptation to pulmonary arterial hypertension. *Eur. Respir. J.* **57**, 2002428 (2021).
157. Pullamsetti, S. S., Tello, K. & Seeger, W. Utilising biomarkers to predict right heart maladaptive phenotype: a step toward precision medicine. *Eur. Respir. J.* **57**, 2004506 (2021).
158. Provencher, S. *et al.* Standards and Methodological Rigor in Pulmonary Arterial Hypertension Preclinical and Translational Research. *Circ. Res.* **122**, 1021–1032 (2018).
159. Khassafi, F. *et al.* Transcriptional profiling unveils molecular subgroups of adaptive and maladaptive right ventricular remodeling in pulmonary hypertension. *Nat. Cardiovasc. Res.* **2**, 917–936 (2023).
160. Tello, K. *et al.* Reserve of Right Ventricular-Arterial Coupling in the Setting of Chronic Overload. *Circ. Heart Fail.* **12**, e005512 (2019).

161. Tello, K. *et al.* Relevance of the TAPSE/PASP ratio in pulmonary arterial hypertension. *Int. J. Cardiol.* **266**, 229–235 (2018).
162. Levey, A. S. *et al.* Using Standardized Serum Creatinine Values in the Modification of Diet in Renal Disease Study Equation for Estimating Glomerular Filtration Rate. *Ann. Intern. Med.* **145**, 247–254 (2006).
163. Kariotis, S. *et al.* Biological heterogeneity in idiopathic pulmonary arterial hypertension identified through unsupervised transcriptomic profiling of whole blood. *Nat. Commun.* **12**, 7104 (2021).
164. Tofovic, S. P. Estrogens and Development of Pulmonary Hypertension: Interaction of Estradiol Metabolism and Pulmonary Vascular Disease: *J. Cardiovasc. Pharmacol.* **56**, 696–708 (2010).
165. Potus, F. *et al.* Downregulation of MicroRNA-126 Contributes to the Failing Right Ventricle in Pulmonary Arterial Hypertension. *Circulation* **132**, 932–943 (2015).
166. Fulton, R. M., Hutchinson, E. C. & Jones, A. M. VENTRICULAR WEIGHT IN CARDIAC HYPERTROPHY. *Heart* **14**, 413–420 (1952).
167. Augustine, D. X. *et al.* Echocardiographic assessment of pulmonary hypertension: a guideline protocol from the British Society of Echocardiography. *Echo Res. Pract.* **5**, G11–G24 (2018).
168. Shimauchi, T. *et al.* TRPC3-Nox2 complex mediates doxorubicin-induced myocardial atrophy. *JCI Insight* **2**, e93358 (2017).
169. Bolger, A. M., Lohse, M. & Usadel, B. Trimmomatic: a flexible trimmer for Illumina sequence data. *Bioinformatics* **30**, 2114–2120 (2014).
170. Dobin, A. *et al.* STAR: ultrafast universal RNA-seq aligner. *Bioinformatics* **29**, 15–21 (2013).
171. Liao, Y., Smyth, G. K. & Shi, W. featureCounts: an efficient general purpose program for assigning sequence reads to genomic features. *Bioinformatics* **30**, 923–930 (2014).
172. Love, M. I., Huber, W. & Anders, S. Moderated estimation of fold change and dispersion for RNA-seq data with DESeq2. *Genome Biol.* **15**, 550 (2014).
173. Leek, J. T., Johnson, W. E., Parker, H. S., Jaffe, A. E. & Storey, J. D. The sva package for removing batch effects and other unwanted variation in high-throughput experiments. *Bioinformatics* **28**, 882–883 (2012).
174. Bu, D. *et al.* KOBAS-i: intelligent prioritization and exploratory visualization of biological functions for gene enrichment analysis. *Nucleic Acids Res.* **49**, W317–W325 (2021).
175. Tay, J. K., Narasimhan, B. & Hastie, T. Elastic Net Regularization Paths for All Generalized Linear Models. *J. Stat. Softw.* **106**, (2023).
176. Assarsson, E. *et al.* Homogenous 96-Plex PEA Immunoassay Exhibiting High Sensitivity, Specificity, and Excellent Scalability. *PLoS ONE* **9**, e95192 (2014).
177. Wright, M. N. & Ziegler, A. ranger: A Fast Implementation of Random Forests for High Dimensional Data in C++ and R. (2015) doi:10.48550/ARXIV.1508.04409.
178. Mason, S. J. & Graham, N. E. Areas beneath the relative operating characteristics (ROC) and relative operating levels (ROL) curves: Statistical significance and interpretation. *Q. J. R. Meteorol. Soc.* **128**, 2145–2166 (2002).
179. Pullamsetti, S. S. *et al.* Lung cancer–associated pulmonary hypertension: Role of microenvironmental inflammation based on tumor cell–immune cell cross-talk. *Sci. Transl. Med.* **9**, eaai9048 (2017).
180. Hołda, M. K. *et al.* Myocardial proteomic profile in pulmonary arterial hypertension. *Sci. Rep.* **10**, 14351 (2020).
181. Rhodes, C. J. *et al.* Plasma proteome analysis in patients with pulmonary arterial hypertension: an observational cohort study. *Lancet Respir. Med.* **5**, 717–726 (2017).
182. Arvidsson, M., Ahmed, A., Säleby, J., Hesselstrand, R. & Rådegran, G. Plasma matrix metalloproteinase 2 is associated with severity and mortality in pulmonary arterial hypertension. *Pulm. Circ.* **12**, e12041 (2022).
183. Sanz, J. *et al.* Right ventriculo-arterial coupling in pulmonary hypertension: a magnetic resonance study. *Heart* **98**, 238–243 (2012).
184. Richter, M. J. & Tello, K. Against the Odds: Risk Stratification with Cardiac Magnetic Resonance Imaging in Pulmonary Arterial Hypertension. *Am. J. Respir. Crit. Care Med.* **201**, 403–405 (2020).
185. Klingler, A. *et al.* Species-, organ- and cell-type-dependent expression of SPARCL1 in human and mouse tissues. *PloS One* **15**, e0233422 (2020).
186. Jiang, B. *et al.* Marked Strain-Specific Differences in the SU5416 Rat Model of Severe Pulmonary Arterial Hypertension. *Am. J. Respir. Cell Mol. Biol.* **54**, 461–468 (2016).
187. Gomez-Arroyo, J. G. *et al.* The monocrotaline model of pulmonary hypertension in perspective. *Am. J. Physiol.-Lung Cell. Mol. Physiol.* **302**, L363–L369 (2012).
188. Campian, M. E. *et al.* Early inflammatory response during the development of right ventricular heart failure in a rat model. *Eur. J. Heart Fail.* **12**, 653–658 (2010).
189. Akazawa, Y. *et al.* Pulmonary artery banding is a relevant model to study the right ventricular remodeling and dysfunction that occurs in pulmonary arterial hypertension. *J. Appl. Physiol.* **129**, 238–246 (2020).

190. Boucherat, O., Agrawal, V., Lawrie, A. & Bonnet, S. The Latest in Animal Models of Pulmonary Hypertension and Right Ventricular Failure. *Circ. Res.* **130**, 1466–1486 (2022).
191. Borgdorff, M. A. J. *et al.* Distinct loading conditions reveal various patterns of right ventricular adaptation. *Am. J. Physiol.-Heart Circ. Physiol.* **305**, H354–H364 (2013).
192. Taraseviciene-Stewart, L. *et al.* Inhibition of the VEGF receptor 2 combined with chronic hypoxia causes cell death-dependent pulmonary endothelial cell proliferation and severe pulmonary hypertension. *FASEB J.* **15**, 427–438 (2001).
193. Suen, C. M., Chaudhary, K. R., Deng, Y., Jiang, B. & Stewart, D. J. Fischer rats exhibit maladaptive structural and molecular right ventricular remodelling in severe pulmonary hypertension: a genetically prone model for right heart failure. *Cardiovasc. Res.* **115**, 788–799 (2019).
194. Potus, F., Hindmarch, C., Dunham-Snary, K., Stafford, J. & Archer, S. Transcriptomic Signature of Right Ventricular Failure in Experimental Pulmonary Arterial Hypertension: Deep Sequencing Demonstrates Mitochondrial, Fibrotic, Inflammatory and Angiogenic Abnormalities. *Int. J. Mol. Sci.* **19**, 2730 (2018).
195. Wu, X. *et al.* Experimental animal models of pulmonary hypertension: Development and challenges. *Anim. Models Exp. Med.* **5**, 207–216 (2022).
196. Cao, Y. *et al.* RNA-sequencing analysis of gene expression in a rat model of acute right heart failure. *Pulm. Circ.* **10**, 1–13 (2020).
197. Prisco, S. Z., Eklund, M., Raveendran, R., Thenappan, T. & Prins, K. W. With No Lysine Kinase 1 Promotes Metabolic Derangements and RV Dysfunction in Pulmonary Arterial Hypertension. *JACC Basic Transl. Sci.* **6**, 834–850 (2021).
198. Silva, J. M. A. *et al.* Hypertrophy of the right ventricle by pulmonary artery banding in rats: a study of structural, functional, and transcriptomics alterations in the right and left ventricles. *Front. Physiol.* **14**, 1129333 (2023).
199. Fliegner, D. *et al.* Female sex and estrogen receptor-β attenuate cardiac remodeling and apoptosis in pressure overload. *Am. J. Physiol.-Regul. Integr. Comp. Physiol.* **298**, R1597–R1606 (2010).
200. Regitz-Zagrosek, V. & Kararigas, G. Mechanistic Pathways of Sex Differences in Cardiovascular Disease. *Physiol. Rev.* **97**, 1–37 (2017).
201. Kessler, E. L., Rivaud, M. R., Vos, M. A. & Van Veen, T. A. B. Sex-specific influence on cardiac structural remodeling and therapy in cardiovascular disease. *Biol. Sex Differ.* **10**, 7 (2019).
202. Regitz-Zagrosek, V. & Gebhard, C. Gender medicine: effects of sex and gender on cardiovascular disease manifestation and outcomes. *Nat. Rev. Cardiol.* **20**, 236–247 (2023).
203. Bal, E., Ilgin, S., Atli, O., Ergun, B. & Sirmagul, B. The effects of gender difference on monocrotaline-induced pulmonary hypertension in rats. *Hum. Exp. Toxicol.* **32**, 766–774 (2013).
204. Carascossa, S., Dudek, P., Cenni, B., Briand, P.-A. & Picard, D. CARM1 mediates the ligand-independent and tamoxifen-resistant activation of the estrogen receptor α by cAMP. *Genes Dev.* **24**, 708–719 (2010).
205. Predescu, D. N., Mokhlesi, B. & Predescu, S. A. The Impact of Sex Chromosomes in the Sexual Dimorphism of Pulmonary Arterial Hypertension. *Am. J. Pathol.* **192**, 582–594 (2022).
206. Kostyunina, D. S. & McLoughlin, P. Sex Dimorphism in Pulmonary Hypertension: The Role of the Sex Chromosomes. *Antioxidants* **10**, 779 (2021).
207. Umar, S. *et al.* The Y Chromosome Plays a Protective Role in Experimental Hypoxic Pulmonary Hypertension. *Am. J. Respir. Crit. Care Med.* **197**, 952–955 (2018).
208. Shiojima, I. Disruption of coordinated cardiac hypertrophy and angiogenesis contributes to the transition to heart failure. *J. Clin. Invest.* **115**, 2108–2118 (2005).
209. Sutendra, G. *et al.* A metabolic remodeling in right ventricular hypertrophy is associated with decreased angiogenesis and a transition from a compensated to a decompensated state in pulmonary hypertension. *J. Mol. Med.* **91**, 1315–1327 (2013).
210. Ohira, H. *et al.* Shifts in myocardial fatty acid and glucose metabolism in pulmonary arterial hypertension: a potential mechanism for a maladaptive right ventricular response. *Eur. Heart J. – Cardiovasc. Imaging* **17**, 1424–1431 (2016).
211. Legchenko, E. *et al.* PPARγ agonist pioglitazone reverses pulmonary hypertension and prevents right heart failure via fatty acid oxidation. *Sci. Transl. Med.* **10**, eaao0303 (2018).
212. Tang, C. *et al.* Characteristics of inflammation process in monocrotaline-induced pulmonary arterial hypertension in rats. *Biomed. Pharmacother.* **133**, 111081 (2021).
213. Dewachter, L. & Dewachter, C. Inflammation in Right Ventricular Failure: Does It Matter? *Front. Physiol.* **9**, 1056 (2018).
214. Wrigley, B. J., Lip, G. Y. H. & Shantsila, E. The role of monocytes and inflammation in the pathophysiology of heart failure. *Eur. J. Heart Fail.* **13**, 1161–1171 (2011).
215. Von Haehling, S. *et al.* Inflammation in right ventricular dysfunction due to thromboembolic pulmonary hypertension. *Int. J. Cardiol.* **144**, 206–211 (2010).

216. Watts, J. A., Zagorski, J., Gellar, M. A., Stevinson, B. G. & Kline, J. A. Cardiac inflammation contributes to right ventricular dysfunction following experimental pulmonary embolism in rats. *J. Mol. Cell. Cardiol.* **41**, 296–307 (2006).
217. Piao, L. *et al.* Cardiac glutaminolysis: a maladaptive cancer metabolism pathway in the right ventricle in pulmonary hypertension. *J. Mol. Med.* **91**, 1185–1197 (2013).
218. Reddy, S. & Bernstein, D. Molecular Mechanisms of Right Ventricular Failure. *Circulation* **132**, 1734–1742 (2015).
219. Wang, L. *et al.* Quantitative assessment of right ventricular glucose metabolism in idiopathic pulmonary arterial hypertension patients: a longitudinal study. *Eur. Heart J. – Cardiovasc. Imaging* **17**, 1161–1168 (2016).
220. King, K. R. *et al.* IRF3 and type I interferons fuel a fatal response to myocardial infarction. *Nat. Med.* **23**, 1481–1487 (2017).
221. Paulin, R. & Michelakis, E. D. The Metabolic Theory of Pulmonary Arterial Hypertension. *Circ. Res.* **115**, 148–164 (2014).
222. Kolb, T. M. *et al.* Right Ventricular Angiogenesis is an Early Adaptive Response to Chronic Hypoxia-Induced Pulmonary Hypertension. *Microcirculation* **22**, 724–736 (2015).
223. Dunn, L. L. *et al.* Hmox1 (Heme Oxygenase-1) Protects Against Ischemia-Mediated Injury via Stabilization of HIF-1α (Hypoxia-Inducible Factor-1α). *Arterioscler. Thromb. Vasc. Biol.* (2020) doi:10.1161/ATVBAHA.120.315393.
224. Ruwhof, C., Van Wamel, A. E. T., Egas, J. M. & Van Der Laarse, A. Cyclic stretch induces the release of growth promoting factors from cultured neonatal cardiomyocytes and cardiac fibroblasts. *Mol. Cell. Biochem.* **208**, 89–98 (2000).
225. Rienks, M., Papageorgiou, A.-P., Frangogiannis, N. G. & Heymans, S. Myocardial Extracellular Matrix: An Ever-Changing and Diverse Entity. *Circ. Res.* **114**, 872–888 (2014).
226. Berk, B. C., Fujiwara, K. & Lehoux, S. ECM remodeling in hypertensive heart disease. *J. Clin. Invest.* **117**, 568–575 (2007).
227. Frangogiannis, N. G. Fibroblasts and the extracellular matrix in right ventricular disease. *Cardiovasc. Res.* **113**, 1453–1464 (2017).
228. Iyer, R. P., Jung, M. & Lindsey, M. L. MMP-9 signaling in the left ventricle following myocardial infarction. *Am. J. Physiol.-Heart Circ. Physiol.* **311**, H190–H198 (2016).
229. Baron, M. A. *et al.* Matrix Metalloproteinase 2 and 9 Enzymatic Activities are Selectively Increased in the Myocardium of Chronic Chagas Disease Cardiomyopathy Patients: Role of TIMPs. *Front. Cell. Infect. Microbiol.* **12**, 836242 (2022).
230. Martos, R. *et al.* Diastolic Heart Failure: Evidence of Increased Myocardial Collagen Turnover Linked to Diastolic Dysfunction. *Circulation* **115**, 888–895 (2007).
231. Chelladurai, P., Seeger, W. & Pullamsetti, S. S. Matrix metalloproteinases and their inhibitors in pulmonary hypertension. *Eur. Respir. J.* **40**, 766–782 (2012).
232. Man, J., Barnett, P. & Christoffels, V. M. Structure and function of the Nppa–Nppb cluster locus during heart development and disease. *Cell. Mol. Life Sci.* **75**, 1435–1444 (2018).
233. Imanaka-Yoshida, K., Tawara, I. & Yoshida, T. Tenascin-C in cardiac disease: a sophisticated controller of inflammation, repair, and fibrosis. *Am. J. Physiol.-Cell Physiol.* **319**, C781–C796 (2020).
234. Valiente-Alandi, I. *et al.* Inhibiting Fibronectin Attenuates Fibrosis and Improves Cardiac Function in a Model of Heart Failure. *Circulation* **138**, 1236–1252 (2018).
235. Liu, X. *et al.* Lineage-specific regulatory changes in hypertrophic cardiomyopathy unraveled by single-nucleus RNA-seq and spatial transcriptomics. *Cell Discov.* **9**, 6 (2023).
236. Chiao, Y. A. *et al.* Matrix metalloproteinase-9 deletion attenuates myocardial fibrosis and diastolic dysfunction in ageing mice. *Cardiovasc. Res.* **96**, 444–455 (2012).
237. Yan, Y. *et al.* Implication of proliferation gene biomarkers in pulmonary hypertension. *Anim. Models Exp. Med.* **4**, 369–380 (2021).
238. Vonk Noordegraaf, A. *et al.* Pathophysiology of the right ventricle and of the pulmonary circulation in pulmonary hypertension: an update. *Eur. Respir. J.* **53**, 1801900 (2019).
239. Ahmed, S. H. *et al.* Matrix Metalloproteinases/Tissue Inhibitors of Metalloproteinases: Relationship Between Changes in Proteolytic Determinants of Matrix Composition and Structural, Functional, and Clinical Manifestations of Hypertensive Heart Disease. *Circulation* **113**, 2089–2096 (2006).
240. Jugdutt, B. Remodeling of the Myocardium and Potential Targets in the Collagen Degradation and Synthesis Pathways. *Curr. Drug Target -Cardiovasc. Hematol. Disord.* **3**, 1–30 (2003).
241. Kaiser, R., Frantz, C., Bals, R. & Wilkens, H. The role of circulating thrombospondin-1 in patients with precapillary pulmonary hypertension. *Respir. Res.* **17**, 96 (2016).
242. Damico, R. *et al.* Serum Endostatin Is a Genetically Determined Predictor of Survival in Pulmonary Arterial Hypertension. *Am. J. Respir. Crit. Care Med.* **191**, 208–218 (2015).

243. Zhou, S., Chen, S., Pei, Y. A. & Pei, M. Nidogen: A matrix protein with potential roles in musculoskeletal tissue regeneration. *Genes Dis.* **9**, 598–609 (2022).
244. Kim, E. H. *et al.* Differential protein expression and basal lamina remodeling in human heart failure. *PROTEOMICS - Clin. Appl.* **10**, 585–596 (2016).
245. Zbinden, A. *et al.* Nidogen-1 Mitigates Ischemia and Promotes Tissue Survival and Regeneration. *Adv. Sci.* **8**, 2002500 (2021).
246. Lu, L. *et al.* C1q/TNF-related protein-1: an adipokine marking and promoting atherosclerosis. *Eur. Heart J.* **37**, 1762–1771 (2016).
247. Muendlein, A. *et al.* The novel adipokine CTRP1 is significantly associated with the incidence of major adverse cardiovascular events. *Atherosclerosis* **286**, 1–6 (2019).
248. Shen, L., Wang, S., Ling, Y. & Liang, W. Association of C1q/TNF-related protein-1 (CTRP1) serum levels with coronary artery disease. *J. Int. Med. Res.* **47**, 2571–2579 (2019).
249. Su, Z., Tian, S. & Liang, W. Circulating CTRP1 Levels Are Increased and Associated with the STOD in Essential Hypertension in Chinese Patients. *Cardiovasc. Ther.* **2019**, 1–7 (2019).
250. Gu, Y. *et al.* CTRP1 Aggravates Cardiac Dysfunction Post Myocardial Infarction by Modulating TLR4 in Macrophages. *Front. Immunol.* **12**, 635267 (2021).
251. Yang, Y. *et al.* Association Between C1q/TNF-Related Protein-1 Levels in Human Plasma and Epicardial Adipose Tissues and Congestive Heart Failure. *Cell. Physiol. Biochem.* **42**, 2130–2143 (2017).
252. Schellings, M. W. M. *et al.* Absence of SPARC results in increased cardiac rupture and dysfunction after acute myocardial infarction. *J. Exp. Med.* **206**, 113–123 (2009).
253. Sullivan, M. M. *et al.* Matricellular Hevin Regulates Decorin Production and Collagen Assembly. *J. Biol. Chem.* **281**, 27621–27632 (2006).
254. Di Salvo, T. G. *et al.* Right Ventricular Myocardial Biomarkers in Human Heart Failure. *J. Card. Fail.* **21**, 398–411 (2015).
255. Keranov, S. *et al.* SPARCL1 as a biomarker of maladaptive right ventricular remodelling in pulmonary hypertension. *Biomarkers* **25**, 290–295 (2020).
256. Kuwashiro, T. *et al.* Oxidized Albumin and Cartilage Acidic Protein-1 as Blood Biomarkers to Predict Ischemic Stroke Outcomes. *Front. Neurol.* **12**, 686555 (2021).
257. Ji, Y. *et al.* Inhibition of Cartilage Acidic Protein 1 Reduces Ultraviolet B Irradiation Induced-Apoptosis through P38 Mitogen-Activated Protein Kinase and Jun Amino-Terminal Kinase Pathways. *Cell. Physiol. Biochem.* **39**, 2275–2286 (2016).
258. Wang, W. *et al.* Underlying Genes Involved in Atherosclerotic Macrophages: Insights from Microarray Data Mining. *Med. Sci. Monit.* **25**, 9949–9962 (2019).
259. Steck, E. *et al.* Chondrocyte secreted CRTAC1: A glycosylated extracellular matrix molecule of human articular cartilage. *Matrix Biol.* **26**, 30–41 (2007).
260. Mayr, C. H. *et al.* Integrative analysis of cell state changes in lung fibrosis with peripheral protein biomarkers. *EMBO Mol. Med.* **13**, e12871 (2021).
261. Li, M. *et al.* Identification of Post-myocardial Infarction Blood Expression Signatures Using Multiple Feature Selection Strategies. *Front. Physiol.* **11**, 483 (2020).
262. Kuhn, M. Building Predictive Models in *R* Using the **caret** Package. *J. Stat. Softw.* **28**, (2008).
263. Couronné, R., Probst, P. & Boulesteix, A.-L. Random forest versus logistic regression: a large-scale benchmark experiment. *BMC Bioinformatics* **19**, 270 (2018).
264. Rajput, D., Wang, W.-J. & Chen, C.-C. Evaluation of a decided sample size in machine learning applications. *BMC Bioinformatics* **24**, 48 (2023).
265. Michelhaugh, S. A. & Januzzi, J. L. Finding a Needle in a Haystack. *JACC Basic Transl. Sci.* **5**, 1043–1053 (2020).
266. Raffield, L. M. *et al.* Comparison of Proteomic Assessment Methods in Multiple Cohort Studies. *PROTEOMICS* **20**, 1900278 (2020).
267. Ren, Z. *et al.* Single-Cell Reconstruction of Progression Trajectory Reveals Intervention Principles in Pathological Cardiac Hypertrophy. *Circulation* **141**, 1704–1719 (2020).

10. DECLARATION

I declare that I have completed this dissertation single-handedly without the unauthorized help of a second party and only with the assistance acknowledged therein. I have appropriately acknowledged and referenced all text passages that are derived literally from or are based on the content of published or unpublished work of others, and all information that relates to verbal communications. I have abided by the principles of good scientific conduct laid down in the charter of the Justus Liebig University of Giessen in carrying out the investigations described in the dissertation.

_____ _____

Place, Date Signature

11. ACKNOWLEDGEMENTS

First and foremost, I am deeply grateful to my supervisor, **Prof. Dr. Soni Savai Pullamsetti,** for the amazing chance to do my doctoral research in her lab. Her support and helpful feedbacks have been incredibly inspiring, enriching every part of my journey. Through every discussion, I learned so much from her, and her advice was the best support I could have asked for during the up and downs of my PhD. Her guidance was not just advice but a life-changing experience that deeply influenced my academic and personal development, and I am forever thankful.

I extend my thanks to **Prof. Dr. Werner Seeger** for establishing a dynamic platform for engaging and intellectually stimulating scientific discussions has been invaluable.

I would like to express my especial thanks to my collaborators from University of Laval, Canada, **Prof. Dr. Sebastien Bonnet,** and his supportive team, in particular, **Olivier Boucherat,** and **Sandra Breuils-Bonnet,** for generously providing human RV samples and conducting numerous in-vivo experiments on rats, and sharing their valuable knowledge and expertise in this field.

I am profoundly grateful to **Dr. Mario Looso**, **Dr. Carsten Kuenne**, and **Dr. Stefan Guenther** for their exceptional and incredible support. Their expertise in RNA sequencing experiments and processing the samples have been instrumental in my research. Beyond the technical aspects, their willingness to assist in analyzing numerous datasets has been invaluable. Their thoughtful guidance within the bioinformatics team consistently illuminated my path throughout my PhD journey, offering insights and encouragement that deeply enriched my experience.

I would like to express my gratitude to **Prof. Dr Khodr Tello**, and **Prof. Dr. Natascha Sommer** from Universitätsklinikum Giessen, for kindly offering to share the PAH plasma cohorts for our explorations, and their valued insights on the RV functional assessment in PAH.

I would also thank **Prof. Allan Lawrie** from Imperial College London, for sharing the UK PAH cohort, and providing their valuable input to this research.

I feel incredibly fortunate to have been surrounded by such wonderful lab members. My sincere thanks go out to all my colleagues for always being there for me. My special gratitude is reserved for **Dr. Prakash Chelladurai** and **Dr. Chanil Valasarajan**, whose assistance and insights proved to be indispensable through my research. Their contributions made every facet of my project significantly better, and easier.

I am eternally thankful to **my parents** for their boundless support and belief in me. Without their encouragement and faith, none of my achievements would have been possible.

In closing, I must express my heartfelt thanks to **Aryan**, whose unconditional love, unlimited patience, constant support and assistance in every imaginable way have been foundation of my confidence throughout these years, making every challenge beatable and every triumph sweeter. The thought of navigating this journey without his companionship is impossible to me.